

NORTHWESTERN UNIVERSITY

Surface Chemistry of Organic Molecules in Atmospheric and Indoor Environments Investigated  
by Sum Frequency Generation Spectroscopy

A DISSERTATION

SUBMITTED TO THE GRADUATE SCHOOL  
IN PARTIAL FULFILLMENT OF THE REQUIREMENTS

for the degree

DOCTOR OF PHILOSOPHY

Field of Chemistry

By

Yangdongling Liu

EVANSTON, ILLINOIS

September 2021

© Copyright by Yangdongling Liu 2021

All Rights Reserved

## Abstract

Surface Chemistry of Organic Molecules in Atmospheric and Indoor Environments

Investigated by Sum Frequency Generation Spectroscopy

Yangdongling Liu

This work examines important heterogeneous processes of organic molecules on surfaces, in the contexts of atmospheric and indoor environments.

In large forest ecosystems, biogenic secondary organic aerosols (SOAs) constitute a dominant fraction of organic particulate matter in the atmosphere. The formation of SOAs starts from the emission of volatile organic compounds (VOCs), among which monoterpenes are a common class, and the adsorption of VOCs and their oxidation products to aerosol seeds or particles. The first part of the thesis presents the experimental measurements of the adsorption thermodynamics and reversibility of a suite of monoterpenes, compared to non-terpene hydrocarbons, for insights into the formation and evolution of biogenic SOAs.

The high surface-to-volume ratio of indoor environments makes surface chemistry particularly important to the study of indoor air quality. However, surface-mediated transformations in indoor environments are not adequately understood. The second part of the thesis provides an overview of the research opportunities in indoor surface chemistry and then dives into a specific study on squalene, a major ozone-active constituent in human skin oil. We present a combined spectroscopic and atomistic modeling approach to elucidate the conformational and orientational preferences of squalene at the air/squalene interface and their implications for reactions with ozone. Beyond idealized model surfaces, we initiated a field campaign, Stay-at-HomeChem, that aims at collecting authentic home-derived samples under the

stay-at-home orders during the COVID-19 pandemic to study the impact of increased human occupancy on indoor air chemistry.

In the last section, we demonstrate the efforts on developing a sum frequency scattering setup that can potentially probe suspended gas-phase aerosols for the first time. This capability will expand the research objects from macroscopically flat surfaces to submicron aerosol surfaces, which would largely benefit both the atmospheric chemistry and indoor air chemistry communities.

---

Prof. Franz M. Geiger

Research Advisor

## Acknowledgements

I would like to first give my warmest thanks to Prof. Franz Geiger for being an incredible advisor throughout my graduate school career. Franz, your passion in science has always been infectious. I can't count how many times I walked into your office with questions and walked out with a clear plan and a recharged mind. I wouldn't have made this far without your support. I would like to thank my committee members, Prof. Peter Stair, Prof. Richard Schaller, and Prof. Elad Harel for their valuable feedbacks on my research. Prof. Peter Stair and Prof. Richard Schaller were very understanding and supportive when I was going through some hard times and I sincerely appreciate it. A special thank you to Prof. Regan Thomson for being another advisor of mine on atmospheric chemistry. I would also like to express my deepest gratitude to my undergraduate advisor, Prof. Vivian Wing-wah Yam, at the University of Hong Kong, and my summer research advisor, Dr. Stefan Minasian, at Lawrence Berkeley National Laboratory, for introducing me to chemistry research.

I feel honored to have worked with amazing collaborators and learned a lot from them, with special thanks to Dr. Aashish Tuladhar, Dr. Yiming Qin, Dr. Michael von Domaros, and Prof. Douglas Tobias. I was fortunate to have the opportunity to start working on indoor surface chemistry and meet the vibrant and collaborative community of the Surface Consortium for Chemistry of Indoor Environments. I am extremely grateful to Prof. Vicki Grassian and her group, especially Victor Or and Michael Alves, at UC San Diego, for providing great support for us entering the indoor chemistry field and discussing research opportunities and experiences with us. At Northwestern University, Prof. Neil Schweitzer at REACT Core Facility and Alex Villatoro, who used to work at Lab Services, gave me important practical advice on building the gas flow

system. I would also like to express my appreciation to Dr. Derek Nelson for being a supportive and inspiring mentor throughout my teaching experience.

To former and current members of Geiger group, I am so grateful that you are part of my graduate school life. To Laura, Mary Alice, Hilary, Alicia, Merve, Paul, Mavis, Ariana, and Johnny, thank you for teaching me everything and helping me grow. Special thanks to Hilary – you helped me get started on my first project. To Ariana – I am so thankful that I got to work closely with you and have a lot of shared memories with you. I vividly remember the many fruitful collaboration and conference trips we took together, to Purdue, to Harvard, to San Diego, and to PNNL. To Paul – you are my role model. I can't thank you enough for how much you have taught me on both specific techniques and scientific thinking. To Naomi – thank you for always being by my side. Your company and support have helped me get through many difficult times. You know I will always be there for you when you need me. To Hanbyul, Jana, Aleia, Emilie, Emily, Rico, and Cat – thank you for adding energy to our group and keeping the research going!

Finally, thank you to my friends and family who supported me, inspired me, and energized me. I am lucky to have met an incredibly smart, kind, and supportive cohort at Northwestern, with special thanks to Dr. Suyog Padgaonkar, Dr. Matt Nisbet, Dr. Xinyi Jiang, and Ariel Leonard. To my old friends, Jinxian, Chenyue, Boya, and Dianjing, you make me a better person and it warms my heart every time I think about you. To Liz, Ed, Anne, John, and Thomas, thank you for everything you have done for me. To Mom and Dad, you are the strongest people and your love has supported me through every stage of my life. I can't express how much I appreciate you and love you. Last but not least, Nate, you are everything to me. Your curiosity and scientific mind have never failed to inspire me. Your adventurous spirit has led me to see a bigger world. Thank you for being with me through thick and thin and I am looking forward to our future journeys!

*To Mom and Dad.*

*To my husband, Nate.*

**List of Abbreviations**

AFM	Atomic force microscopy
AMS	Aerosol mass spectrometry
APPI	Atmospheric pressure photoionization
ARM	Atmospheric Radiation Measurement
ATR	Attenuated total reflection
CCD	Charge-coupled device
CCN	Cloud condensation nuclei
CHARMM	Chemistry at Harvard Macromolecular Mechanics
CI	Chemical ionization
COVID-19	Coronavirus disease 2019
CPC	Condensation particle counter
DART	Direct analysis in real time
DFT	Density functional theory
ESI	Electrospray ionization
FT	Fourier Transform
GC	Gas chromatography
HPLC	High performance liquid chromatography
ID	Inner diameter
IEPOX	Isoprene epoxy diol
IR	Infrared
IUPAC	International Union of Pure and Applied Chemistry



LC	Liquid chromatography
MD	Molecular dynamics
MFC	Mass flow controller
MOUDI	Micro-orifice uniform-deposit impactors
MS	Mass spectrometry
OD	Outer diameter
PMIRAS	Polarization modulation infrared reflectance absorption spectroscopy
ppb	Parts per billion
ppm	Parts per million
PTIR	Photothermal infrared
PTR	Proton transfer reaction
PVC	Polyvinyl chloride
RH	Relative humidity
QCM	Quartz crystal microbalance
SFG	Sum frequency generation
SFS	Sum frequency scattering
SHS	Second harmonic scattering
SLPM	Standard liter per minute
SOA	Secondary organic aerosol
SVOC	Semi-volatile organic compound
TOPAS	Tunable optical parametric amplifier setup
UHV	Ultra-high vacuum

UV	Ultraviolet
Vis	Visible
VOC	Volatile organic compound
XRF	X-ray fluorescence

## Table of Contents

<b>Abstract</b> .....	3
<b>Acknowledgements</b> .....	5
<b>List of Abbreviations</b> .....	8
<b>Table of Contents</b> .....	11
<b>List of Figures</b> .....	15
<b>List of Tables</b> .....	19
 <b>Chapter 1 Introduction to Surface Chemistry in Atmospheric and Indoor</b>	
<b>Environments</b> .....	20
1.1 Heterogeneous Processes on the Surfaces of Atmospheric Aerosols.....	21
1.2 Molecular-Level Indoor Surface Chemistry and Physics. ....	23
1.3 Challenges and State-of-the-Art Techniques to Overcome Them .....	25
1.3.1 Challenges .....	25
1.3.2 State-of-the-Art Techniques. ....	27
1.4 Vibrational Sum Frequency Generation (SFG) Spectroscopy .....	29
1.5 Thesis Scope and Organization .....	30
 <b>Chapter 2 Adsorption Thermodynamics, Reversibility, and Reactivity of</b>	
<b>Monoterpenes at Surfaces</b> .....	32
2.1 Introduction.....	33
2.2 Methods .....	34
2.2.1 Materials .....	34
2.2.2 SFG Spectroscopy .....	34

	12
2.2.3 Flow Setup .....	35
2.3 Results and Discussion .....	37
2.3.1 SFG Spectra of Acyclic and Cyclic Alkanes at Vapor/Fused Silica Interface Are in Close Agreement with Literature .....	37
2.3.2 The Adsorption of Terpenes Shows Partial Reversibility While Non-Terpene Hydrocarbons Do Not. ....	39
2.3.3 Gibbs Free Adsorption Energies Are Loosely Correlated with $P_{vap}$ ..	43
2.3.4 Molecular Orientation Distributions Show Negligible Changes with Terpene/VOC Vapor Pressure in C-H Stretching Region Except for Cyclohexane.....	46
2.4 Conclusion .....	49
2.5 Expanded Capabilities and Ongoing Research. ....	51
2.5.1 Higher Sensitivity of the New SFG Setup .....	51
2.5.2 The Development of an Integrated and Versatile Flow Setup that Mimics the Atmospheric Environment.....	52
2.5.3 Attempts of In-Situ Monitoring of Ozonolysis of Surface-Adsorbed Terpenes. ....	54
<b>Chapter 3 Molecular-Level Surface Chemistry and Physics of Indoor Air .....</b>	<b>59</b>
3.1 Perspectives on Research Opportunities in Indoor Surface Chemistry and Physics.....	60
3.1.1 Research questions .....	61
3.1.2 Experimental considerations. ....	68

3.2 Molecular Orientation at the Squalene/Air Interface .....	70
3.2.1 Introduction .....	70
3.2.2 Methods .....	73
A. Sample Preparation and SFG Measurements .....	73
B. Spectral Fitting Procedure .....	74
C. Molecular Dynamics (MD) Simulations .....	75
D. Electronic Structure Calculations. ....	76
3.2.3 Results and Discussion. ....	76
A. SFG spectra of the surface of a squalene film.....	77
B. Spectral Fitting Attempts.....	80
C. Squalene Tends to Orient Along Surface Normal with Terminal Double Bonds Nearest Surface.....	82
D. Four in Five Squalene Molecules Have at Most One Gauche Defect .....	83
E. Methyl Groups Prefer Alignment Along Surface Normal, Other Groups Much Less So.....	84
F. Vibrational Frequency Analysis. ....	86
3.2.4 Implications for Ozonolysis Rates .....	89
3.2.5 Conclusions .....	90
3.3 Preliminary Investigations on Ozonolysis of Squalene and Skin Oil.....	92
3.4 Home-Derived Indoor Molecular, Nano-, and Microlayers – StayAtHomeChem Campaign .....	95

	14
3.4.1 Techniques to be Used for Sample Analysis .....	96
3.4.2 Information about Participants' Home Environments.....	97
3.4.3 Timeline of Experiments for Each Room .....	100
3.4.4 Sample Collection and Storage .....	103
3.4.5 Field Diary/Data Logging .....	103
 <b>Chapter 4 Vibrational Sum Frequency Scattering (SFS) Setup for Suspended</b>	
<b>Aerosols</b> .....	105
4.1 Introduction.....	106
4.2 Experimental Considerations .....	107
4.3 Experimental Setup.....	108
4.4 Preliminary Results and Future Plans.....	111
<b>References</b> .....	113
 <b>Appendix SFG Spectroscopy of Field Aerosol Samples from the GoAmazon2014/5</b>	
Campaign .....	141
<b>Curriculum Vitae</b> .....	152

## List of Figures

- Figure 1.1.** An illustration of role of aerosols in the climate system and in the atmosphere. .... 22
- Figure 1.2.** Indoor molecular, nano-, and microlayers form initially through the adsorption of indoor semivolatile and volatile organic compounds ( $\alpha$ -pinene as an example) to engineered indoor surfaces. The new physical and chemical properties of these surfaces need to be understood from a molecular perspective with techniques that are applicable under ambient conditions relevant to indoor environments. .... 24
- Figure 1.3.** Multi-pronged approach for probing the surface physics and chemistry of indoor molecular, nano-, and microlayers. See Section 1.3.2 *State-of-the-Art Techniques* for more discussion. .... 28
- Figure 2.1.** Diagram of the dual path flow set-up. (1) helium tank; (2) mass flow controllers; (3) bubbler filled with volatile organic compound (liquid); (4) on-off valves; (5) three-way valve that allows vapor from only one upstream path to flow to the sample, only used in on-off experiments and replaced with an all-through three-way joint when recording isotherms; (6) Teflon flow chamber with inlet from the flow system, outlet to the exhaust, and optical window (fused silica). .... 36
- Figure 2.2.** Representative ssp-polarized vibrational SFG spectra in the C-H region of n-hexane, n-octane, cyclohexane and cyclooctane vapor in contact with vapor/fused silica interfaces. Intensities are normalized to the maximum peak intensity of each spectrum. Band assignments are summarized in **Table 2.1** and discussed in detail in the text. .... 38
- Figure 2.3.** Intensity averages of several on-off traces for cyclooctane, n-octane, cyclohexane, n-hexane, R-(+)-limonene, (-)- $\beta$ -pinene, (-)- $\alpha$ -pinene and (+)-3-carene vapor, normalized to the maximum ssp-polarized SFG signal intensity. Error bars at 1440 s and 3240 s of each trace are shown. .... 40
- Figure 2.4.** Average adsorption isotherms of all the organic compounds on fused silica at 22 °C and Langmuir model fits (lines). For clarity, pressure ranges 0 – 3.5 torr (A), 0 – 13 torr (B), 0 – 140 torr (C) are shown separately, and shadings with the same color indicate the same range. For 3-carene, only the sub-monolayer coverage regime of the adsorption isotherm is shown. The full isotherm of 3-carene is included in **Figure 2.5**. .... 43
- Figure 2.5.** Average adsorption isotherms of n-hexane, cyclohexane, n-octane, cyclooctane, (-)- $\alpha$ -pinene, (-)- $\beta$ -pinene, R-(+)-limonene, and (+)-3-carene at vapor/fused silica interface and Langmuir adsorption model fits (red lines). Fitting results are summarized in Table S2. For the adsorption isotherm of (+)-3-carene, the Langmuir model is fit only to the sub-monolayer regime at low pressure. .... 44
- Figure 2.6.** Adsorption free energy vs. terpene/VOC equilibrium vapor pressure at room temperature. Error bars (**Table 2.2**) are smaller than the circle diameters. .... 45

**Figure 2.7.** (A) ssp-Polarized SFG spectra of cyclohexane at the vapor/fused silica interface at different partial pressures, offset for clarity. (B)–(E) E-field ratio of the ( $r^-$  or  $d^-$ ) mode over the ( $r^+$  or  $d^+$ ) mode plotted against VOC partial pressure for cyclohexane, cyclooctane, hexane and octane at the vapor/fused silica interface. (F) Measured adsorption isotherm of cyclohexane at the vapor/fused silica interface (black dots) and Langmuir model fit (red line), and computed isotherm models for assessing upper and lower bounds due to orientational changes with  $P_{\text{cyclohexane}}$  (blue dots) and corresponding Langmuir model fits (blue lines)..... 47

**Figure 2.8.** Representative ssp-polarized SFG spectra of (–)- $\alpha$ -pinene (A), (–)- $\beta$ -pinene (B), R-(+)-limonene (C), and (+)-3-carene (D) at the vapor/fused silica interface at different vapor pressures..... 49

**Figure 2.9.** (A) The color-coded SFG spectra of  $\alpha$ -pinene adsorbed to  $\text{CaF}_2$  surface recorded every 0.3 second over a period of 3 min. (B) The final spectrum acquired for 0.3 seconds at 3 min. (C) The corresponding integrated spectral intensity every 0.3 second over time, with logarithmic time axis in the inset..... 52

**Figure 2.10.** Schematic of the most updated flow setup..... 53

**Figure 2.11.** Schematic of the two types of flow cells in internal and external geometry..... 54

**Figure 2.12.** ssp-Polarized SFG spectra of VOC vapor (black), SOA (grey), adsorbed VOC vapor (blue), adsorbed VOC vapor after ozone flow (green) for  $\alpha$ -pinene (left) and  $\beta$ -caryophyllene (right). ..... 55

**Figure 2.13.** ssp-Polarized SFG spectra of  $\alpha$ -pinene before and after ozone flow (300 – 700 ppm). Left:  $\text{CaF}_2$  substrate in the internal geometry; Middle: atomic layer deposited (ALD)  $\text{SiO}_2$  on  $\text{CaF}_2$  substrate in the internal geometry; Right:  $\text{SiO}_2$  substrate in the external geometry. .... 56

**Figure 2.14.** ssp-Polarized SFG spectra of  $\beta$ -caryophyllene, adsorbed on  $\text{CaF}_2$ , after helium rinse and after ozone flow (200 – 300 ppm)..... 57

**Figure 2.15.** ssp-Polarized SFG spectra of  $\beta$ -caryophyllene, adsorbed on  $\text{SiO}_2$ , after helium rinse and after ozone flow..... 57

**Figure 3.1.** An illustration of the combined spectroscopic and atomistic modeling approaches to elucidate the conformational and orientational preferences of squalene at the air/oil interface and collisions with ozone..... 73

**Figure 3.2.** Snapshot with view on the squalene/vacuum interface. The black lines show the simulation cell. The system is 3D periodic. The color code for the interfacial atoms is as follows: blue  $\rightarrow$  methyl groups; orange  $\rightarrow$  methylene groups; red  $\rightarrow$  vinylic C–H groups..... 75

**Figure 3.3.** Top: A representative 3D optical image of a spin-coated squalene film on fused silica, with the height profile shown at  $Y = 180 \mu\text{m}$  (yellow line). “Height 0” was set to the lowest height on the image. Laser spot size used in the SFG experiments indicated by a white circle. Bottom: A representative ssp-polarized vibrational SFG spectrum of the surface of a squalene film..... 78



**Figure 3.4.** Replicates of ssp-, ppp-, and sps-polarized SFG spectra of the surface of squalene films on fused silica. .... 79

**Figure 3.5.** Spectral fitting of a representative ssp-polarized SFG spectrum of an air/squalene interface..... 81

**Figure 3.6.** Position-dependent correlation functions,  $g(z)$ , for various parts of a squalene molecule. .... 82

**Figure 3.7.** *Left:* Distribution of the methylene bridge dihedral angles. An angular cutoff of  $120^\circ$  was used to separate the two states. *Center:* Populations of squalene conformers with zero to five gauche defects, both in the bulk and in the interface (empirically defined through the molecular center of mass position,  $z_{\text{com}} \geq 15 \text{ \AA}$ , cf. **Figure 3.7**). *Right:* In row-major order, snapshots of randomly selected squalene conformers with zero to five gauche defects. .... 83

**Figure 3.8.** *Top row:* Joint probability densities between group center of mass position and group dipole moment orientation,  $p(z_{\text{group}}, \cos\theta)$ , for methyl, methylene, and vinylic C–H groups. Values of  $\cos\theta = 1$  correspond to alignment with the surface normal. *Bottom row:* Probability density differences relative to the bulk density. .... 85

**Figure 3.9.** Computed gas-phase IR and Raman spectra, as well as group contributions. The measured SFG spectrum has been overlaid (shaded curve) to guide the eye. Computed line spectra have been convoluted with Lorentzian functions with a full width at half maximum of  $20 \text{ cm}^{-1}$ . Frequencies were scaled by a constant to match the experimental peaks. See Supporting Information section SI.3 for details on the identification of group contributions. For Raman spectra, the polarization of the incident and scattered beams is given in parentheses. .... 87

**Figure 3.10.** Top panel: Experimental liquid-phase IR spectrum and computed gas-phase IR spectrum (DFT/B3LYP/cc-pVTZ) for squalene. The data was extracted through digitization of Figure 3 in ref. 272. Bottom panel: Experimental SFG spectrum and computed gas-phase IR spectrum (DFT-D4/TPSSh/def2-TZVP) for squalene obtained in this work. The spectra in this work have been convoluted with broader Lorentzian functions. .... 88

**Figure 3.11.** Position-dependent ozone–double-bond collision rates,  $c_{\text{O}_3\text{-DB}}$ ..... 90

**Figure 3.12.** Representative ssp-polarized SFG spectra of squalene before (in green) and after (in orange) ozone flow. The helium flow was employed to adjust the RH. During the experiment, the RH was maintained at 40%. The ozone concentration was at 30 – 50 ppb. The shaded area indicates the wavenumber ranges of the integration of the two peak areas, which are used in kinetic analysis. .... 93

**Figure 3.13.** The peak areas of the two peaks in the ssp-polarized SFG spectra of squalene during ozonolysis over a time period of 40 min. The time zero is marked with a red dashed line..... 94

**Figure 3.14.** Representative ssp-polarized SFG spectra of two skin oil samples, collected on two different days, before and after 20 minutes of ozone flow. The helium flow was employed to adjust the RH. On the left, the RH was maintained below 5% and the ozone concentration was 1 – 1.2

ppm. On the right, the RH was maintained around 50% and the ozone concentration was about 0.5 ppm. .... 18  
ppm. .... 95

**Figure 3.15.** Participants responses to some survey questions regarding their home environments. .... 99

**Figure 4.1.** Schematic of the sum frequency scattering setup with the femtosecond, kHz Spectra-Physics Solstice /TOPAS laser system. Only the detection angles of 0 and 90 degrees are shown. Please refer to the text for details about the design and the part numbers. .... 109

**Figure 4.2.** The reflection SFG spectrum of a gold window (normalized to the maximum signal) and the transmission SFG spectra of a 1-mm thick piece of quartz (normalized to the maximum signal in the spp-polarized spectrum). The SFG signal of the gold did not pass through a polarizer but the incident visible and IR beams were both p polarized. The quartz spectra were taken with three polarization combinations. .... 111

## List of Tables

<b>Table 2.1.</b> Band assignments of features of spectra in <b>Figure 2.2</b> . IR wavenumbers in $\text{cm}^{-1}$ are recorded for each band.....	39
<b>Table 2.2.</b> A summary of equilibrium vapor pressures, standard adsorption free energies obtained from adsorption isotherms, and adsorption reversibility ranges obtained from on-off traces of the hydrocarbons studied in this work. ....	41
<b>Table 2.3.</b> Fit parameters (the normalization factor $a$ and the adsorption equilibrium constant $K$ ) for the adsorption isotherms of each compound to the Langmuir model. ....	44
<b>Table 3.1.</b> Spectral fitting results of the representative ssp-polarized SFG spectrum of an air/squalene interface. ....	81
<b>Table 3.2.</b> Summary of available methods to be used for analyzing indoor surface samples.....	96

## CHAPTER 1

### Introduction to Surface Chemistry in Atmospheric and Indoor Environments

#### Portions of this chapter appear in the following publications:

Liu, Y.; Bé, A. G.; Or, V. W.; Alves, M. R.; Grassian, V. H.; Geiger, F. M., Challenges and Opportunities in Molecular-Level Indoor Surface Chemistry and Physics. *Cell Reports Physical Science* **2020**, 1, 100256. <https://doi.org/10.1016/j.xcrp.2020.100256>.

von Domaros, M.; Liu, Y.; Butman, J. L.; Perlt, E.; Geiger, F. M.; Tobias, D. J., Molecular Orientation at the Squalene/Air Interface from Sum Frequency Generation Spectroscopy and Atomistic Modeling. *The Journal of Physical Chemistry B* **2021**, 125, 3932-3941. <https://doi.org/10.1021/acs.jpcc.0c11158>. Copyright [2021] American Chemical Society.

## 1.1 Heterogeneous Processes on the Surfaces of Atmospheric Aerosols

An aerosol is defined as a suspension of solid particles and/or liquid droplets in a volume of gas.<sup>1</sup> Atmospheric aerosols can be generated from natural sources such as sea spray and volcanic activities, or anthropogenic sources such as the burning of biomass and fossil fuels.<sup>2-4</sup> Besides this direct emission of primary aerosols into the atmosphere, secondary aerosols can also be formed from gas-phase molecules in the atmosphere through gas-to-particle conversion processes.<sup>3, 5-6</sup> Due to their long lifetimes in the troposphere (up to weeks) and lower stratosphere (up to years), atmospheric aerosols play an important role in the climate system by reflecting and scattering solar radiation,<sup>7-8</sup> serving as cloud condensation nuclei (CCN),<sup>9-11</sup> and participating in heterogeneous chemical reactions in the atmosphere (**Figure 1.1**).<sup>6, 12-14</sup> However, due to the low level of scientific understanding regarding the formation, composition, and properties of aerosols, large uncertainty regarding their impacts on the climate system remains.<sup>14-15</sup> This thesis contributes to narrowing this knowledge gap by specifically exploring interfacial processes that are relevant to the formation, evolution, and CCN activity of secondary organic aerosols (SOAs).

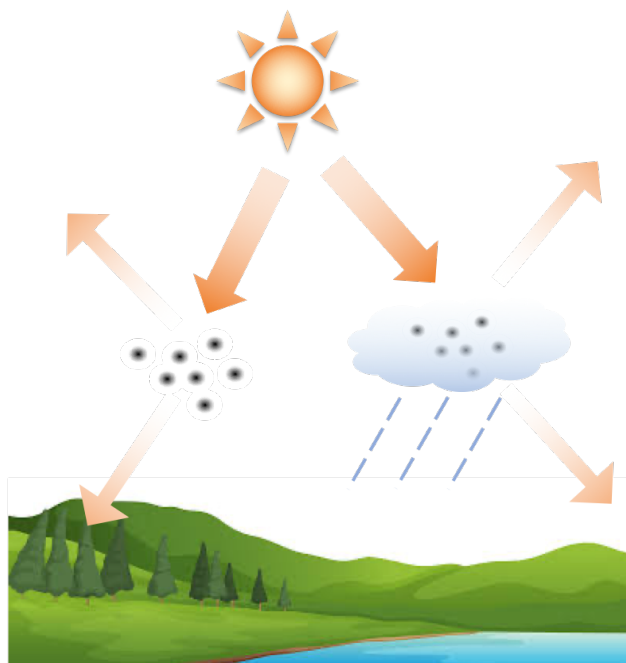


**Figure 1.1.** An illustration of role of aerosols in the climate system and in the atmosphere.

Organic compounds usually constitute a substantial portion of the total mass of aerosol particles in the environment, reaching as high as 90% in tropical forests.<sup>3, 16-17</sup> In large forest systems, through model estimation and field measurements, it has been shown that a dominant fraction of the organic particulate matter is biogenic SOAs.<sup>6, 18-19</sup> The formation of biogenic SOAs starts with the emission of volatile organic compounds (VOCs) from plants. Monoterpenes, as common SOA precursors, are estimated to comprise 15% of the annual global biogenic VOC flux in the atmosphere.<sup>20</sup> The VOCs undergo gas-phase reactions to form less volatile oxidation products and subsequently form particles through gas-to-particle conversion processes such as nucleation, condensation, and coagulation.<sup>3, 6, 14, 18, 21-23</sup> After the initial particles are formed, they continue interacting with the gas-phase species, which may result in changes to the size, composition, physical properties, and reactivity of SOAs.<sup>13, 23-27</sup> This work focuses on heterogeneous processes occurring at the gas/particle interface because the aerosol surface is the

first entity encountered by incoming gas-phase molecules.

One objective of this thesis is to explore the physical and chemical transformations at the gas/particle interface of SOAs under dynamic atmospheric conditions. The investigation includes (1) quantifying the thermodynamic parameters, (2) monitoring the transformation progress, and (3) exploring the molecular origin of the transformations. The molecular picture of the gas/particle interface this work seeks to describe will ultimately further the understanding of the formation, growth, and CCN activity of SOAs.

## **1.2 Molecular-Level Indoor Surface Chemistry and Physics**

The indoor environment is where we spend the vast majority of our time, be it at home or at work.<sup>28</sup> While much of the time, we take clean indoor air for granted, research shows that indoor air can be more polluted than outdoor air, with potential links to human health problems like chronic fatigue, asthma, and sick building syndrome. Yet, there is still a lack of mechanistic insights connecting health outcomes with indoor air quality and indoor air chemistry, making studies on this topic a frontier in environmental and health sciences, as has been especially highlighted by the current COVID-19 pandemic.

Indoor surface-to-volume ratios are considerably higher than outdoors.<sup>29</sup> Through processes collectively referred to as “sorption”, surfaces have long been considered important for regulating physical and chemical transformations that gas-phase species undergo indoors.<sup>30-32</sup> Microlayers, or thin films, formed from surface deposition and absorption following the initially adsorbed monolayer, are common indoors. These thin films are sometimes categorized within the at-times vaguely defined concept of “surfaces”. However, from a molecular perspective, a thin film is composed of Ångstrom to nanometer-thin surface, containing the topmost layer or two of

molecules in direct contact with the gas phase, and a micrometer-thick bulk phase underneath (**Figure 1.2**). The two regions are not necessarily homogeneous at a molecular level, even for aqueous solutions.<sup>33-34</sup> We have learned from atmospheric aerosol studies that the extent of mass transfer between the surface and the bulk is usually indicated by the viscosities and diffusivities in the various regions, and that such mass transfer depends on relative humidity (RH).<sup>35-38</sup> When the RH is low, mass transfer can be slowed down or inhibited, and the surface in turn plays a larger role in dictating the reactivity of the overall film. At high RH, in turn, diffusivities increase and the bulk film is accessible to incoming reactants.

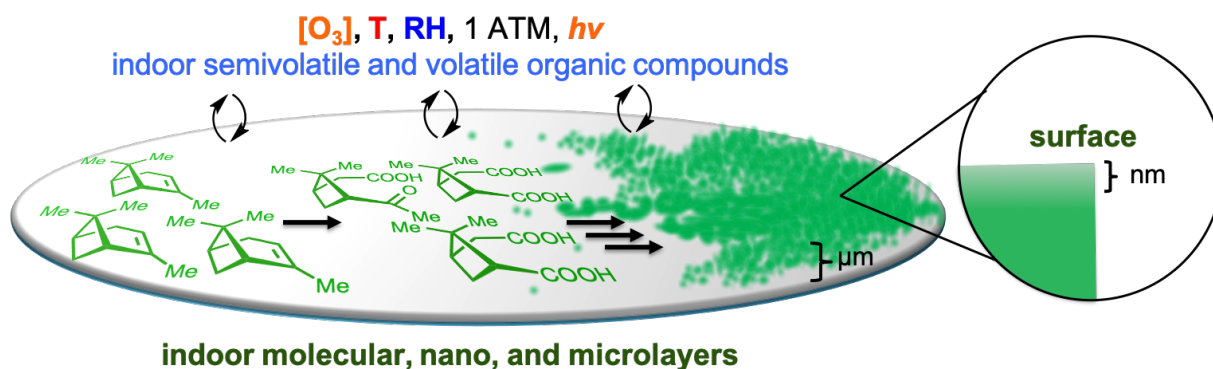


**Figure 1.2.** Indoor molecular, nano-, and microlayers form initially through the adsorption of indoor semivolatile and volatile organic compounds ( $\alpha$ -pinene as an example) to engineered indoor surfaces. The new physical and chemical properties of these surfaces need to be understood from a molecular perspective with techniques that are applicable under ambient conditions relevant to indoor environments.

As discussed in the Review by Ault *et al.*,<sup>39</sup> surface-specific molecular-level studies on the surface processes of indoor environments that are carried out under ambient conditions in real time are now just beginning to emerge<sup>40-43</sup> and hold the promise of providing much needed microscopic and mechanistic insights into chemical reactivity within these indoor engineered spaces. The approach to get there will require bulk and surface-specific measurements, ideally carried out simultaneously, on the same sample, under ambient conditions. The molecular and mechanistic



insights derived from such an approach can help disentangle long-standing problems with indoor air quality on human health through dermal and inhalation exposure.<sup>44-50</sup>

### **1.3 Challenges and State-of-the-Art Techniques to Overcome Them**

*1.3.1. Challenges.* Surfaces of atmospheric aerosols and in indoor environments are inherently complex and dynamic due to the large variety of chemicals from various sources. A large portion of chemical analyses of atmospheric aerosols and indoor molecular, nano-, and microlayers is performed off-line and sometimes requires solvent extraction,<sup>41, 51-53</sup> with possible material loss of low volatility compounds during sample transportation from the field to instruments and of low solubility compounds during sample extraction. This approach can also scramble the surface chemical composition with that of the bulk phase. Another drawback is that off-line analysis is restricted to low time resolutions, typically on the scale of days to months. As a result, processes and transformations occurring on faster time scales are buried within the snapshots provided by these off-line analyses. Thus, there is a need to provide a medium in which surfaces representative of those found in the atmospheric and indoor environments can be recreated and reacted in a controlled environment, allowing for specific surface processes to be probed. Techniques capable of on-line analysis in actual indoor environments are also needed to directly monitor dynamic changes in real time. Certain fast kinetic processes require a time resolution on the order of seconds or better.

It is important to conduct experiments under ambient conditions, including pressure, temperature, and RH, relevant to atmospheric and indoor settings. Ultra-high vacuum (UHV), usually ideal for electron or X-ray based techniques in surface studies, can lead to the evaporation of volatile compounds and thus bias the results. Typical concentrations of VOCs and oxidants need

to be paid attention to as well. For example, indoor ozone concentration levels vary with multiple factors such as outdoor ozone concentrations, ventilation rates, and indoor surface chemical reactions, but typically lie below 50 ppb.<sup>54</sup>

In order to characterize a *surface* at a molecular level, as defined in the previous section, one needs to be able to selectively probe the actual surface, which can be challenging because surface information is easily overwhelmed by bulk signals in many experimental techniques. The thickness of or the depth beneath a surface that a technique can probe should be considered (for instance, evanescent wave profile in attenuated total reflection (ATR) or dielectric constant profile in nonlinear optics).

Progress is also needed towards capturing an understanding of the adsorption of the initial monolayer in order to fully model the formation and evolution of atmospheric aerosols and indoor microlayers.<sup>55-56</sup> The surfaces of engineered indoor materials are almost always covered by matter. However, every time we clean up a surface, we remove the majority, if not all, of the material on the surface and a new film starts to grow from the initial monolayer. Moreover, an aged film of a particular composition, X, can serve as a host for a new initial monolayer of a different composition, Y. The detection of these initial monolayers requires high-sensitivity analytical techniques with adequate chemical contrast, which is usually difficult to achieve under ambient conditions.

It should be noted that, in indoor environments, many of the compounds can stay on surfaces for years and can follow different longer time-scale reaction pathways than their airborne counterparts, which are typically restricted to reactions that occur faster than the air exchange rates. The presence of these “aged” chemicals adds to the complexity of real-world indoor surfaces and the difficulty of carrying out laboratory studies to mimic practical scenarios.

1.3.2. *State-of-the-Art Techniques*. No single technique overcomes all of the challenges while providing all aspects of the molecular information needed. Instead, a successful approach may combine and integrate data from multiple state-of-the-art surface-, thin film- or aerosol-, and bulk-specific analytics (**Figure 1.3**). There exist literature reviews that comprehensively summarize techniques that are applicable to indoor surface chemistry<sup>39, 51</sup> or atmospheric aerosol chemistry.<sup>53, 57</sup> Herein a brief overview of some examples highlighting the utility of such techniques in indoor surface chemistry is provided. Mass spectrometry is widely applied in indoor air chemistry for its power in molecular or elemental identification.<sup>51, 58-62</sup> For thin film analysis particularly, chemical ionization mass spectrometry (CIMS)<sup>63-64</sup> and proton transfer reaction-mass spectrometry (PTR-MS)<sup>59-60, 65-66</sup> have been used for characterizing gas-phase products of heterogeneous reactions. Condensed phase products have been successfully probed on-line at ambient pressure by direct analysis in real time-mass spectrometry (DART-MS)<sup>67-72</sup> and off-line by gas<sup>72-73</sup> or liquid<sup>71, 74</sup> chromatography-mass spectrometry (GC- or LC-MS). The elemental composition of surface deposition in indoor environments can be analyzed by off-line aerosol mass spectrometry (AMS) following sample collection and extraction.<sup>75</sup> Electron microscopy coupled with elemental mapping and other X-ray based techniques, widely used for identifying elements present in atmospheric aerosol samples,<sup>57, 76-77</sup> has also been applied in indoor particulate matter studies.<sup>78</sup> For surface process or thin film analysis, vibrational spectroscopy is particularly useful in that it provides chemical bond information *in situ* and in real time with high time resolution under ambient conditions. One can deduce information such as surface pH values<sup>79-80</sup> and thermodynamics<sup>43, 81</sup> and kinetics<sup>42, 70, 73, 82-83</sup> of surface interactions from vibrational spectroscopic analysis.

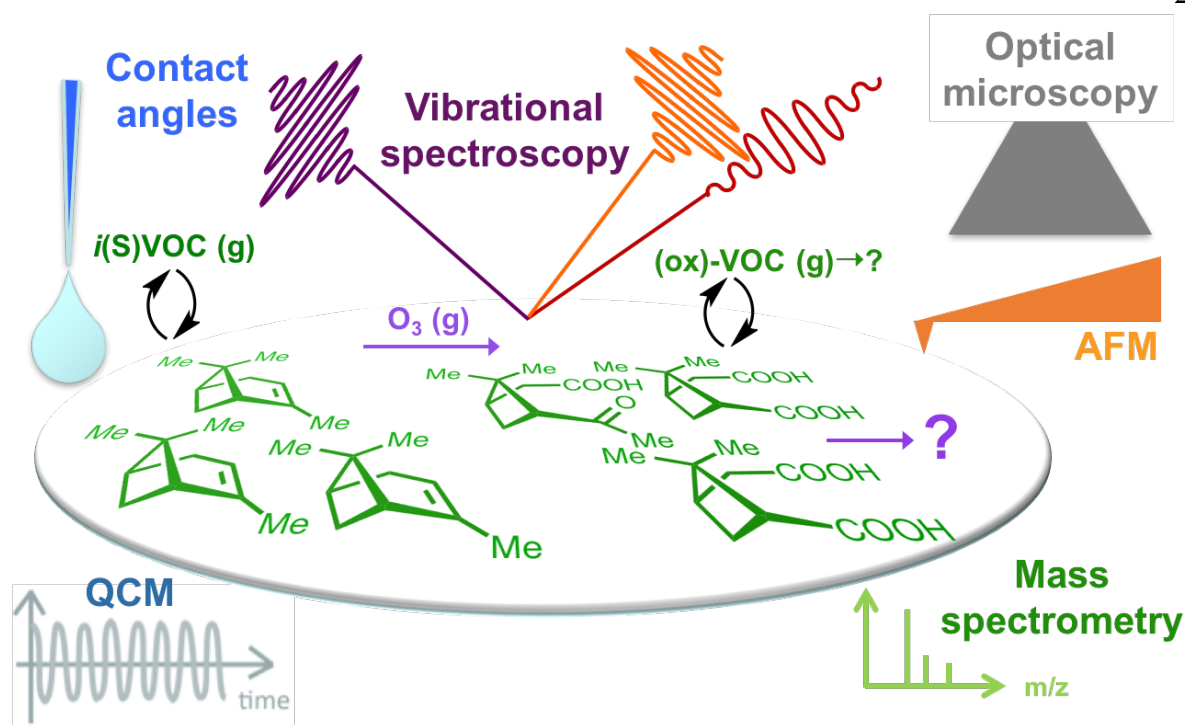


**Figure 1.3.** Multi-pronged approach for probing the surface physics and chemistry of indoor molecular, nano-, and microlayers. See Section 1.3.2 *State-of-the-Art Techniques* for more discussion.

Besides the aforementioned techniques, some analytical techniques have not yet been widely applied in indoor chemistry but have had success in atmospheric chemistry or show promising potential. For example, the recently developed method atomic force microscopy-photothermal infrared (AFM-PTIR) spectroscopy combines the strengths of AFM and infrared (IR) spectroscopy to probe the morphology and functional groups of laboratory- and field-generated thin film samples.<sup>41, 84-85</sup> Vibrational sum frequency generation (SFG) spectroscopy holds the promise of complementing other techniques by providing surface specific information.<sup>19, 86-100</sup> As with other vibrational spectroscopic tools, SFG spectroscopy probes functional groups on surfaces nondestructively under ambient condition in an on-line manner. In addition, contact angle goniometry<sup>88</sup> and pendant drop tensiometry<sup>101</sup> are economical, effective, and potentially high-throughput approaches for measuring the hydrophilicity or wettability of surfaces and the surface

activity of VOCs, respectively. Quartz crystal microbalance (QCM) mass estimations can be useful for detecting the micro- or even nano-grams of chemicals adsorbed or absorbed to surfaces or pre-existing films of materials.<sup>102-105</sup>

#### 1.4 Vibrational Sum Frequency Generation (SFG) Spectroscopy

Vibrational sum frequency generation (SFG) spectroscopy is widely used for studying interfacial chemistry because it is surface selective, chemical bond specific, and non-destructive. There is a rich literature elaborating on the theoretical basis of SFG.<sup>106-108</sup> The method relies on a second-order optical process that occurs when two light fields overlap spatially and temporarily at an interface and generate an output light field that oscillates at the sum frequency of the two incident fields. Because this nonlinear process requires the breaking of centrosymmetry, amorphous (centrosymmetric) bulk media inherently remain spectroscopically silent, granting SFG spectroscopy its intrinsic surface selectivity.

The intensity of the output SFG signal is proportional to the effective second-order susceptibility,  $\chi_{eff}^{(2)}$ , of the interface. At the surface of an organic film, the nonresonant component of the term  $\chi_{eff}^{(2)}$  is generally small when compared to the resonant contribution. The resonant component can be written as

$$\chi_R^{(2)} = N \langle \beta_{ijk,q} \rangle \quad (1)$$

where  $N$  is the number of interfacial molecules and  $\langle \beta_{ijk,q} \rangle$  is the orientational ensemble average of the molecular hyperpolarizability tensor. For each normal mode  $q$ ,  $\beta_{ijk,q}$  is proportional to the product of the derivatives of both the polarizability,  $\alpha_{ij}$ , and dipole moment,  $\mu_k$ , with respect to the normal mode coordinate,  $Q_q$ .

$$\beta_{ijk,q} \propto \frac{\partial \alpha_{ij}}{\partial Q_q} \frac{\partial \mu_k}{\partial Q_q} \quad (2)$$

Therefore, a vibrational mode is required to be both IR and Raman active to yield SFG signal.

In addition, the three beams (output SFG, input visible, and input IR) are all polarized, with *s* and *p* denoting the oscillations normal to and within the plane of incidence, respectively. For example, an *ssp*-polarized spectrum was collected with *s*-polarized sum frequency, *s*-polarized visible, and *p*-polarized infrared beams. Different polarization combinations probe selected components of the vibrational modes. For example, *ssp* and *sps* polarization combination probe the components of the vibrational modes that are oriented normal and parallel to the surface, respectively. Therefore, polarization resolved SFG spectroscopy can help us deduce the orientation of chemical bonds and, for simple molecules, even the entire molecule, especially when multiple polarization combinations are thoughtfully adopted. There is rich literature on orientational analysis with SFG spectroscopy.<sup>107-111</sup> More details will be described in Chapter 2 and Chapter 3.

Two SFG setups (Spitfire Pro and Solstice from Spectra-Physics) have been used in this thesis work, both described in detail in previous publications.<sup>91, 112</sup> The geometry of the sample interface will be described for specific experiments.

## 1.5 Thesis Scope and Organization

As discussed in this chapter of Introduction, investigating heterogeneous processes on the surfaces of SOAs can advance our understanding of the formation and evolution of aerosols in the atmosphere. In indoor environments, molecular-level studies of surfaces have just started to emerge and can provide important insights into indoor chemistry that has impacts on human health. It can be challenging to selectively probe these environmentally relevant surfaces at a molecular

level under ambient conditions. A combination of bulk-, thin film-, and surface-specific analytics need to be employed to obtain information about the different aspects of the chemical processes. Vibrational SFG spectroscopy, as an intrinsically surface selective technique that provides chemical bond information and operates under ambient conditions, is used as a main tool in this thesis.

In Chapter 2, the adsorption thermodynamics and reversibility of a suite of atmospherically relevant monoterpenes on solid surfaces are quantified using SFG spectroscopy and compared with non-terpene hydrocarbons. The partially reversible adsorption of monoterpenes to fused silica surfaces opens the possibility of studying surface-adsorbed molecules *in-situ* without needing to covalently attach them. Attempts to explore the *in-situ* monitoring of ozonolysis of surface bound  $\alpha$ -pinene and  $\beta$ -caryophyllene are demonstrated.

Chapter 3 starts with perspectives on the important research questions and experimental considerations in indoor surface chemistry. The next section presents an investigation of the molecular orientation of squalene on the surface, combining SFG spectroscopy and atomistic modeling. Molecular orientation of squalene has important implications for its ozonolysis products and rates, and preliminary data are reported. The last section of Chapter 3 describes the planning of Stay-at-HomeChem, a field campaign that aims at collecting home-derived samples during the unprecedented time when people are spending most of the time at home due to the COVID-19 pandemic.

Chapter 4 aims to expand the current capabilities of SFG spectroscopy to sum frequency scattering (SFS) of suspended aerosols. Experimental considerations, the current setup, and preliminary data of reflection and transmission SFG signal from reference samples are presented.

## CHAPTER 2

### Adsorption Thermodynamics, Reversibility, and Reactivity of Monoterpenes at Surfaces

**Portions of this chapter is reproduced from the following publication with the permission  
of AIP Publishing:**

Liu, Y.; Chase, H. M.; Geiger, F. M., Partially (Resp. Fully) Reversible Adsorption of Monoterpenes (Resp. Alkanes and Cycloalkanes) to Fused Silica. *The Journal of Chemical Physics* **2019**, 150, 074701. <https://doi.org/10.1063/1.5083585>.



## 2.1 Introduction

As mentioned in Chapter 1, monoterpenes are an important class of VOCs in environmental chemistry. They are estimated to comprise 15% of the annual global biogenic VOC flux in the atmosphere,<sup>20</sup> where they are susceptible to various chemical reactions to form less volatile oxidation products that can eventually form SOA particles.<sup>3, 6, 14, 18, 21-23</sup> In addition to gas-phase reactions, recent studies demonstrate that monoterpenes can react with preexisting aerosol particles in the condensed-phase<sup>56, 113-114</sup> or interact with the surfaces of dust aerosol particles.<sup>56</sup> Since the aerosol surface is the first entity encountered by the incoming gas-phase monoterpenes, the adsorption thermodynamics, reversibility, and reactivity of monoterpenes at the gas/solid interface can provide insight into the formation, properties, and ultimate fate of aerosol particles. Besides the implications in atmospheric chemistry, quantifying the interaction between monoterpenes and solid substrates also informs heterogeneously-catalyzed organic synthesis that employs terpenes as bio-renewable feedstocks.<sup>115-120</sup>

We recently reported experimental and computational evidence of a rotationally fluid adsorption state of  $\alpha$ -pinene on fused silica.<sup>121</sup> Thermodynamic parameters of binding and the extent of reversibility of the  $\alpha$ -pinene/silica interaction were quantified using vibrational SFG spectroscopy and molecular dynamics (MD) simulations.<sup>97</sup> We now investigate the reversibility, binding constants, and free adsorption energies of other environmentally relevant monoterpenes varying in molecular structure ( $\beta$ -pinene, limonene, and 3-carene) that rank among the most abundant monoterpenes in the atmosphere.<sup>3, 20, 122-123</sup> We then compare their interactions to common environmentally<sup>5, 124-126</sup> and industrially<sup>120, 127-128</sup> relevant cyclic and linear alkanes having equilibrium vapor pressures comparable to and exceeding those of the terpenes studied here.

## 2.2 Methods

**2.2.1 Materials.** (–)- $\alpha$ -pinene (Sigma Aldrich, Part No. P-7408, 99%), (–)- $\beta$ -pinene (Sigma Aldrich, Part No. 112089, 99%), (R)-(+)-limonene (Sigma Aldrich, Part No. 183164, 97%), (+)-3-carene (Sigma Aldrich, Part No. 21986,  $\geq 98.5\%$ ), cyclooctane (Sigma Aldrich, Part No. C109401,  $\geq 99\%$ ), Cyclohexane (EMD Millipore, Part No. 1028220500,  $>99.9\%$ ), *n*-hexane (Alfa Aesar, Part No. L09938, 99%), *n*-octane (Sigma Aldrich, Part No. 296988,  $\geq 99\%$ ), cyclohexane (EMD Millipore, Part No. 1028220500,  $>99.9\%$ ), and *n*-hexane (Alfa Aesar, Part No. L09938, 99%) were all purchased and used as received.

**2.2.2. SFG spectroscopy.** The broadband vibrational SFG spectroscopy, with the Spitfire Pro system, used in this study has been described in detail in our previous work.<sup>19, 91, 94, 96, 129</sup> Briefly, a broadband IR beam tuned to the C–H stretching region (2800 – 3200  $\text{cm}^{-1}$ ) is spatially and temporally overlapped with an 800 nm visible up-converter beam at an interface with near total internal reflection geometry at incident angles of 38 and 30 degrees, respectively, to produce an output beam that oscillates at the sum frequency of the two incident beams. The intensity of the sum frequency signal is proportional to the square modulus of the second-order susceptibility  $\chi^{(2)}$  of the material, which, in turn, determines the absorptive lineshape of the SFG spectrum.<sup>106, 130-132</sup> The spectra reported in this work were collected using the *ssp* polarization combination, corresponding to *s*-polarized sum frequency, *s*-polarized visible, and *p*-polarized infrared beams. This polarization combination probes the components of the vibrational modes that are oriented normal to the interface.

**2.2.3. Flow Setup.** The dual-path flow system was adapted from our previously published studies (**Figure 2.1**).<sup>96-97</sup> Briefly, a stream of helium gas (Ultra-High Purity Grade, 99.999%) was split into a “dry” path, through which it directly reached the sample stage, and a “wet” path, wherein it passed through a bubbler containing the VOC liquid of interest to carry the VOC vapor to the sample stage. Flow rates were controlled and monitored by digital mass flow controllers (MFCs, Alicat) for each path and are reported in standard liter per minute (SLPM). In the adsorption reversibility studies, a three-way valve was used where the two paths meet to prevent the dry path from being exposed to the VOC vapor so that the SFG signal from residual vapors in the tubing was minimized. However, when taking adsorption isotherms, an all-through three-way joint was used so that the flows from both upstream paths could get through. At the sample stage, the helium from the dry path, the VOC-saturated helium from the wet path, or a mixture of both passed through a home-built aluminum flow cell that was sealed with a Viton o-ring and a fused silica optical window (ISP Optics, Part No. QI-W-25-3) in conjunction with the described SFG setup. All the experiments were conducted at an ambient temperature maintained at 22.0 ( $\pm 0.5$ ) °C, and the relative humidity inside the sample cell was below 5% under helium flow during the experiments.

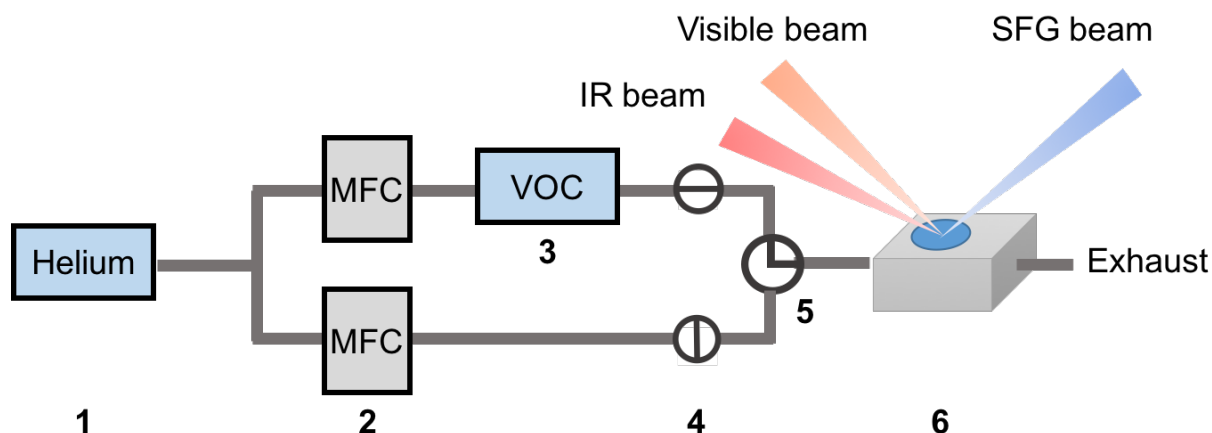


**Figure 2.1.** Diagram of the dual path flow set-up. (1) helium tank; (2) mass flow controllers; (3) bubbler filled with volatile organic compound (liquid); (4) on-off valves; (5) three-way valve that allows vapor from only one upstream path to flow to the sample, only used in on-off experiments and replaced with an all-through three-way joint when recording isotherms; (6) Teflon flow chamber with inlet from the flow system, outlet to the exhaust, and optical window (fused silica).

As shown previously,<sup>97</sup> we studied the extent of reversibility of adsorption by alternating the helium gas flow through the wet (“on”) and dry (“off”) paths while continuously recording SFG spectra. The SFG peak intensity was normalized to the maximum peak intensity over the entire course of the experiment and plotted over time to produce “on-off” traces. To obtain an adsorption isotherm of a given compound, the partial pressure of the VOC vapor in the flow cell was controlled by adjusting the flow rate ratio of helium through the wet path and the dry path. The SFG E-field magnitude, which is proportional to the square-root of the peak area, was then plotted as a function of the partial pressure of the VOC to generate an isotherm. All the on-off traces obtained are averages of duplicates or triplicates, and the isotherms are averages of at least triplicate measurements.

Before each experiment, the flow cell, the fused silica optical windows, and the Viton o-rings were sonicated in methanol (Fisher Scientific, HPLC grade), rinsed with methanol and Millipore water alternately and dried with nitrogen gas. Subsequently, the aluminum flow cell and

the optical windows were dried in an oven for an hour and then cooled to room temperature. The windows and the o-rings were plasma-cleaned for 15 min immediately prior to the experiments. The surfaces after these treatments were free of any vibrational SFG signal in the C–H stretching region.

## 2.3 Results and Discussion

**2.3.1. SFG Spectra of Acyclic and Cyclic Alkanes at Vapor/Fused Silica Interface Are in Close Agreement with Literature; First Reported Spectrum for Cyclooctane.** Representative *ssp*-polarized SFG spectra of n-hexane, n-octane, cyclohexane, and cyclooctane at vapor/fused silica interfaces, along with peak assignments, are shown in **Figure 2.2**. The SFG spectra of hexane, octane and cyclohexane are in good agreement with previously reported spectra.<sup>133-136</sup> Yet, to our knowledge, **Figure 2.2** shows the first reported SFG spectrum of cyclooctane vapor in contact with a fused silica substrate. The peak assignments (**Table 2.1**) are based on SFG reports at various interfaces<sup>137-139</sup> as well as IR studies of the bulk phase.<sup>140-141</sup>

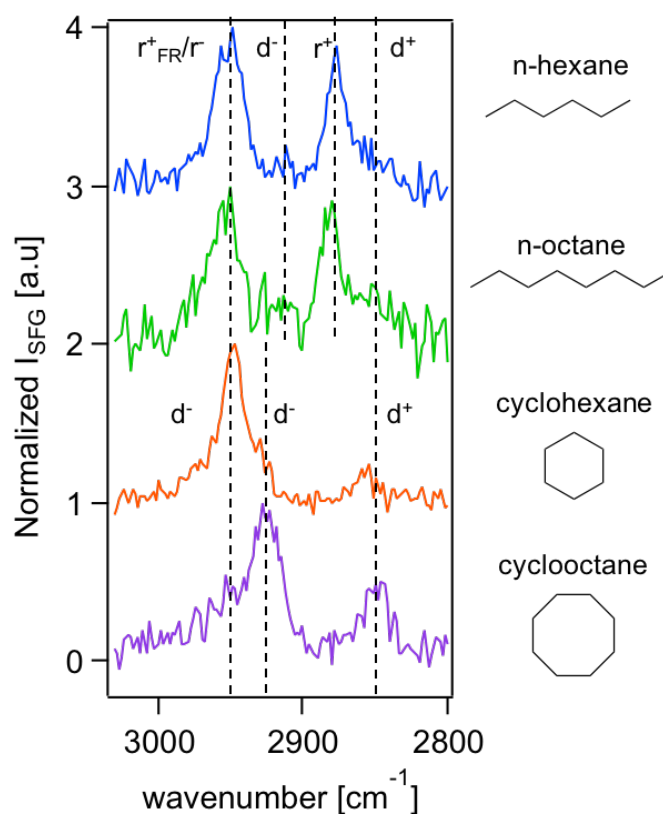


**Figure 2.2.** Representative ssp-polarized vibrational SFG spectra in the C-H region of n-hexane, n-octane, cyclohexane and cyclooctane vapor in contact with vapor/fused silica interfaces. Intensities are normalized to the maximum peak intensity of each spectrum. Band assignments are summarized in **Table 2.1** and discussed in detail in the text.

The spectra of n-hexane and n-octane are dominated by two bands centered around 2950  $\text{cm}^{-1}$  and 2880  $\text{cm}^{-1}$ . The latter band is assigned as the methyl symmetric stretch ( $r^+$ ), and the former is considered to contain contributions from both the methyl asymmetric stretch ( $r^-$ ) and the Fermi resonance of the methyl symmetric stretch ( $r^+_{\text{FR}}$ ) with the overtone of the methyl bending mode.<sup>134, 139</sup> The  $r^+_{\text{FR}}$  mode is usually centered around 2935  $\text{cm}^{-1}$ , whereas it has been reported to shift to 2940  $\text{cm}^{-1}$ , presumably as a response to the surface environment compared with the bulk.<sup>139</sup> There is a small, broad band around 2910–2930  $\text{cm}^{-1}$ , which we attribute to the methylene asymmetric stretch ( $d^-$ ), and a shoulder band around 2850  $\text{cm}^{-1}$  can be assigned to the methylene symmetric stretch ( $d^+$ ).

**Table 2.1.** Band assignments of features of spectra in **Figure 2.2**. IR wavenumbers in  $\text{cm}^{-1}$  are recorded for each band.

Hydrocarbon	$r_{\text{FR}}^+ / r^-$	$d^-$	$r^+$	$d^+$
Hexane	2948	2911	2877	2853
Octane	2949	2913	2880	2852
Cyclohexane	–	2946, 2930	–	2855
Cyclooctane	–	2949, 2926	–	2850

The SFG spectrum of cyclohexane at the vapor/silica interface shows three bands at 2946  $\text{cm}^{-1}$ , 2930  $\text{cm}^{-1}$  and 2855  $\text{cm}^{-1}$ , of which the first two modes are assigned as nondegenerate methylene asymmetric stretches ( $d^-$ ), and the lowest frequency mode as the methylene symmetric stretch ( $d^+$ ). As has been reported in literature, the  $d^-$  mode contains multiple peaks due to the coupling of methylene groups in a well-defined conformation and the highest frequency peak at 2946  $\text{cm}^{-1}$  is significantly blue-shifted due to the ring strain.<sup>133</sup> The spectrum of cyclooctane vapor exhibits similar features, with two nondegenerate asymmetric methylene stretch bands at 2949  $\text{cm}^{-1}$  and 2926  $\text{cm}^{-1}$ , and a methylene symmetric stretch band at 2850  $\text{cm}^{-1}$ . The highest frequency  $d^-$  band appears as a shoulder in contrast to a prominent peak in cyclohexane vapor spectrum.

**2.3.2. The Adsorption of Terpenes Shows Partial Reversibility While Non-Terpene Hydrocarbons Do Not.** Our previous work suggested that the extent of binding reversibility may be independent of vapor pressure because  $\alpha$ -pinene adsorption to fused silica is partially reversible at room temperature and at elevated temperatures.<sup>97</sup> Here, we report results obtained using VOCs

having a wide range of equilibrium vapor pressures, exceeding that of  $\alpha$ -pinene by a factor of up to 30 at room temperature. The averages of on-off traces of each VOC are shown in **Figure 2.3**, and the reversibility percentages are summarized in **Table 2.2** along with the equilibrium vapor pressures.<sup>142-144</sup> At 22 °C, the equilibrium vapor pressures of the terpenes are between 1.5 – 4 torr. Among the non-terpene hydrocarbons studied, the equilibrium vapor pressure of cyclooctane is 4.7 torr, close to those of terpenes, whereas n-hexane has a much higher equilibrium vapor pressure of 134 torr.

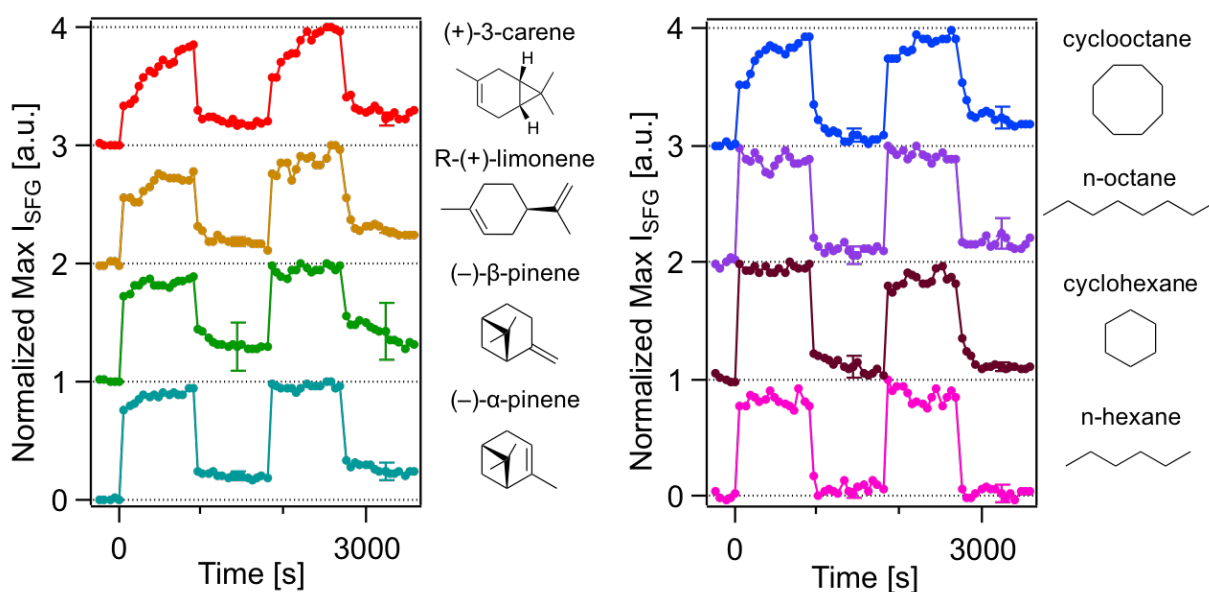


**Figure 2.3.** Intensity averages of several on-off traces for cyclooctane, n-octane, cyclohexane, n-hexane, R-(+)-limonene, (-)- $\beta$ -pinene, (-)- $\alpha$ -pinene and (+)-3-carene vapor, normalized to the maximum *spp*-polarized SFG signal intensity. Error bars at 1440 s and 3240 s of each trace are shown.

Similar to the previously demonstrated partial reversibility of  $\alpha$ -pinene, we found that the adsorption of  $\beta$ -pinene, limonene and 3-carene to fused silica is also partially reversible. Among these, the reversibility of  $\beta$ -pinene shows large variability, ranging from 40% to 90%. In contrast to the adsorption behavior of the terpenes studied, we observed full reversibility of hexane adsorption to fused silica, and large extent of reversibility of other non-terpene alkanes. Even



though the group of alkanes studied here covers a large vapor pressure range, the “intra-group” difference within the alkane group, regarding the extent of adsorption reversibility, appears to be less prominent than the “inter-group” difference between the alkane group and the terpene group. More specifically, cyclooctane in the alkane group has a comparable vapor pressure to that of  $\alpha$ -pinene, but it does not consistently exhibit partial reversibility like  $\alpha$ -pinene. Instead, the extent of reversibility of cyclooctane is more similar to that of other alkanes, despite their large vapor pressure difference. This finding suggests that vapor pressure is not a sole predictor of adsorption reversibility. There are common structural features shared among the group of terpene molecules that differentiate them from the non-terpene alkanes in regard to the adsorption behavior.

**Table 2.2.** A summary of equilibrium vapor pressures, standard adsorption free energies obtained from adsorption isotherms, and adsorption reversibility ranges obtained from on-off traces of the hydrocarbons studied in this work.

Hydrocarbon	Vapor Pressure (torr) at 22°C	$\Delta G_{\text{ads}}^{\circ}$ (kJ/mol)	% Reversibility
(+)-3-carene	1.5* <sup>142</sup>	-23.1 ± 0.2	70–85%
R-(+)-limonene	1.6 <sup>143</sup>	-20.0 ± 0.1	70–80%
(-)- $\beta$ -pinene	2.5 <sup>143</sup>	-20.6 ± 0.3	40–90%
(-)- $\alpha$ -pinene	4 <sup>143</sup>	-19.8 ± 0.2	70–85%
cyclooctane	4.7 <sup>144</sup>	-15.3 ± 0.3	80–100%
n-octane	12 <sup>143</sup>	-10.7 ± 0.5	75–100%
cyclohexane	86 <sup>143</sup>	-10.5 ± 0.2	85–100%
n-hexane	134 <sup>143</sup>	-8.1 ± 0.4	100%

\* Equilibrium vapor pressure at 22°C for (+)-3-carene could not be found in literature. 22°C is outside the valid temperature range for the Antoine equation coefficients used for (+)-3-carene in this study.

First, the group of terpenes studied in this work have molecular structures in closer proximity to a sphere-like geometry, compared to the chain- or disk-like geometries of the linear and cyclic alkanes, respectively. Our previous computational work suggests a rotationally fluid adsorption state of  $\alpha$ -pinene on fused silica with different reorientation times.<sup>121</sup> MD simulations reveal that the more tightly bound population of  $\alpha$ -pinene molecules are trapped in microscopic “pockets” at the solid surface and are thus rotation-hindered, resulting in larger van der Waals interaction with the substrate and longer reorientation times.<sup>97</sup> The distinct partial reversibility of the adsorption of the monoterpenes studied here supports this proposed mechanism in that sphere-like molecules are more likely to get trapped in “pockets” and have larger surface contact area with the substrate.

In addition, the SiO–H--- $\pi$  interaction between the silanol groups of the fused silica surface and the double bonds in the terpene molecules, which one might categorize as a weak hydrogen bond, can potentially enhance the binding. Similar partial reversibility of  $\alpha$ -pinene adsorption was also observed on a CaF<sub>2</sub> substrate, where a C=C–H---F interaction might be present. These interactions are near the weak H-bond interaction limit and the onset of van der Waals interactions.<sup>145</sup> Overall, the non-covalent interaction between the adsorbed molecules and the solid substrate is weak, thus it is not surprising that extent of reversibility can be variable and perhaps subject to small fluctuations of temperature and surface conditions. Future investigations will be carried out to more systematically evaluate the role of molecular geometry and structural variations,

such as the number and position of  $\pi$  bonds, in the adsorption of atmospherically relevant compounds to solid substrates.

**2.3.3. Gibbs Free Adsorption Energies Are Loosely Correlated with  $P_{\text{vap}}$ .** The averages of the room-temperature adsorption isotherms for each compound are shown in **Figure 2.4**, presented at low (0-3.5 torr), intermediate (0-13 torr), and high (0-140 torr) pressure ranges.

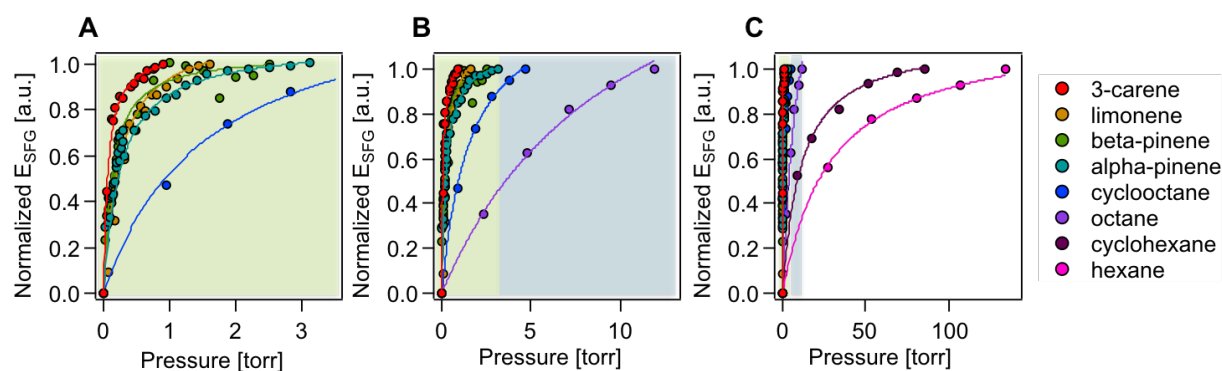


**Figure 2.4.** Average adsorption isotherms of all the organic compounds on fused silica at 22 °C and Langmuir model fits (lines). For clarity, pressure ranges 0 – 3.5 torr (A), 0 – 13 torr (B), 0 – 140 torr (C) are shown separately, and shadings with the same color indicate the same range. For 3-carene, only the sub-monolayer coverage regime of the adsorption isotherm is shown. The full isotherm of 3-carene is included in **Figure 2.5**.

Individual isotherms with error bars are shown in the **Figure 2.5**. The isotherms are fit with the Langmuir adsorption model, as discussed in our previous work,<sup>97</sup> to obtain the Gibbs free energies of adsorption ( $\Delta G^{\circ}_{\text{ads}}$ ), using 760 Torr as the standard state for adsorption from the gas phase. Except for 3-carene, the adsorption isotherms of the hydrocarbons exhibit Langmuirian sub-monolayer behavior, while the 3-carene isotherm suggests the formation of multi-layers as the vapor pressure approaches saturation. Therefore, only the sub-monolayer regime was fit with the Langmuir model in all cases.

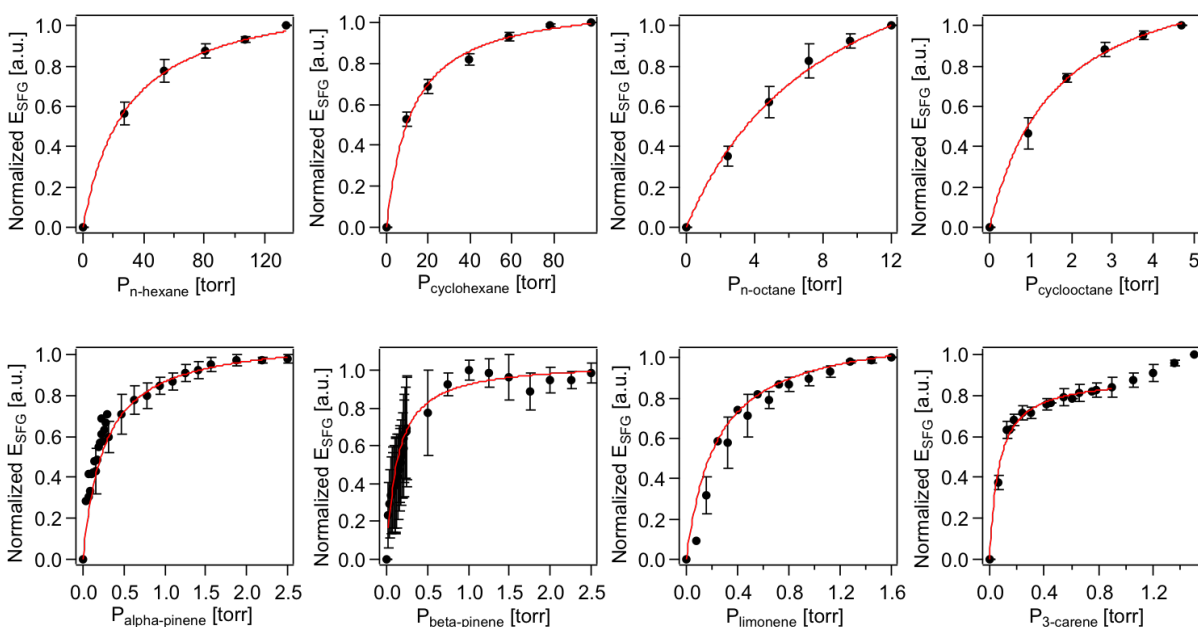


**Figure 2.5.** Average adsorption isotherms of n-hexane, cyclohexane, n-octane, cyclooctane, (-)- $\alpha$ -pinene, (-)- $\beta$ -pinene, R-(+)-limonene, and (+)-3-carene at vapor/fused silica interface and Langmuir adsorption model fits (red lines). Fitting results are summarized in Table S2. For the adsorption isotherm of (+)-3-carene, the Langmuir model is fit only to the sub-monolayer regime at low pressure.

**Table 2.3.** Fit parameters (the normalization factor  $a$  and the adsorption equilibrium constant  $K$ ) for the adsorption isotherms of each compound to the Langmuir model.

Hydrocarbon	$a$	$K$ (torr <sup>-1</sup> )	$\Delta G_{\text{ads}}^{\circ}$ (kJ/mol)
(+)-3-carene	$0.89 \pm 0.02$	$15 \pm 1$	$-23.1 \pm 0.2$
R-(+)-limonene	$1.156 \pm 0.005$	$4.28 \pm 0.06$	$-20.0 \pm 0.1$
(-)- $\beta$ -pinene	$1.05 \pm 0.02$	$8 \pm 1$	$-20.6 \pm 0.3$
(-)- $\alpha$ -pinene	$1.09 \pm 0.01$	$3.9 \pm 0.3$	$-19.8 \pm 0.2$
cyclooctane	$1.35 \pm 0.06$	$0.63 \pm 0.08$	$-15.3 \pm 0.3$
n-octane	$1.9 \pm 0.2$	$0.10 \pm 0.02$	$-10.7 \pm 0.5$
cyclohexane	$1.14 \pm 0.01$	$0.090 \pm 0.006$	$-10.5 \pm 0.2$

n-hexane	$1.18 \pm 0.04$	$0.034 \pm 0.005$	$-8.1 \pm 0.4$
----------	-----------------	-------------------	----------------

The  $\Delta G^\circ_{\text{ads}}$  values of the compounds studied are summarized in **Table 2.2**, along with the vapor pressures and percent reversibility discussed before. The  $\Delta G^\circ_{\text{ads}}$  values of the terpenes are all around -20 kJ/mol, and those of the non-terpene alkanes studied here are considerably less negative, ranging from -15 kJ/mol to -8 kJ/mol. As one can see from the plot of  $\Delta G^\circ_{\text{ads}}$  against vapor pressure (**Figure 2.6**),  $\Delta G^\circ_{\text{ads}}$  is loosely correlated with vapor pressure. Clearly, the role of molecular structure in the non-covalent interaction between the molecules and the solid surface, as discussed in the previous section, needs to be further investigated. Moreover, along with  $\Delta G^\circ_{\text{ads}}$  values, the desorption energetics of these compounds can be obtained through kinetic studies by nonlinear optical techniques<sup>146</sup> and temperature-programmed desorption<sup>147-150</sup> so that a complete potential energy profile of adsorption can be outlined for a more quantitative understanding of the adsorption process of environmentally and industrially relevant compounds.

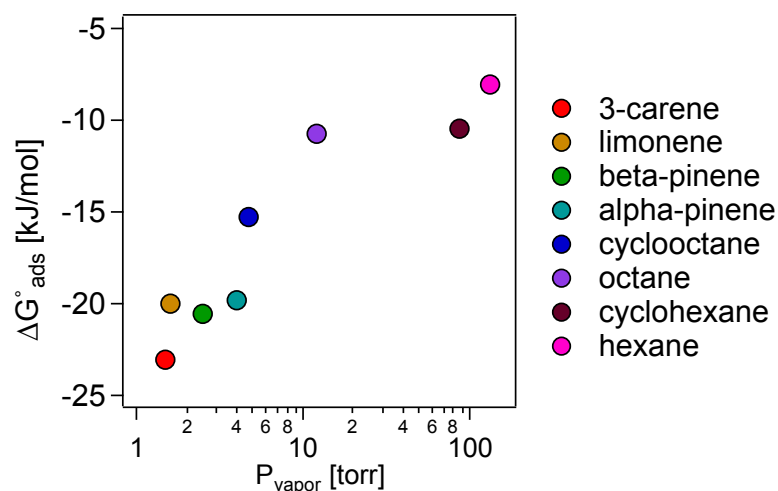


**Figure 2.6.** Adsorption free energy vs. terpene/VOC equilibrium vapor pressure at room temperature. Error bars (**Table 2.2**) are smaller than the circle diameters.

**2.3.4. Molecular Orientation Distributions Show Negligible Changes with Terpene/VOC Vapor Pressure in C-H Stretching Region Except for Cyclohexane.** Each compound studied here except for cyclohexane is orientationally invariant as the hydrocarbon vapor pressure increases, at least as assessed in the C-H stretching region (**Figure 2.7**). For cyclohexane, the SFG line shapes vary with partial pressure (**Figure 2.7A**), indicating a vapor pressure-dependent (and, by comparison to the isotherms shown in **Figure 2.4**, surface coverage-dependent) variation in the average molecular orientation at the fused silica surface. More specifically, while the asymmetric ( $d^-$ ) and symmetric methylene stretching bands ( $d^+$ ) that are consistent with literature reports<sup>133, 151</sup> are clearly present near saturation coverage, low surface coverages coincide with a lack of the  $d^+$  band, consistent with a different average orientation at low coverage. **Figure 2.7B** plots the E-field ratios of the two bands against the vapor pressure for several replicate measurements and reveals the trend observed in the isotherm shown in **Figure 2.7A**.

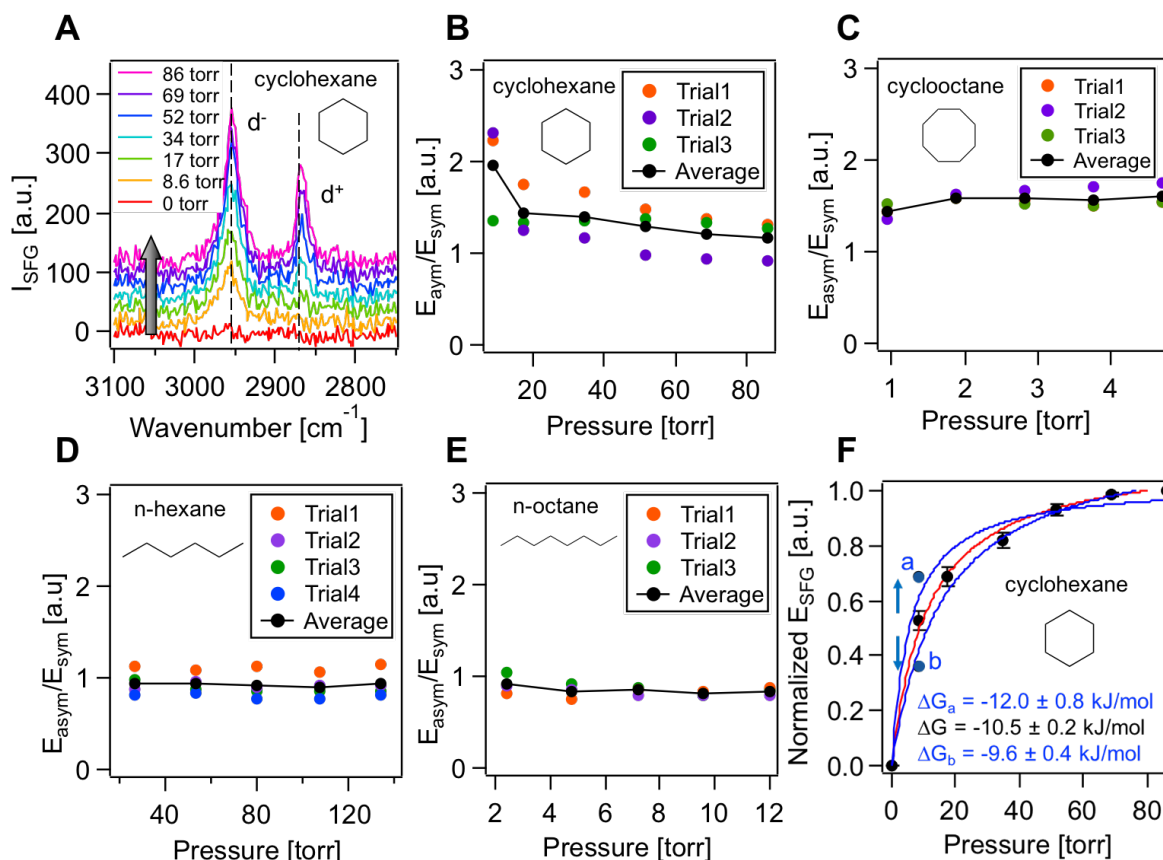


**Figure 2.7.** (A) *ssp*-Polarized SFG spectra of cyclohexane at the vapor/fused silica interface at different partial pressures, offset for clarity. (B)–(E) E-field ratio of the ( $r^-$  or  $d^-$ ) mode over the ( $r^+$  or  $d^+$ ) mode plotted against VOC partial pressure for cyclohexane, cyclooctane, hexane and octane at the vapor/fused silica interface. (F) Measured adsorption isotherm of cyclohexane at the vapor/fused silica interface (black dots) and Langmuir model fit (red line), and computed isotherm models for assessing upper and lower bounds due to orientational changes with  $P_{cyclohexane}$  (blue dots) and corresponding Langmuir model fits (blue lines).

The same analysis performed for the other alkanes (**Figure 2.7C, D, and E**) reveals that the average molecular orientation remains invariant with increasing vapor pressure. Similarly, the lineshapes of the SFG spectra obtained from the terpenes studied here do not change with partial pressure either (**Figure 2.8**), indicating the average molecular orientations of these species are invariant with terpene partial pressure. The result of this evaluation validates the current approach of linearly relating the E-field of SFG signal to the number of adsorbates and indicates that any changes in the molecular orientations have only a minor influence on the free energy of adsorption

for all the species studied here except cyclohexane at low surface coverage. To assess the significance of the average molecular orientation change to the Langmuir adsorption model fits was explored by modeling the magnitude of the SFG E-field corresponding to the lowest surface coverage, where orientation changes may occur, by upper and lower bounds of an arbitrary +30% and -30% (**Figure 2.7F**). The resulting  $\Delta G^{\circ}_{\text{ads}}$  estimates are  $-12.0 \pm 0.8$  kJ/mol and  $-9.6 \pm 0.4$  kJ/mol, not much different from the  $\Delta G^{\circ}_{\text{ads}}$  estimate obtained from the measured isotherm ( $-10.5 \pm 0.2$  kJ/mol) when compared to  $kT$ . Further investigation is needed to address the exact molecular orientation change, which we will pursue using phase-resolved SFG spectroscopy to yield the vibrational mode symmetry needed for the orientation analysis,<sup>152-154</sup> conveniently obtained using the method relative to the IEEE standard  $\alpha$ -quartz.<sup>153</sup>



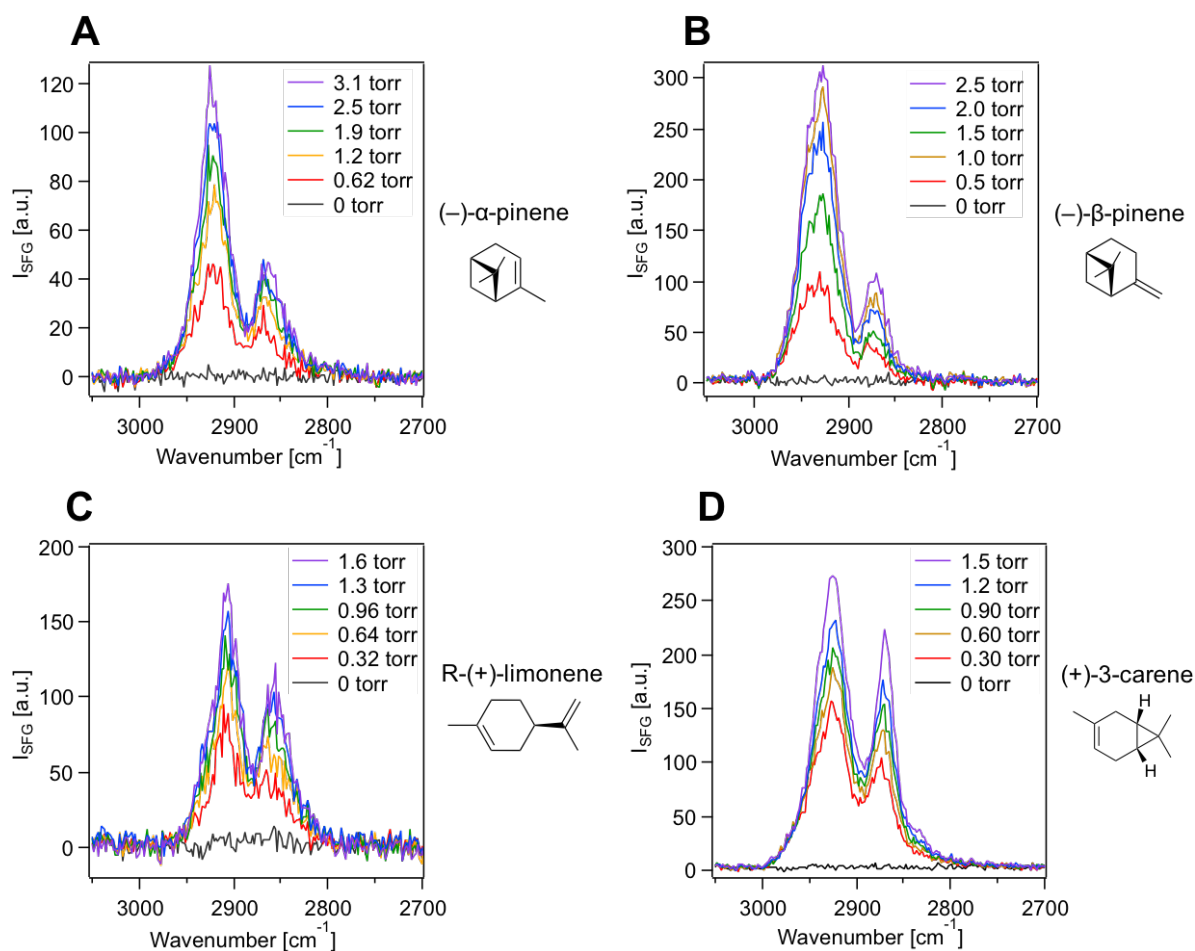


**Figure 2.8.** Representative *ssp*-polarized SFG spectra of (-)- $\alpha$ -pinene (A), (-)- $\beta$ -pinene (B), R-(+)-limonene (C), and (+)-3-carene (D) at the vapor/fused silica interface at different vapor pressures.

## 2.4 Conclusion

In conclusion, the vapor phase adsorption of four monoterpenes,  $\alpha$ -pinene,  $\beta$ -pinene, limonene and 3-carene, and four non-terpene hydrocarbons, hexane, cyclohexane, octane and cyclooctane, to fused silica was studied by SFG spectroscopy using a dual-path flow set up. The SFG spectra of the four non-terpene hydrocarbons are in good agreement with the literature. Briefly, the two linear alkanes, hexane and octane, show two major bands that are assigned as

methyl symmetric stretching and a mixture of methyl asymmetric stretching and the Fermi resonance of methyl symmetric stretching. The methylene symmetric/asymmetric stretching bands are relatively small. The two cyclic alkanes, cyclohexane and cyclooctane, exhibit a methylene symmetric stretching band and multiple non-degenerate methylene asymmetric stretching bands that are typical for molecules with ring structures.

The physical adsorption of the four monoterpenes to fused silica was shown to be partially reversible, despite the weak non-covalent interaction between the adsorbates and the solid substrate. In comparison, the non-terpene hydrocarbons studied do not consistently show partial reversibility even though their vapor pressures cover a large range, which implies that molecular structure is important for determining the adsorption dynamics and the extent of reversibility. Lastly, the adsorption free energies,  $\Delta G^{\circ}_{\text{ads}}$ , of all the compounds on the fused silica surface were determined by fitting the adsorption isotherms with the Langmuir model. Possible confounding changes in average molecular orientation to changes in SFG intensity were evaluated and found to be negligible in regard to the free adsorption energy in the limit of  $kT$  at room temperature. The information regarding the thermodynamics of hydrocarbons at the gas/solid interface is particularly important to understanding the formation of organic aerosol particles in the atmospheric and optimizing catalysts and conditions in heterogeneous catalysis.

The result of partial reversibility for the monoterpenes presented in this chapter allows for the possibility of studying the chemical reactivity of surface-bound monoterpenes towards oxidants or polymerization catalysts without the necessity of covalently attaching the monoterpenes to the surface. Indeed, the partial reversibility of terpene adsorption to solid substrates, which results in them being bound to the substrate on the timescale of days, even at elevated temperatures,<sup>97</sup> opens the possibility of studying the surface chemistry of terpenes on

optical substrates *in situ* and in real time by various linear (*e.g.*, attenuated total reflectance infrared or Raman spectroscopy) or nonlinear spectroscopic (*e.g.*, vibrational sum frequency generation spectroscopy) or surface-sensitive techniques (scanning probes, quartz crystal microbalances, microscopy). This approach has the potential to provide insights into atmospherically relevant heterogeneous processes without the limitation of short particle residence times encountered in most atmospheric flow tubes and chambers. Furthermore, compared to the previous strategy of covalently attaching the terpenes to the surface via silane or thiol chemistry,<sup>25-26, 155-160</sup> the approach allows one to follow heterogeneous processes (adsorption, reaction, desorption) with physisorbed as opposed to chemisorbed molecules.

## **2.5 Expanded Capabilities and Ongoing Research**

### **2.5.1. Higher Sensitivity of the New SFG Setup.**

With our Spectra-Physics Solstice/TOPAS system, the SFG setup can achieve sufficiently high signal-to-noise ratio at a time resolution of sub-seconds, which makes it a viable technique for studying the kinetics of surface processes. This capability is demonstrated in **Figure 2.9**.

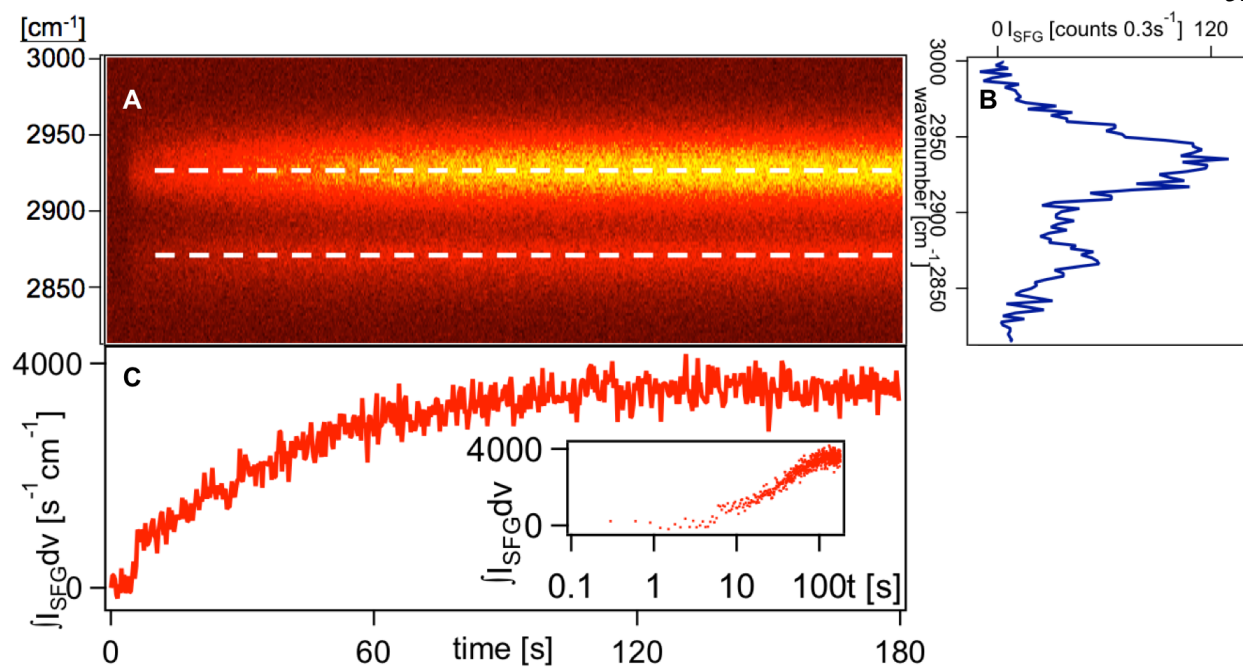


**Figure 2.9.** (A) The color-coded SFG spectra of  $\alpha$ -pinene adsorbed to  $\text{CaF}_2$  surface recorded every 0.3 second over a period of 3 min. (B) The final spectrum acquired for 0.3 seconds at 3 min. (C) The corresponding integrated spectral intensity every 0.3 second over time, with logarithmic time axis in the inset.

### 2.5.2 The Development of an Integrated and Versatile Flow Setup that Mimics the Atmospheric Environment.

An “all-in-one” flow setup (**Figure 2.10**) that has the capability of controlling multiple conditions, including RH, VOC concentration, and ozone concentration, was designed and assembled. VOC vapors and water vapor are generated by passing helium gas (Airgas, Ultra-High Purity, 99.999%) through bubblers that contain the VOCs and water. The RH detector (Omega Engineering, RH-USB) was sealed onto a home-built aluminum flow cell with the sensor inside the cell. Ozone is generated by feeding diluted oxygen (Airgas, 100 ppm or 10% oxygen in helium) into the ozone generator (Oxidation Technologies, ZO-30). The ozone generator was designed to pump in ambient air as the oxygen source. Since we have an oxygen tank as the source with a

positive pressure, the air pump in the ozone generator was disabled and bypassed. The ozone concentration is measured by an ozone analyzer (Teledyne, Model 430). The flow restrictor in the ozone analyzer was also removed and bypassed so that it won't cause a back pressure to the upstream. A by-passing loop for the ozone analyzer is incorporated for the occasions when organic vapors, which can contaminate the analyzer, are present in the system. With the aforementioned ozone generation and detection apparatus, ozone below 100 ppb, which is relevant for atmospheric and indoor environments, can be generated and monitored. As in the original simple version of flow setup, the concentrations of VOCs, water vapor, and ozone can be controlled by adjusting the flow rates of respective paths. A loop that bypasses the sample cell is designed so that the gas flow composition can be stabilized before it accesses the sample. Check valves that only allow one-way gas flow are incorporated to prevent any potential back flow.

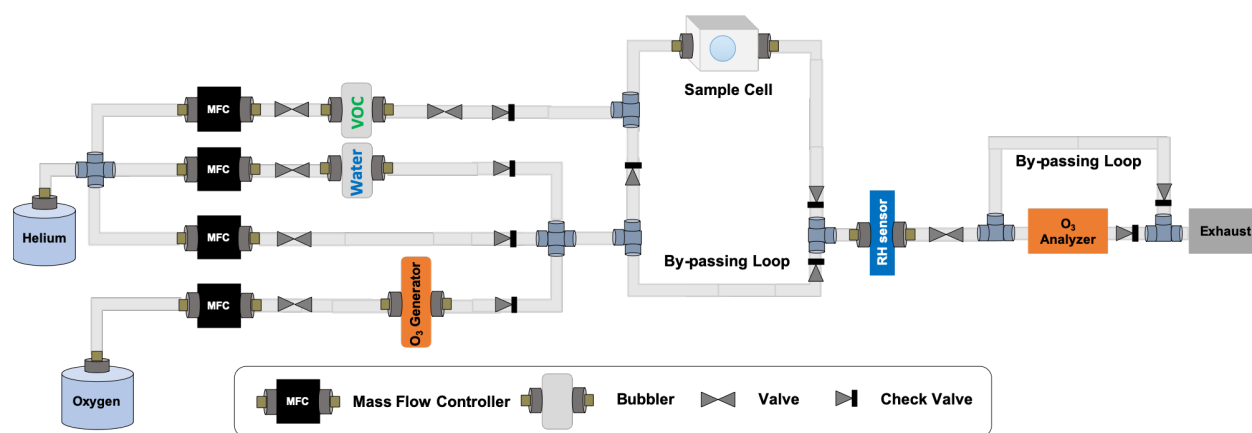


**Figure 2.10.** Schematic of the most updated flow setup.

Two types of home-built flow cells, made of Teflon or PVC, were designed to probe the air/organic or organic/substrate interface (**Figure 2.11**). The substrate is usually fused silica as a model for mineral dust in the context of atmospheric chemistry. The substrate or the cover window is clamped or screwed onto the base against O-rings to ensure air tightness.

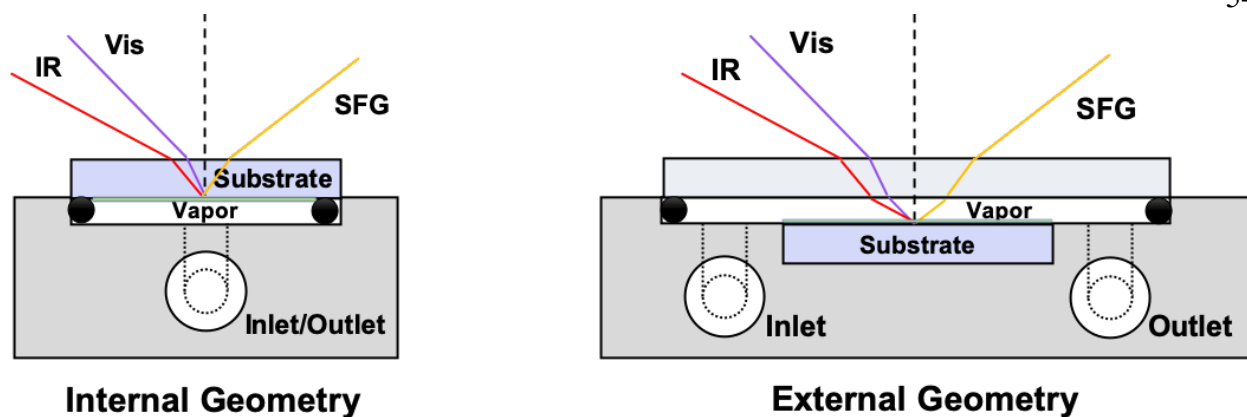


**Figure 2.11.** Schematic of the two types of flow cells in internal and external geometry.

This flow system creates a laboratory environment that simulates the real atmosphere, and the sample cell is equivalent to an environmental chamber, where various transformations occurring at the interface can be monitored *in situ* and in real time by SFG spectroscopy. With different sample cells, the flow setup can be coupled with other instruments such as QCM or optical microscope. By varying one or more factors, a wide range of experiments can be conducted to study the individual and integrated effects of environmental conditions to the formation and evolution of SOAs.

### 2.5.3 Attempts of In-Situ Monitoring of Ozonolysis of Surface-Adsorbed Terpenes

As described in Section 2.4 *Conclusion*, the partial reversibility of terpene adsorption to solid substrates allows for the possibility of probing reactivity of adsorbed molecules that are immobilized on a solid substrate. The traditional way of studying aerosol composition is generating SOAs from gas-phase chemical reactions in chambers with a certain particle residence time, and subsequently carrying out characterization. With this approach, the early stages of the physical and chemical transformations of SOAs remain undetectable. Now, the capability of

studying the surface chemistry of adsorbed terpenes on optical windows makes it possible to take *in situ*, real time measurements as reactions proceed.

In a preliminary experiment, we exposed two CaF<sub>2</sub> optical windows to  $\alpha$ -pinene vapor, and subsequently let them sit in ambient air for 10 min so that the “loosely bound” molecules desorbed and the “tightly bound” molecules remained adsorbed. Then one window was brought to an ozone chamber for ozonolysis of the adsorbed  $\alpha$ -pinene, and the other one stayed untreated. Comparing the SFG spectra in the C–H stretching region of the untreated window and the ozone-treated window (**Figure 2.12, left**), we found that the SFG peaks of the ozone-treated window showed slight blue shifts. This result is in agreement with the previous observation of the blue shifts of peaks in the  $\alpha$ -pinene derived SOA spectrum compared with the  $\alpha$ -pinene vapor spectrum.<sup>94</sup> Similar results were seen for  $\beta$ -caryophyllene, the most abundant sesquiterpene in the atmosphere (**Figure 2.12, right**). The number of distinguishable peaks in the spectrum of  $\beta$ -caryophyllene vapor decreases from three to two after ozonolysis. Even though we cannot assign the peaks to specific vibrational modes, the spectral change appeared to be distinctive.

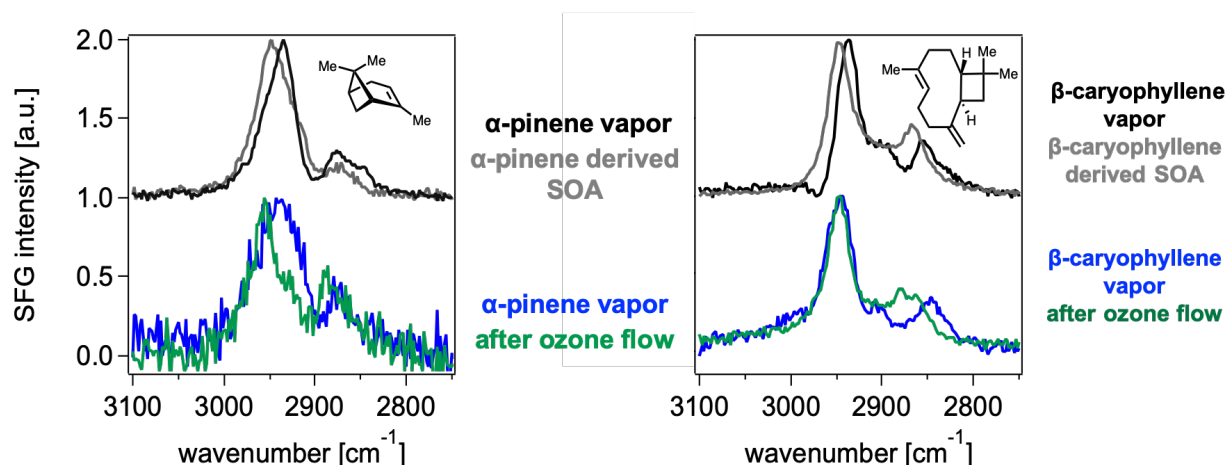


**Figure 2.12.** *ssp*-Polarized SFG spectra of VOC vapor (black), SOA (grey), adsorbed VOC vapor (blue), adsorbed VOC vapor after ozone flow (green) for  $\alpha$ -pinene (*left*) and  $\beta$ -caryophyllene (*right*).

Note that the preliminary experiments above were conducted in an “offline” manner, which means that the sample windows were taken off the sample cell, treated with very high concentrations of ozone (hundreds of ppm), and put back onto the cell for SFG measurements. The experiments were then repeated in an “online” manner with the flow setup, with the RH controlled. However, “online” measurements of  $\alpha$ -pinene spectra before and after ozonolysis have not reproduced the spectral shift even at very high concentrations of ozone (300 – 700 ppm) (**Figure 2.13**).

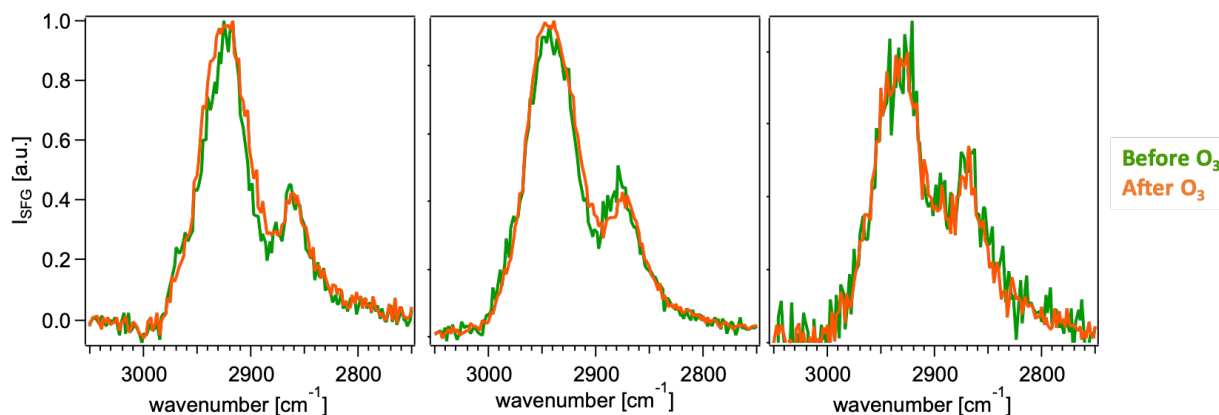


**Figure 2.13.** *ssp*-Polarized SFG spectra of  $\alpha$ -pinene before and after ozone flow (300 – 700 ppm). *Left*:  $\text{CaF}_2$  substrate in the internal geometry; *Middle*: atomic layer deposited (ALD)  $\text{SiO}_2$  on  $\text{CaF}_2$  substrate in the internal geometry; *Right*:  $\text{SiO}_2$  substrate in the external geometry.

The spectral change in the *ssp*-polarized SFG spectra of  $\beta$ -caryophyllene, adsorbed on  $\text{CaF}_2$  substrate, before and after ozone flow (200 – 300 ppm) under different RH was investigated in the internal geometry (**Figure 2.14**). However, the same experiments for  $\beta$ -caryophyllene adsorbed on  $\text{SiO}_2$  substrate exhibited inconsistent results. In some experiments, the spectrum after helium rinse only contained two peaks (**Figure 2.15**, left), whereas in other experiments, the middle peak remained present even after concentrated ozone flow (**Figure 2.15**, right).



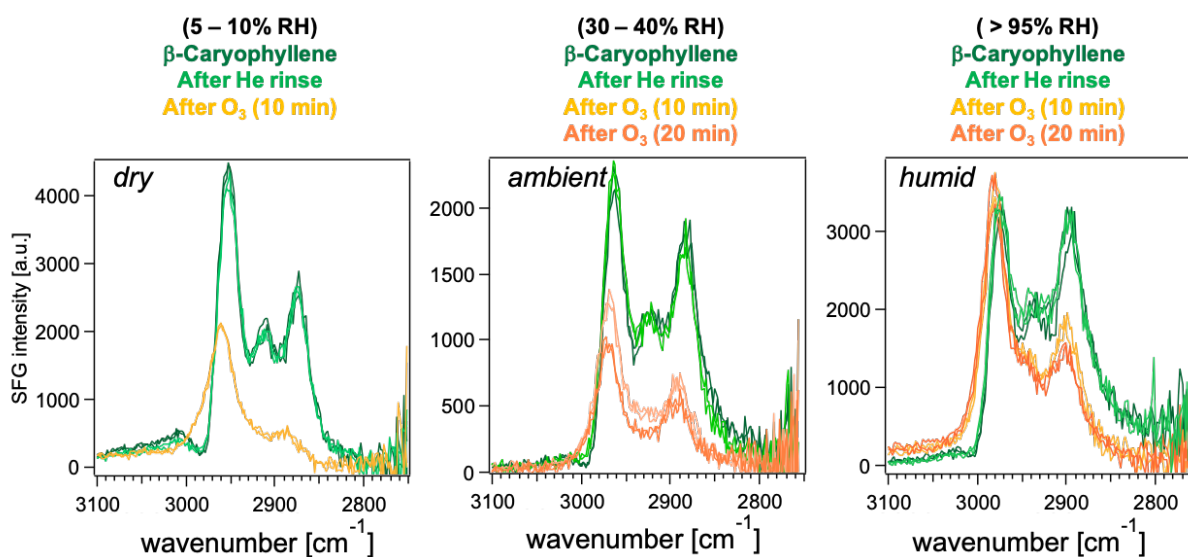


**Figure 2.14.** *sps*-Polarized SFG spectra of  $\beta$ -caryophyllene, adsorbed on  $\text{CaF}_2$ , after helium rinse and after ozone flow (200 – 300 ppm).

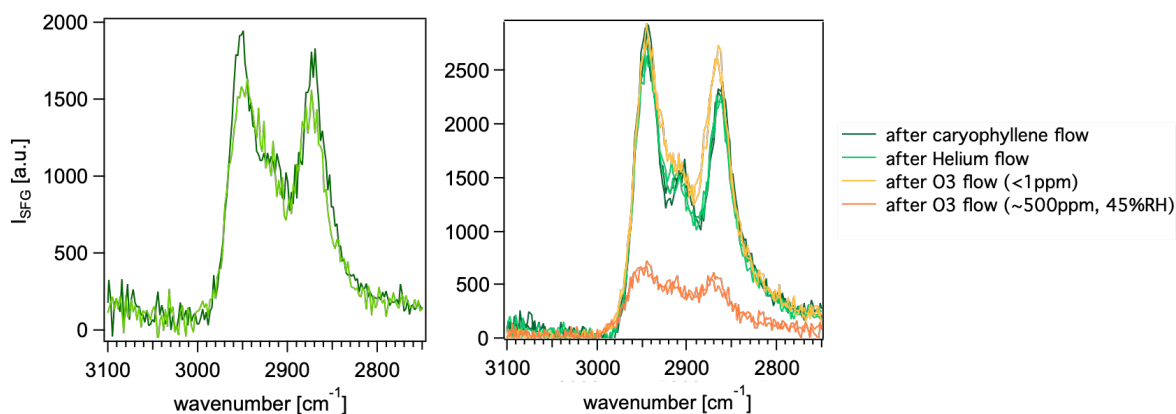


**Figure 2.15.** *sps*-Polarized SFG spectra of  $\beta$ -caryophyllene, adsorbed on  $\text{SiO}_2$ , after helium rinse and after ozone flow.

The C–H stretching region of complex organic molecules such as  $\alpha$ -pinene and  $\beta$ -caryophyllene is congested with many vibrational modes. There have been great research efforts in assigning the peaks and interpreting the spectral features.<sup>161-162</sup> Therefore, it might not be the most robust approach to track the reaction progress based on certain subtle or inconsistent spectral

changes. Since ozonolysis products contain carbonyl groups whereas terpenes do not, the SFG signal in the C=O stretching region<sup>99</sup> over the reaction can potentially serve as a simpler and more distinctive indicator of the reaction progress.

### Chapter 3

#### Molecular-Level Surface Chemistry and Physics of Indoor Air

##### Portions of this chapter appear in the following publications:

Liu, Y.; Bé, A. G.; Or, V. W.; Alves, M. R.; Grassian, V. H.; Geiger, F. M., Challenges and Opportunities in Molecular-Level Indoor Surface Chemistry and Physics. *Cell Reports Physical Science* **2020**, 1, 100256. <https://doi.org/10.1016/j.xcrp.2020.100256>.

von Domaros, M.; Liu, Y.; Butman, J. L.; Perlt, E.; Geiger, F. M.; Tobias, D. J., Molecular Orientation at the Squalene/Air Interface from Sum Frequency Generation Spectroscopy and Atomistic Modeling. *The Journal of Physical Chemistry B* **2021**, 125, 3932-3941. <https://doi.org/10.1021/acs.jpcc.0c11158>. Copyright [2021] American Chemical Society.

### 3.1 Perspectives on Research Opportunities in Indoor Surface Chemistry and Physics

Under varying conditions, engineered surfaces build up indoor molecular, nano-, and microlayers over time that exhibit dynamically changing properties. By integrating state-of-the-art surface, thin film, and bulk analytics with advanced multi-scale – from atomistic to macroscopic – computer modeling, research opportunities in indoor surface chemistry include the following fundamental questions:

- 1) How do indoor volatile and semi-volatile organic compounds (VOCs and SVOCs) and inorganic and organic aerosols adsorb or stick from air to engineered indoor surfaces? How do they build up from submonolayer amounts to nano- and microlayers to form secondary organic films?
- 2) What functional groups, with what orientation distribution, on the surfaces of indoor molecular, nano-, and microlayers present themselves to incoming gas-phase species? What role does interfacial water play in regulating the physical properties and chemical reactivities of these molecular, nano-, and microlayers?
- 3) How do indoor molecular, nano-, and microlayers react with gas-phase VOCs and oxidants, such as ozone and OH radical, heterogeneously? What are the mechanisms under various conditions?
- 4) How does the response of indoor molecular, nano-, and microlayers to gas-phase species vary under dynamic conditions of RH, moisture content, light, and temperature?

These questions have been explored to varying extents, as summarized in a number of review articles.<sup>39, 51-52, 163-166</sup> This section aims to highlight aspects that need further exploration as the field moves forward and bring out practical considerations and suggestions in research design for the community. Overall, answers to these questions are expected to help better identify and

quantify sources and sinks of indoor air pollutants, along with improving the prediction of indoor air quality dynamics. Such efforts may also enable the eventual design of coatings, paints, or other technologies that control or prevent the buildup of indoor molecular, nano-, and microlayers where needed.

### 3.1.1 Research Questions

*Adsorption Thermodynamics and Kinetics.* The thermodynamic and kinetic parameters of VOC adsorption are important inputs for models that integrate surface physical and chemical processes in indoor environments and provide valuable insights into organic film growth.<sup>55, 167-168</sup> This topic has been pursued by the indoor air chemistry community for years. A great number of experimental studies have been conducted using macroscopic and off-line approaches, which has provided valuable parametric information for film growth models.<sup>169-172</sup> On-line approaches for studying the surface adsorption and organic film absorption processes at a molecular level have emerged in recent years, among which Fourier Transform infrared (FTIR) spectroscopy is a widely employed technique that usually involves high-surface area solid particles.<sup>42-43, 81, 148-150, 173-175</sup> SFG spectroscopy, with its high sensitivity and surface selectivity, has shown success in probing the interaction between VOCs and optically reflective solid surfaces.<sup>97-98, 176</sup> The amount of VOCs adsorbed, which is an important variable in calculating adsorption and desorption rates in kinetic analysis, can be estimated by models and experimentally measured in an on-line manner using QCM. This approach will be particularly meaningful with porous materials, which are thought to be major sinks for VOCs and SVOCs.<sup>52, 177</sup> In addition, previous work has shown that adsorbed water can compete for surface adsorption sites and may interact with VOCs.<sup>81, 173-175, 178-179</sup>

Investigations of VOC adsorption should therefore be conducted under different RH and temperatures that are relevant indoors.

A molecular picture of the adsorption of VOCs on solid surfaces can be derived by combining experimental and computational methods. For example, MD simulations suggested a highly fluxional state of adsorbed  $\alpha$ -pinene on fused silica stabilized by rotational entropy and hindered rotations for more tightly bound  $\alpha$ -pinene molecules.<sup>97, 121</sup> MD insights into studies of limonene have shown the importance of  $\pi$ -hydrogen bonding interactions between the C=C double bonds of adsorbed limonene and the hydroxyl groups of SiO<sub>2</sub> surfaces.<sup>42</sup>

*Molecular Orientation.* Within the x-y plane of a surface, the orientation distributions of adsorbates are likely to be isotropic. In contrast, distributions of molecular tilt angles, relative to the surface normal, are likely far from isotropic under many conditions of temperature and RH. The key driver is the polarity difference between air and the condensed phase. The precedent comes from the field of polymer surface chemistry. Already in the early 2000's, it was shown that methyl side groups stand up in air (non-polar) and lie flat in water (polar).<sup>180</sup> On the surfaces of much more complex mixtures of indoor films, orientation distributions of functional groups such as C=C double bonds, carbonyl groups, and C-H groups, are highly likely to be similarly sensitive to water content in the immediate vicinity. A previous report on heterogeneous reactive uptake coefficients ( $\gamma$ ) plotted against gas-phase reaction probabilities for the ozonolysis of various olefins shows how the molecular orientation of C=C double bonds greatly drives chemical reactivity in a fashion that is entirely unexpected from the gas phase reactive cross sections.<sup>159</sup> This observation is consistent with our intuition that a functional group or a reactive site needs to be accessible to reactants, in terms of both spatial arrangement and molecular orbital overlap, i.e. reactive cross

section, for the reaction to occur. Previous work on C=C double bond ozonolysis has shown that reactive uptake coefficients are considerably larger when the C=C double bonds are oriented towards as opposed to away from the gas phase.<sup>26</sup> These experiments were conducted using chiral terpene derivatives, but this concept is expected to be generally important for indoor air chemistry as well. Molecular structures, including shape, functional group orientation, and chirality, along with surface properties, including hydrophilicity and microscopic texture and roughness, can dictate molecular orientation distributions at different surface coverages, temperature, and RH values.

In this respect, SFG spectroscopy is advantageous in that the signal intensity is not only proportional to the number of oscillators squared but also sensitive to the molecular orientation. Examining the line shape of the spectra at different surface coverages provides insights into possible molecular orientation changes. Polarization-resolved SFG spectra allow one to derive molecular orientations for relatively simple molecules,<sup>176</sup> and, with the help of calculations, more complex molecules. When local mode approximations are applicable, one can conduct orientation analyses using the polarization intensity ratio method<sup>107, 181</sup> or the polarization null angle method.<sup>182-185</sup> When vibrational modes are due to delocalized coupling of multiple oscillators, density functional theory (DFT)-based simulation method can serve as a reasonably affordable and accurate approach to provide molecular orientation estimates that can be used to interpret the experimental spectra.<sup>121, 186-188</sup> In order to determine the absolute molecular orientation of a particular vibrational mode (oscillator pointing up vs down), one can carry out heterodyne-detected SFG measurements by involving a quartz crystal as a reference.<sup>99, 153</sup> In addition to spectroscopic analyses, atomistic MD simulations can provide insights into molecular configurations at interfaces<sup>42-43, 121</sup> and help recapitulate experimental observables and vice versa.

With information on the molecular orientation provided by these experimental and computational methods, models of indoor air can potentially include more mechanistic details into the molecular level so as to improve accuracy and predicting capability.<sup>167</sup> One key outcome would be, for instance, the direct, real-time tracking of a C=C double bond orientation distribution as RH is increased or decreased, followed by ozonolysis, all directly at the interface of interest while simultaneously monitoring reactants and products in the gas phase above and the condensed phase below. Possible approaches are described next.

*Heterogeneous Reactions.* The high surface-to-volume ratio of indoor environments provides ample opportunity for heterogeneous reactions to occur between surface bound species and gas-phase VOCs and oxidants, such as ozone, hydroxyl radical, Cl<sub>2</sub>, and HOCl, over extended periods of time. Research has been focusing on the identification of gas-phase and condensed-phase products and the quantification of reactive uptake coefficients, which are important parameters in indoor air kinetic models.<sup>167, 189</sup> Among them, heterogeneous ozonolysis has been studied most extensively by mass spectrometry,<sup>65-69, 71, 73-74, 190-192</sup> ATR-FTIR spectroscopy,<sup>73, 82-83</sup> and SFG spectroscopy.<sup>86-88</sup>

As discussed in the section of *Molecular Orientation*, the  $\pi$ -electron system of the C=C double bonds need to be fully accessible by gas phase ozone for heterogeneous ozonolysis to be feasible. Therefore, beyond parametric studies, it is also necessary to take into account the spatial constraint of surface species when seeking a molecular-level mechanism to rationalize the distinctive kinetics of heterogeneous reactions, underscoring the importance of molecular orientation analysis.<sup>86-88, 191, 193-194</sup> In addition, earlier work on the ozonolysis of surface-bound silanized terpene derivatives<sup>86-90, 195-196</sup> has shown evidence of two reactivity modes and two



outcomes of hydrophobicity after ozonolysis, depending on ozone concentration levels. This insight is likely to be relevant for indoor air as well.<sup>197-198</sup> One should therefore sample a range of ozone concentrations when determining the reactive uptake coefficients of ozone by indoor molecular, nano-, and microlayers and evaluating the physical and chemical properties of new surface layers.

*Role of Water.* As already noted, the RH level in indoor environments largely depends on outdoor weather conditions, window locations, ventilation, and the use of heating, air conditioning and/or (de)humidifiers in each individual room. Even in homes with good humidity control, RH can temporarily spike up in local areas from certain human activities such as showering and cooking. Hence, even though RH is typically controlled between 30% and 50% for human health and comfort in modern buildings and houses, higher and lower RH levels beyond this range are not uncommon. In addition, pools of liquid water are often found indoors, be they formed through leaks, spills, or condensation due to improper ventilation in damp spaces. Such pools or thin films of liquid water can be reservoirs for water-soluble compounds and provide opportunities for bulk aqueous chemistry.<sup>199-200</sup>

The role of “sorbed” or interfacial water is even more complex. The rich literature on water acting as a plasticizer in atmospheric SOA particles<sup>36-38, 201-202</sup> is likely applicable for indoor nano- and microlayers as well. These layers are expected to exhibit different physical properties, such as viscosity and diffusivity, depending on indoor RH levels. Liquid-liquid phase separation observed in atmospheric aerosol particles at high RH<sup>203-205</sup> can also possibly occur indoors when water vapor condenses to surfaces where organic matter accumulates. Furthermore, water molecules are important in regulating surface processes.<sup>40, 206</sup> For instance, the molecular orientation distribution

at the surface of SOA particles widens considerably as the particles transform from being “marble-like” to being “honey-like” when transitioning the RH from low to high. Surface molecules are found to exhibit different extents of ordering depending on RH, as in an opened versus closed surface gate, which might in turn influence the adsorption, surface partitioning, and reactivity of the films.<sup>96</sup>

Experiments aimed at probing the hydrogen bonding environment of interfacial water molecules on the surfaces of indoor materials and molecular, nano-, and microlayers should be particularly insightful, especially when coupled with molecular simulations of water dynamics.<sup>33, 207-211</sup> Reports pairing SFG spectroscopy with MD simulations have elucidated lipid-water interactions in the tightly hydrogen bonded network of interfacial water.<sup>211</sup> Even though the tightly hydrogen-bonded water network manifests itself in the OH stretching region near  $3200\text{ cm}^{-1}$ , where ice exhibits a narrow ( $\sim 50\text{ cm}^{-1}$ ) and intense resonance,<sup>212</sup> the water molecules are unlikely to be “ice-like” but instead subject to local field effects due to net-aligned dipoles and charged species. Nevertheless, theoretical and experimental studies have shown that water near interfaces might have hindered rotational motion and thus a more ordered structure.<sup>33-34, 206, 213</sup> In general, as discussed in previous sections, this combination of experimental and computational studies is fruitful for developing a molecular picture at interfaces and presents itself as a promising toolset for the indoor chemistry community.

In the context of indoor surface chemistry, it will be important to investigate the extent and reversibility of water uptake by the indoor molecular, nano-, and microlayers under varying conditions, which can be quantified by measuring the mass change using QCM.<sup>102, 104</sup> The changes in the size, shape, and morphology of domains of the indoor molecular, nano-, and microlayers can be monitored by optical microscopy and AFM for a further understanding of the plasticizing

role of water.<sup>104</sup> Spectroscopic analysis of the structure of surface-bound molecules, such as the orientation of hydrophilic or hydrophobic moieties, at different RH levels can also be important in gaining mechanistic insights into the role of water in surface processes indoors.

*Surface Processing.* As discussed in previous sections, water plays a critical role in regulating surface processes such as the adsorption of VOCs and heterogeneous chemical reactions, and the sequence of such interplays matters. Some processes compete with each other, such as the adsorption of water and pyruvic acid,<sup>81</sup> whereas other processes work together to facilitate air/surface interactions and transformations. For example, the presence of both HOCl and Cl<sub>2</sub> promotes the formation of secondary aerosol particles from limonene.<sup>214</sup> Another example is the dissociation of nitric acid on surfaces which is facilitated at higher relative humidity to yield strongly adsorbed nitrate ions.<sup>173</sup> When designing laboratory experiments or events in field campaigns, one should therefore consider the sequence of exposure to various experimental conditions to model real-life events in indoor environments. For means of example, one may employ the following two sequences for probing two different indoor scenarios:

- 1) [*flowing indoor VOC and ozone together at low RH, stopping the flow, and then raising RH*] as a model for transitioning from daytime to nighttime, when ozone level is lower and RH is higher, and
- 2) [*flowing indoor VOC, stopping the VOC flow, flowing ozone subsequently, stopping the ozone flow, all under low RH, and then raising RH*] as a model for a daytime VOC emission event, such as house cleaning, followed by an afternoon influx of high amounts of ozone in the presence of air pollution and then nighttime humid air.

### 3.1.2 Experimental Considerations.

*From Idealized Models to Real World Surfaces.* When choosing which type of indoor surface to investigate, there are options that range from idealized model systems to the surfaces of materials present in actual homes, as well as active and passive samplers.<sup>39</sup> Idealized model surfaces can be hydrophilic (fused silica) or hydrophobic (Teflon), or be molecular (polyethylene, propylene, silicone, latex), ionic ( $\text{CaCO}_3$ ), or metallic ( $\text{Cr}(0)$ ,  $\text{Ni}(0)$ ,  $\text{Cu}(0)$ ,  $\text{Fe}(0)$ , and their thermal oxides) in nature. Surfaces of inorganic (glass, marble, concrete) and organic (natural and synthetic polymers) substrates placed in homes and offices may be selected as real-world samples or used for passive sampling. Comparing results obtained on different substrates, such as flat glass surfaces versus silica powders and actual paint versus  $\text{TiO}_2$ , provides insights into how surface morphology, roughness, and trace amounts of chemicals might influence the VOC uptake, reactivity, and fate of indoor surfaces.

*Flow System and Chambers.* Flow systems and chambers have long been utilized in almost every laboratory-based indoor surface study. A chamber provides a controllable, chemically pristine, and background aerosol-free environment, compared to a real indoor atmosphere. Chambers allow for indoor spaces to be experimentally modeled. An adjacent flow system allows the user to introduce key components normally measured in indoor field studies such as RH, temperature, VOCs and SVOCs, generated aerosol, light, and oxidants in a deliberate manner. Such setups can be coupled with on-line analytical techniques, such as SFG spectroscopy, QCM, and mass spectrometry, for direct measurements of surfaces *in-situ* and in real-time. The flow system built for atmospheric chemistry, shown in **Figure 2.10** and **Figure 2.11** in Chapter 2, can be directly employed for indoor chemistry.

Laboratory generated idealized model surfaces provide an avenue for systematic investigations into how different indoor transformation processes alter the morphology and chemical composition at the air-solid interface. By slowly building up the complexity of the exposure conditions that these mimetic surfaces are exposed to, we can begin to deconvolute how different indoor surface processes (sorption, deposition, reaction, and reemission) contribute and interplay in the evolution of indoor surfaces. By using information gathered from real-world field studies and understanding the current gaps in research regarding theoretical modeling of indoor mechanisms, laboratory generated surfaces can bridge these fields much more effortlessly by providing a distilled view of the many complex surface-specific processes that can occur in indoor spaces.

*Synthetic Standards.* VOCs and oxidized molecules of interest to indoor air processes include constituents found in or formed from paints and coatings, upholstery, tobacco smoke residues, cooking oils and greases, fragrances, and even human skin oils.<sup>163</sup> While a limited number of indoor VOCs are commercially available (e.g. limonene, squalene, acetone, acetaldehyde, formaldehyde), the vast majority of oxidation products formed via reactive pathways occurring indoors are not readily accessible. Isotopic labeling of VOCs and their oxidation products could enable detailed molecular studies of chemical reaction pathways and physicochemical heterogeneous processes occurring indoors.<sup>162, 215</sup> Such challenges offer exciting opportunities for synthetic organic chemists to contribute to the emerging field of synthetic atmospheric and indoor air chemistry.

Organic synthesis allows for access to meaningful amounts of authentic standards in pure and homogeneous form, that, when combined with physical measurements, laboratory chamber

studies, and field studies, can be used for structural assignments and benchmarking, probing physical properties, and elucidating molecular information about complex indoor surface processes.<sup>216</sup> Several recent efforts in the atmospheric chemistry community have focused on the synthesis of proposed oxidation products derived from isoprene,<sup>95, 217-220</sup> monoterpenes (e.g.  $\alpha$ - and  $\beta$ -pinene, carene, and limonene),<sup>221-226</sup> and  $\beta$ -caryophyllene,<sup>101, 227-230</sup> the most abundant sesquiterpene emitted into the atmosphere.<sup>229, 231-233</sup> Synthetic isotopic labeling strategies, namely those focused on site-specific deuterium and  $^{13}\text{C}$  labeling of biogenic VOCs, have also been developed.<sup>162, 215, 234-236</sup> These standards have been used to elucidate information on mechanistic pathways, identify and quantify the presence of molecular constituents in both laboratory and field samples, as well as determine atmospherically relevant physical properties. There exists a critical need for expanding the scope of such synthetic efforts in order to improve the number of precursor VOCs, oxidation products, and isotopologues available to the indoor air chemistry and physics community.

## **3.2 Molecular Orientation at the Squalene/Air Interface**

### **3.2.1 Introduction**

The presence of human occupants can significantly impact indoor air composition through breath and skin emissions.<sup>164, 237-239</sup> The C=C double bonds of unsaturated lipids in skin oil can react heterogeneously with ozone on various surfaces such as skin, hair, soiled clothing, and any other indoor surface that we have touched and on which we have left skin oil. These reactions lower the ozone concentrations in occupied indoor environments and generate a variety of (di)carbonyls, carboxyls, and hydroxycarbonyls, some of which may be respiratory or skin irritants depending on their volatility.<sup>164, 239</sup> Among the lipids comprising human skin oil, squalene is the

most ozone-reactive constituent,<sup>240-241</sup> with six double bonds, squalene contributes to about 50% of unsaturation in skin oil.<sup>242</sup> Numerous studies have experimentally characterized the products and investigated the kinetics of heterogeneous squalene ozonolysis.<sup>66, 73, 83, 190, 243</sup> Kinetic models have also been developed at different scales to address various aspects of the process.<sup>167, 189, 244</sup> However, the conformation and orientation of the topmost layer of squalene molecules, in the nanometer-thin interfacial region, have not been clearly described or studied. As a result, the molecular-level picture of the air/squalene interface, where the reaction first occurs when ozone impinges on the skin oil surface, remains enigmatic.

As explained in Section 3.1.1 *Molecular Orientation*, the polarity difference and dielectric profile across the interface, along the z-axis, between two bulk phases can drive interfacial molecules to adopt preferential orientations and tilt angles. At an air:skin oil interface, squalene molecules may adopt a non-uniform distribution of tilt angles. This orientational preference is an important factor in determining the reactivity of each of the six C=C double bond in squalene because it dictates the accessibility of C=C bonds to incoming ozone molecules. As a result, the reaction probability (due to different molecular overlap, i.e., reactive cross section) and non-reactive contributions to the ozonolysis kinetics (collision rates) may be strongly influenced by interfacial molecular orientation. As mentioned in Section 3.1.1 *Molecular Orientation*, previous studies have provided experimental evidence that the reactive uptake coefficients for the ozonolysis of olefins bound to silanized glass surfaces differs depending on whether the C=C double bond points towards the air or the glass side.<sup>26</sup> Moreover, the ozonolysis of closely spaced terminal C=C double bonds in self assembled monolayers has been reported to readily yield a dimeric carboxylic acid anhydride, highlighting the importance of local environment, orientations, and proximity.<sup>245</sup>

The polarization-resolved SFG signal is sensitive to the orientations of vibrational modes, which can help us deduce the orientation of the chemical bonds and even the entire molecule. Such an approach has seen many successful precedents in interfacial chemistry in various contexts, which provides a rich library aiding in spectral assignment and orientational analysis, especially in the C–H stretching region.<sup>107-111</sup>

For relatively large and complex molecules, however, it can be challenging to deduce orientational information solely from experimental data or even make robust spectral assignment in the congested C–H stretching region where normal modes overlap with each other and can be delocalized.<sup>186-187</sup> To aid with the spectral interpretation, MD simulations have been successfully employed to obtain atomistic information about conformations and orientations of interfacial molecules.<sup>121, 246-247</sup> Hall *et al.* have described an approach to analyzing the orientation of complex molecules like leucine, in which they simulated SFG spectra for the dominant conformers of leucine on surfaces and searched for the ratio of the conformers that generate the best matching spectrum to the experimental data.<sup>246</sup> Ho *et al.* have presented a similar analysis of  $\alpha$ -pinene on fused silica, in which they calculated SFG spectra for every possible molecular orientation to find the ensemble-averaged SFG spectrum that recapitulated the experimental spectrum.<sup>121</sup> In these two cases, the target molecules have relatively rigid structures, which means the number of dominant conformers is reasonable and such calculation is feasible. Unfortunately, this is not the case for squalene, which can adopt almost 125000 distinct conformers, based on the conformational flexibility of the main carbon chain dihedral angles alone. For even larger molecules such as lipids, peptides, and proteins, although there have been reports of peak assignments in the C–H stretching region, they are based on spectral fitting and previous common assignments of alkyl chains or



amino acids.<sup>248-250</sup> For proteins, motifs such as amide bonds that provide more information on the secondary structures are gaining more research interest.<sup>247, 251-255</sup>

In this section, we have collaborated with Dr. Michael von Domaros in Prof. Douglas Tobias's group at University of California, Irvine, on investigating the orientation of squalene molecules at surfaces. Dr. von Domaros complemented our experimental SFG data with electronic structure calculations and MD simulations (**Figure 3.1**). All the simulation work in this section is attributed to Dr. Michael von Domaros, Dr. Eva Perlt, and Prof. Douglas J. Tobias. Brief descriptions of the computational methods and results are provided so that the full picture can be better understood. More details can be found in the publication.<sup>256</sup>

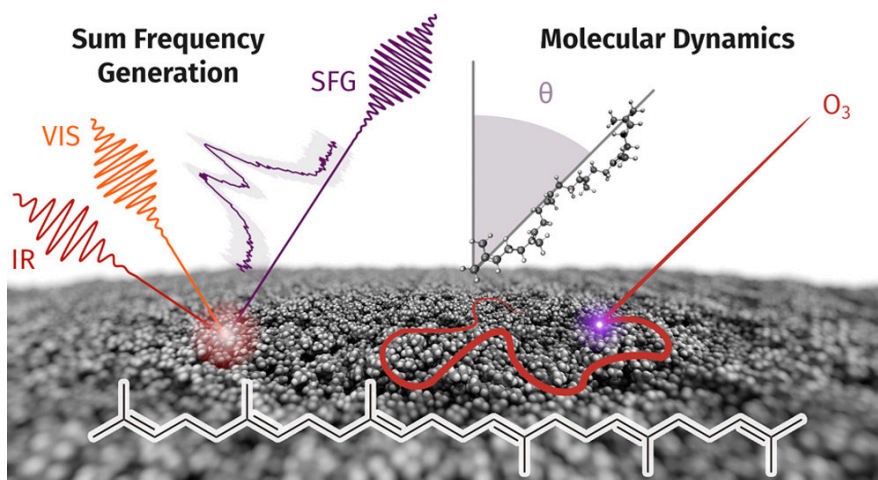


**Figure 3.1.** An illustration of the combined spectroscopic and atomistic modeling approaches to elucidate the conformational and orientational preferences of squalene at the air/oil interface and collisions with ozone.

### 3.2.2 Methods

**A. Sample Preparation and SFG Measurements.** Samples were prepared by dissolving squalene (Sigma-Aldrich, Part No. S3626, >98%, used as received) in deuterated chloroform,  $\text{CDCl}_3$  (Sigma-Aldrich, Part No. 151823, 99.8 atom % D), and spin-coating squalene at 3000 rpm onto a fused silica optical window substrate (ISP Optics, Part No. QI-W-25-3) that had been sonicated in

methanol (Fisher Scientific, Part No. A452-4, HPLC grade), rinsed with methanol and Millipore water alternately, and then plasma cleaned. The thickness of the spin-coated squalene film was characterized with 3D optical microscope (Bruker ContourGT). The coated sample window was clamped vertically on a translational stage. The Spectra-Physics Solstice SFG laser system and the data acquisition procedure used in the current study have been described in detail in previous work.<sup>112</sup> The incident IR beam and visible beam overlap spatially and temporally in an external geometry at the air/squalene interface. SFG spectra were taken with *ssp*, *ppp*, and *sps* polarization combinations. The ambient temperature and relative humidity in the laboratory were maintained at  $20 \pm 1$  °C and 30 – 50%.

**B. Spectral Fitting Procedure.** The spectra were fit using the equation below to disentangle all the vibrational modes.

$$I_{SFG} \propto |\chi^{(2)}|^2 = \left| \chi_{NR}^{(2)} + \sum_{\nu}^n \chi_{\nu}^{(2)} \right|^2,$$

where  $\chi^{(2)}$  is the second-order nonlinear susceptibility which consists of a nonresonant term  $\chi_{NR}^{(2)}$  and terms that resonant with surface vibrational modes  $\chi_{\nu}^{(2)}$ . The resonant terms can be expressed below.

$$\chi_{\nu}^{(2)} = \frac{a_{\nu} e^{i\theta_{\nu}}}{\omega_{\nu} - \omega - i\Gamma_{\nu}},$$

where  $a_{\nu}$ ,  $\theta_{\nu}$ ,  $\omega_{\nu}$ , and  $\Gamma_{\nu}$  are the amplitude, phase angle, frequency, and the peak width of the vibrational mode  $\nu$ , respectively. In this work, phase angles are fixed at 0° or 180° allowing vibrational modes to constructively or destructively interfere with each other. The numerators are thus simplified to  $\pm a_{\nu}$  based on the relative phases of the vibrational modes. The resonant terms  $\chi_{\nu}^{(2)}$  include two O–H stretching modes fixed at 3400  $\text{cm}^{-1}$  and 3200  $\text{cm}^{-1}$  for convenience,

representing the more loosely and the more tightly hydrogen-bonded network, respectively, and five C–H stretching modes, methyl Fermi resonance ( $r_{FR}$ ), methyl symmetric ( $r^+$ ) and asymmetric stretch ( $r^-$ ), and methylene symmetric ( $d^+$ ) and asymmetric stretch ( $d^-$ ). The asymmetric stretches are fixed to be out of phase with symmetric stretches and Fermi resonances. The two O–H stretching modes are out of phase with each other.

**C. MD Simulations.** Dr. von Domaros performed all-atom MD simulations to characterize the structure of the air/squalene interface. The system consists of 343 squalene molecules set up in a slab geometry and oriented so that the surface normal points along the  $z$ -axis of the coordinate system (**Figure 3.2**). The center of mass of the slab lies at  $z = 0$ .

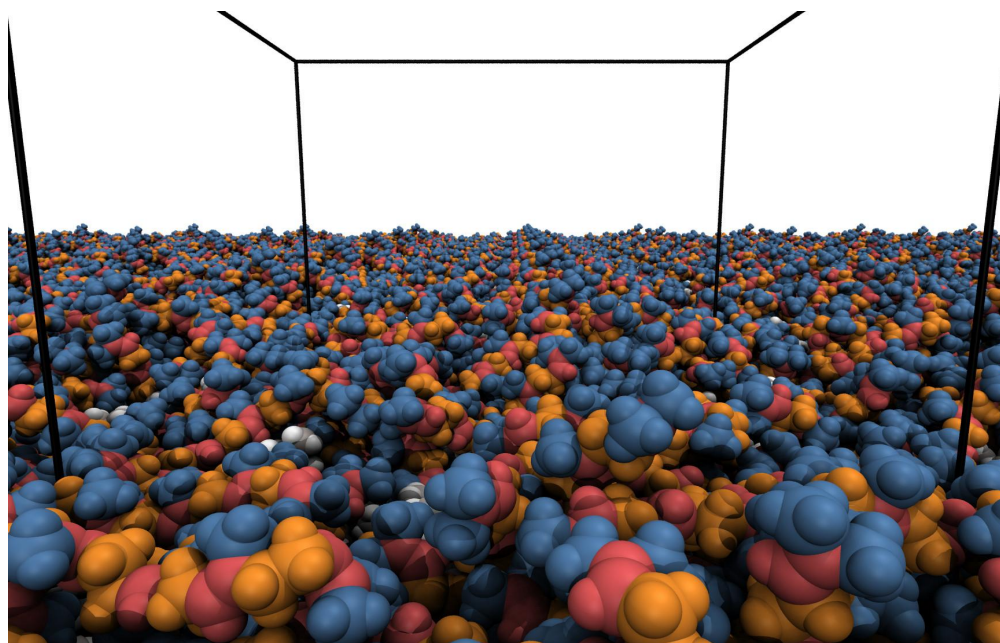


**Figure 3.2.** Snapshot with view on the squalene/vacuum interface. The black lines show the simulation cell. The system is 3D periodic. The color code for the interfacial atoms is as follows: blue  $\rightarrow$  methyl groups; orange  $\rightarrow$  methylene groups; red  $\rightarrow$  vinylic C–H groups.

675 short (2 ns) simulations in the microcanonical ensemble were also performed, in which thermalized (298.15 K) ozone molecules—initially placed randomly at some distance from the slab—impinge on the squalene surface. Ozone interactions were described as reported by Vácha *et al.*<sup>257</sup> The outcomes of these impinging-molecule simulations were used to estimate surface and bulk accommodation coefficients, as well as ozone–double-bond collision rates. A full description of this procedure can be found in previous work.<sup>189, 258-259</sup>

Further simulation details, including the initialization and equilibration protocol, have been described previously.<sup>189, 244</sup> The present study differs only in the configuration of the individual squalene molecules. Previous work was based on a squalene isomer with two *cis*-configured double bonds (IUPAC name prefix 6Z,10Z,14E,18E), taken from the crystal structure of *bacteriorhodopsin*.<sup>260</sup> Here, we investigate the all-*trans* isomer (6E,10E,14E,18E), which was also used in the experiments. We consistently exploit the symmetry of the simulation setup and report all quantities as averages over both sides of the slab.

**D. Electronic Structure Calculations.** Gas-phase geometry optimizations and vibrational frequency analyses were carried out for one of the dominant squalene conformers (all-*anti*). All calculations were performed at the density functional level of theory (DFT), with the Tao-Perdew-Staroverov-Scuseria (TPSS) meta-hybrid functional (TPSSh),<sup>261</sup> a def2-TZVP basis set,<sup>262</sup> and fourth generation dispersion correction (D4).<sup>263</sup> The calculations were carried out with the Turbomole v7.5<sup>264-265</sup> software package.

### 3.2.3 Results and Discussion

**A. SFG spectra of the surface of a squalene film.** Spin-coated squalene films on fused silica consist of large patches of droplets that are a few micrometers thick and small densely packed droplets that are tens to hundreds of nanometers thick, revealed by 3D optical microscope (**Figure 3.3**). A representative *ssp*-polarized spectrum of the surface of a squalene film in the C–H and O–H stretching regions ( $2600 - 3800 \text{ cm}^{-1}$ ) is shown in **Figure 3.3**. Replicates of spectra with *ssp*, *ppp*, and *sps* polarization combinations are shown in **Figure 3.4**. These spectra were collected from different samples prepared on different days and the spectral features are generally consistent. Because the spectrum is normalized to the reference nonresonant signal from gold and the signal from it is relatively low towards the edges of the spectrum due to weak IR power there, the signal-to-noise ratio is relatively low on both ends.

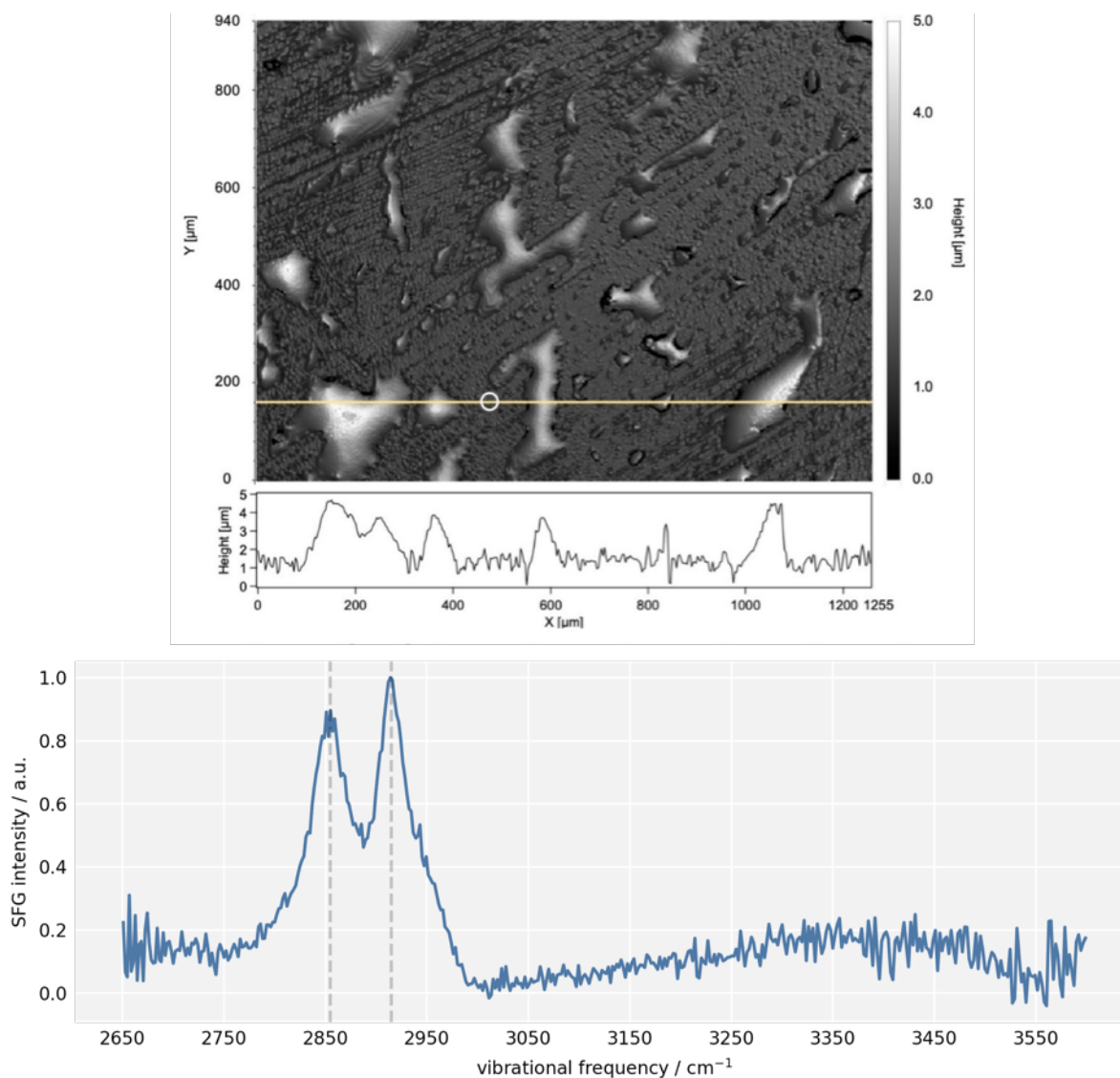


**Figure 3.3.** Top: A representative 3D optical image of a spin-coated squalene film on fused silica, with the height profile shown at  $Y = 180 \mu\text{m}$  (yellow line). “Height 0” was set to the lowest height on the image. Laser spot size used in the SFG experiments indicated by a white circle. Bottom: A representative ssp-polarized vibrational SFG spectrum of the surface of a squalene film.

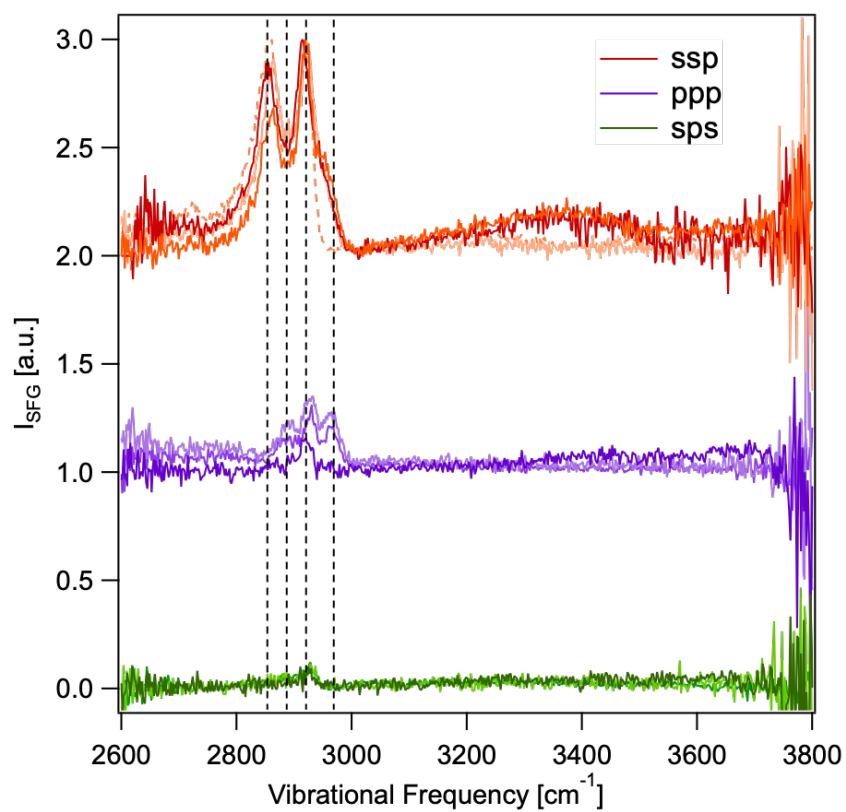


**Figure 3.4.** Replicates of ssp-, ppp-, and sps-polarized SFG spectra of the surface of squalene films on fused silica.

Considering the molecular structure of squalene, the most striking feature of the spectrum shown in **Figure 3.3** is the lack of a distinguishable signal around  $3050\text{ cm}^{-1}$ , which would be expected for the vinylic ( $=\text{C}-\text{H}$ ) modes, despite the fact that squalene contains six vinylic  $\text{C}-\text{H}$  bonds.<sup>26, 109, 158-159</sup> The other polarization combinations we used did not show signal intensity in that frequency region, either (**Figure 3.4**). This finding indicates that the vinylic  $\text{C}-\text{H}$  bonds are oriented such that their transition dipole moments sum to zero, which would be expected for all *trans*-configured modes, or modes that are symmetrically distributed in and/or normal to the  $x$ - $y$  plane of the interface. Next, the  $\text{O}-\text{H}$  stretching region appears to contain a weak broad band, indicating the presence of some water molecules at the squalene surface at ambient relative

humidity. The  $3400\text{ cm}^{-1}$  center frequency of this broad band matches that of bulk liquid water, indicating perhaps the presence of a loosely hydrogen-bonded network of water molecules.<sup>266</sup>

The  $sp^3$ -hybridized C–H stretching region (below  $3000\text{ cm}^{-1}$ ) in the *ssp*-polarized spectra is dominated by two main peaks at around  $2855\text{ cm}^{-1}$  and  $2915\text{ cm}^{-1}$ , which are usually assigned as methylene symmetric and asymmetric stretches, respectively.<sup>107, 109, 267</sup> A shoulder appears near  $2965\text{ cm}^{-1}$ , which is normally attributed to methyl asymmetric stretches<sup>268-269</sup> or methyl Fermi resonances.<sup>270</sup> One of the *ssp*-polarized spectra is an outlier without the shoulder band and is notated with dashed lines. The considerable SFG intensity at  $2900\text{ cm}^{-1}$  indicates the presence of additional modes, given the spectral resolution of our instrument ( $\sim 8\text{ cm}^{-1}$  near  $2900\text{ cm}^{-1}$ ). Indeed, all-trans-configured n-octadecyl silane show no signal intensity in this frequency region.<sup>271</sup> The *ppp*-polarized spectra generally exhibit three peaks at around  $2965\text{ cm}^{-1}$ ,  $2930\text{ cm}^{-1}$ , and  $2900\text{ cm}^{-1}$  and the *sps*-polarized spectra only contain a small bump at around  $2930\text{ cm}^{-1}$ . The broad O–H stretching band only appears to be significant in some *ssp*-polarized spectra.

## B. Spectral Fitting Attempts

While the frequencies of the two dominant peaks and the shoulder in the *ssp*-polarized spectra are consistent with reported IR spectra of squalene in literature,<sup>272-273</sup> the published spectral assignments have only been approximate in the C-H stretching region. This lack of information is not surprising, given the complexity of squalene's molecular structure. The best spectral fitting results are shown in **Figure 3.5** and summarized in **Table 3.1**.



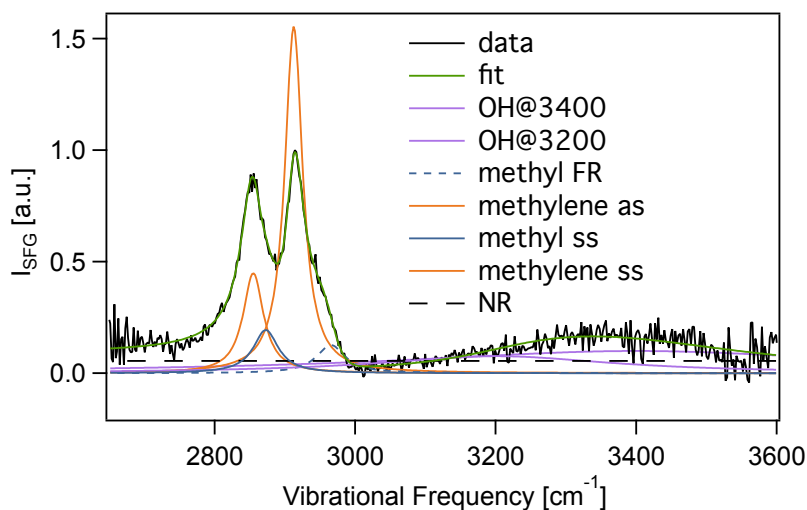


**Figure 3.5.** Spectral fitting of a representative ssp-polarized SFG spectrum of an air/squalene interface.

**Table 3.4.** Spectral fitting results of the representative ssp-polarized SFG spectrum of an air/squalene interface.

Assignment	$d^+$	$r^+$	$d^-$	$r^-$	$r_{FR}$	OH at 3200 $\text{cm}^{-1}$	OH at 3400 $\text{cm}^{-1}$	NR
<b>Frequency</b>	2855(3)	2873(7)	2912.5(9)	--	2965(3)	3200	3400	--
<b>Amplitude</b>	12(9)	$1(1) \times 10^1$	-19(1)	--	9(2)	$-6(1) \times 10^1$	$1.3(3) \times 10^2$	0.24(3)
<b>Width</b>	18(4)	$2(1) \times 10^1$	15.4(8)	--	25(4)	$2.0(3) \times 10^2$	$4.0(4) \times 10^2$	--

As discussed in the Section 3.2.1 Introduction, we caution that, for a large and flexible molecule like squalene, it is not accurate to assign individual peaks to single normal modes. The normal modes are scattered over the C–H stretching spectral range. Therefore, we present our spectral fitting attempts with common peak assignments here but avoid interpretation of the fitting results. The fitting results only poorly recapitulated the structural information obtained from the atomistic simulations, as described next.

**C. Squalene Tends to Orient Along Surface Normal with Terminal Double Bonds Nearest Surface.** Figure 3.6 shows position-dependent correlation functions,  $g(z)$ , for selected parts of a squalene molecule. These functions give the probability of finding atoms belonging to the chosen moiety at a position  $z$ , relative to the respective bulk phase probability. While the atomic mass distribution of the system is relatively featureless (sigmoidal shape; top panel, solid line), the center of mass distribution shows a layered interfacial structure that spans about two nanometers (top panel, dashed line). Furthermore, individual atoms, in particular those forming the symmetry-equivalent groups of double bonds, are non-uniformly distributed across the squalene/air interface (bottom panel). Above 30 Å, it is most likely to find a terminal squalene double bond. The probabilities to find the interjacent and innermost bonds peak at 28 Å and 24 Å respectively. It is evident that the squalene molecules have orientational preferences in the interface (a tendency to be aligned with the surface normal).

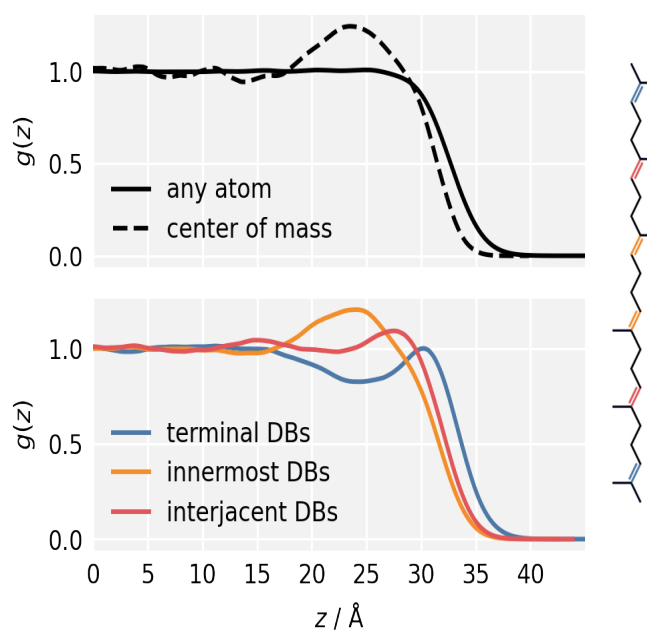


**Figure 3.6.** Position-dependent correlation functions,  $g(z)$ , for various parts of a squalene molecule.

**D. Four in Five Squalene Molecules Have at Most One *Gauche* Defect.** Conformational flexibility can lead to differences in molecular shape, symmetry, and thus reactivity, as discussed in the Introduction. The largest contribution to conformational flexibility in squalene molecules comes from rotations around the methylene bridge carbon-carbon bonds. The primary conformation of these dihedral angles is *anti* (**Figure 3.7**, left panel). About 45% of all squalene molecules have all-*anti* methylene bridges and ~37% have only one *gauche* defect (center panel). Only in rare cases are all methylene bridges *gauche*. There is no significant variability between populations in the interface and in the bulk. In the right panel of **Figure 3.7**, we illustrate the general shape of squalene molecules by showing one randomly selected snapshot for each possible number of *gauche* defects per molecule. The two dominant conformers with zero or one defects are primarily chain-like.

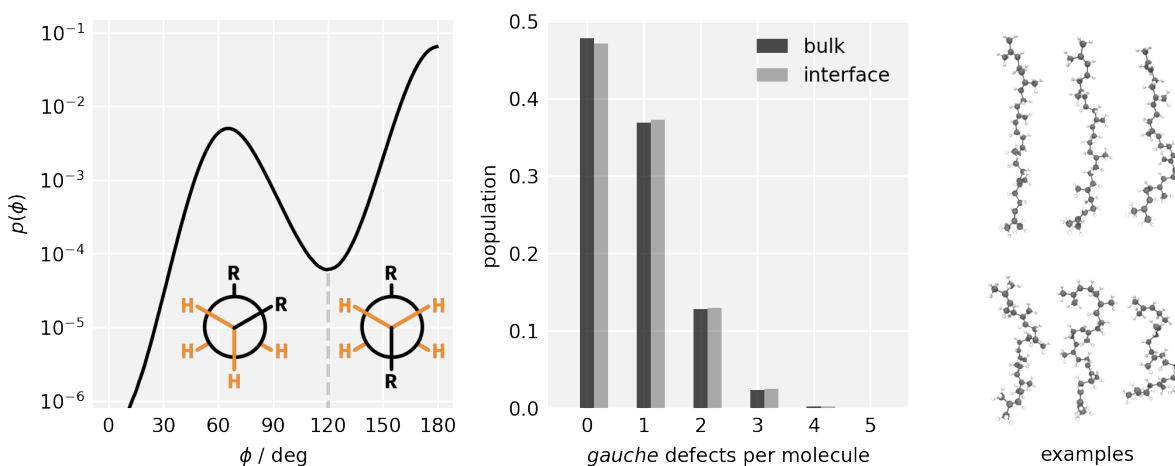


**Figure 3.7.** *Left:* Distribution of the methylene bridge dihedral angles. An angular cutoff of  $120^\circ$  was used to separate the two states. *Center:* Populations of squalene conformers with zero to five *gauche* defects, both in the bulk and in the interface (empirically defined through the molecular center of mass position,  $z_{\text{com}} \geq 15 \text{ \AA}$ , cf. **Figure 3.6**). *Right:* In row-major order, snapshots of randomly selected squalene conformers with zero to five *gauche* defects.

In terms of SFG signal, the all-*anti* conformers of squalene have all the methylene groups in adjacent pairs with opposite alignments and thus possess local inversion centers. Therefore,

despite being the largest population, the methylene groups in all-*anti* conformers should not contribute significantly to SFG signal, compared to the conformers with more distorted symmetry introduced by one or more *gauche* defects.<sup>274-275</sup> This result indicates that the spectral assignment of the 2855 cm<sup>-1</sup> mode to a CH<sub>2</sub> symmetric stretch that we based on assigned SFG spectra of common aliphatic compounds is unlikely to be correct. To pursue this issue further, we proceeded towards analyzing the molecular alignment of the methyl, methylene, and vinyl dipole moments,  $\mu$ , with respect to the surface normal (*z*-axis).

### **E. Methyl Groups Prefer Alignment Along Surface Normal, Other Groups Much Less So.**

We first note that each of groups we studied is charge neutral in the CHARMM force field. In the top row of **Figure 3.8**, we show joint probability densities between the group center of mass position  $z_{\text{group}}$  and the group orientation, measured in terms of  $\cos\theta = \mu_z/|\mu|$ , where  $\mu_z$  is the component of the group dipole vector  $\mu$  along the surface normal. To emphasize orientational preferences, we show the differences relative to the bulk distribution in the bottom row. Within the interface, there is a clear tendency for methyl group dipoles to be preferentially oriented along the surface normal, and more specifically, pointing upwards (note the predominance of the color blue in **Figure 3.2**). The same trend, although attenuated, can be seen for methylene groups.

Interfacial vinylic C–H groups prefer to be either aligned or anti-aligned with the surface normal. The molecular origin of this dichotomy lies in the molecular structure of the squalene molecules and the strong tendency of methyl groups to be aligned with the surface normal. Consider the terminal methyl groups of a squalene molecule, which have higher than average concentrations in the interface (**Figure 3.6**). Because of the rigidity of double bonds, methyl groups act as an anchor for the C–H group connected to them. Depending on which of the two methyl

groups is aligned with the surface normal, the corresponding C–H bond tends to have either a positive or negative  $z$ -contribution. Methylene groups are less restricted by these effects because of the possibility of rotation around the bond linking the  $sp^2$ - $sp^3$ -hybridized carbon atoms.

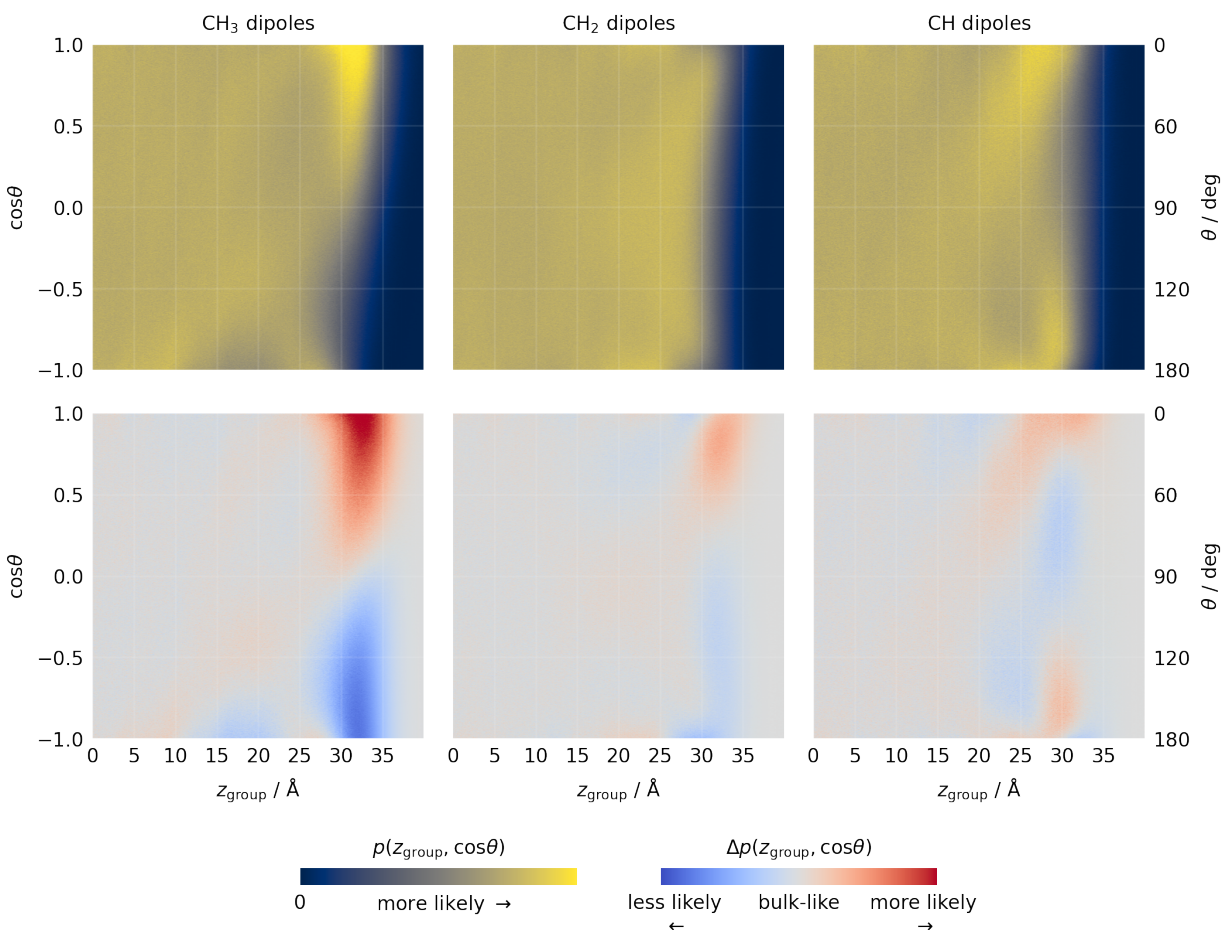


**Figure 3.8.** *Top row:* Joint probability densities between group center of mass position and group dipole moment orientation,  $p(z_{\text{group}}, \cos\theta)$ , for methyl, methylene, and vinylic C–H groups. Values of  $\cos\theta = 1$  correspond to alignment with the surface normal. *Bottom row:* Probability density differences relative to the bulk density.

While the methylene groups located at the interface point their transition dipole moments up along the surface normal, the vast majority of them are *trans*-configured and thus SFG inactive, based on the results from the previous section. Methyl groups, on the other hand, are expected to contribute more to *ssp*-polarized SFG intensity relative to methylene groups. Finally, the analysis

presented here indicated why no vinylic =C–H stretches are observed in the SFG spectrum: while their C–H bonds point along the surface normal, a comparable number of them point their C–H bonds down into the bulk to largely cancel the overall second-order contribution.

**F. Vibrational Frequency Analysis.** To aid with the vibrational mode assignment problem discussed in Section 3.2.3B, we computed the gas-phase IR and Raman spectra of a single squalene molecule in one of the dominant all-*anti* conformations at the density functional level of theory (**Figure 3.9**).

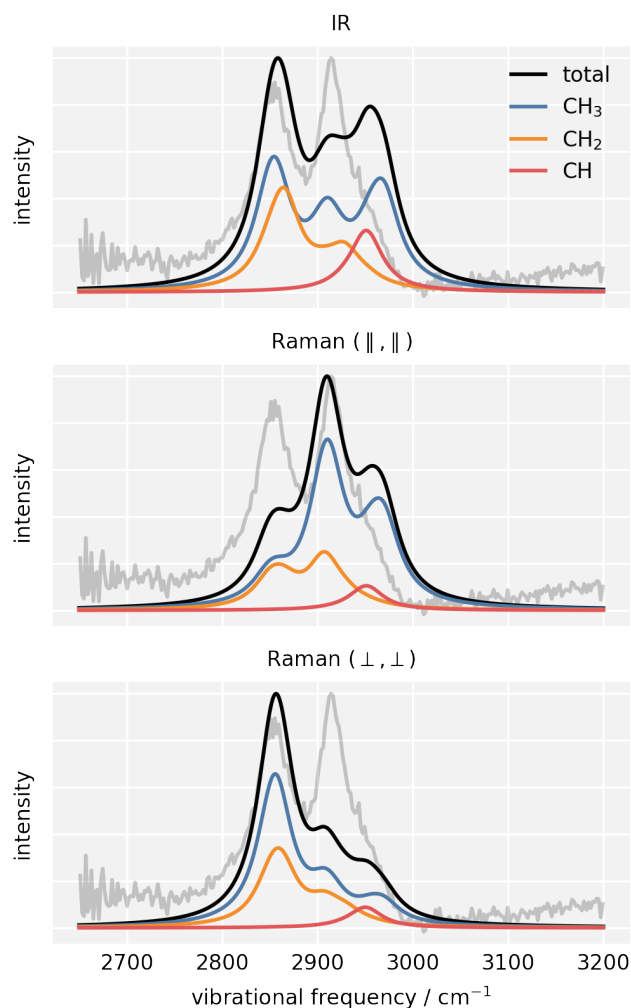


**Figure 3.9.** Computed gas-phase IR and Raman spectra, as well as group contributions. The measured SFG spectrum has been overlaid (shaded curve) to guide the eye. Computed line spectra have been convoluted with Lorentzian functions with a full width at half maximum of  $20\text{ cm}^{-1}$ . Frequencies were scaled by a constant to match the experimental peaks. See Supporting Information section SI.3 for details on the identification of group contributions. For Raman spectra, the polarization of the incident and scattered beams is given in parentheses.

In a similar combined experimental/DFT study, only minor conformational effects on the vibrational frequencies have been observed.<sup>272</sup> Through a normal mode analysis, we identified group contributions to the overall IR intensity/Raman scattering cross section in the C–H stretching region. Visual inspection of the normal modes revealed a strong non-local character of most motions. The spectra have been frequency scaled to be aligned with the measured SFG spectrum.

The remaining minor discrepancies in the peak locations can be attributed to the neglect of interfacial solvation effects, computational setup,<sup>188</sup> and/or the neglect of Fermi resonances in the harmonic approximation. The comparison to the results reported in previous work is presented in

**Figure 3.10.**

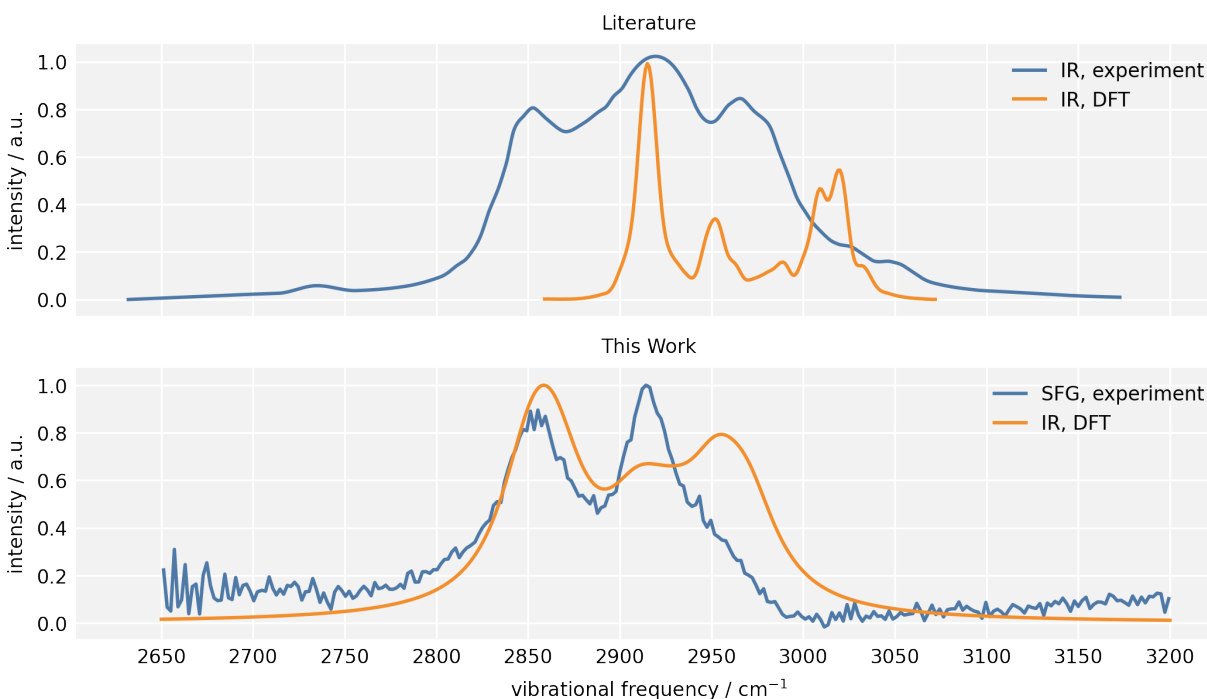


**Figure 3.10.** *Top panel:* Experimental liquid-phase IR spectrum and computed gas-phase IR spectrum (DFT/B3LYP/cc-pVTZ) for squalene. The data was extracted through digitization of Figure 3 in ref. 272. *Bottom panel:* Experimental SFG spectrum and computed gas-phase IR spectrum (DFT-D4/TPSSh/def2-TZVP) for squalene obtained in this work. The spectra in this work have been convoluted with broader Lorentzian functions.

Our results support the notion that it is inaccurate to assign each individual peak to an isolated methyl or methylene group. Methyl group normal modes span the complete C–H stretching region (2800–3000 cm<sup>-1</sup>), methylene group signals peak in the lower two thirds of the frequency range, and vinylic C–H groups in the upper third. These findings are consistent with those in ref. 272. Note that the experimental IR spectrum reported in Laan et al.<sup>272</sup> shows only a



weak signal in the typical vinylic C-H stretching region above  $3000\text{ cm}^{-1}$ , even though there are six such bonds in squalene. While unanticipated, this lack of a substantial IR response above  $3000\text{ cm}^{-1}$  is consistent with the computed vibrational responses, as well as the SFG spectrum. Also note that the presence of vinylic C-H peak in the IR and Raman spectra does not contradict its absence in the SFG spectra since SFG, as a second-order process, samples the orientational ensemble average of vibrational modes.

To more reliably calculate the contribution of each mode to individual peaks and match the experimental spectrum, one would need to simulate SFG spectra for all the conformations and orientations of squalene molecules on the surface and take the ensemble average, as described in the Introduction. For a large and flexible molecule like squalene, the large conformational space that would need to be surveyed makes the computation prohibitively expensive. This approach is therefore beyond the scope of this work. Another method of disentangling the normal modes is to selectively deuterate certain positions of the squalene molecule, which requires extensive synthetic work but can potentially provide great insights.<sup>161, 187, 276</sup> Finally, heterodyning the SFG response from squalene against the non-resonant response from a nonlinear optical material with a known phase, such as  $\alpha$ -quartz, would provide the phase information needed to determine which modes are in and out of phase of one another,<sup>277</sup> which would further aid in the spectroscopic assignments.

**3.2.4 Implications for Ozonolysis Rates.** To assess the impact of the orientational and conformational preferences of squalene on an important indoor air reaction — its ozonolysis — we computed position-dependent ozone–double-bond collision rates,  $c_{\text{O}_3\text{-DB}}$ . These rates are related to reaction rates,  $r_{\text{O}_3\text{-DB}}$ , through the reaction probability,  $\gamma_{\text{O}_3\text{-DB}}$ , with  $r_{\text{O}_3\text{-DB}} = \gamma_{\text{O}_3\text{-DB}} \cdot c_{\text{O}_3\text{-DB}}$ . Collision rates are thus an important measure for the non-reactive aspect of the squalene

ozonolysis kinetics. The position-dependent rates have been estimated from the impinging molecule simulations, which (due to their large number) provide ample ozone–double-bond collisions, both in the interface and the bulk. Collision rates were estimated by counting the number of ozone–double-bond collisions in bins along  $z$ , and dividing by the residence time within the bins.<sup>189, 258-259</sup> This normalization condition ensures that collision rates are uniform in the bulk and decay to zero in the gas phase, despite the inhomogeneous sampling of different regions of the interface due to the nature of the impinging-molecule simulations. Results have been split up into contributions from the different types of symmetry-equivalent double bonds present in the system and are shown in **Figure 3.11**. While ozone does not show any preference to collide with a particular class of double bonds in the bulk, collisions with terminal double bonds are more frequent than others in the interface. This behavior can be well understood with the orientational and conformational preferences discussed above.

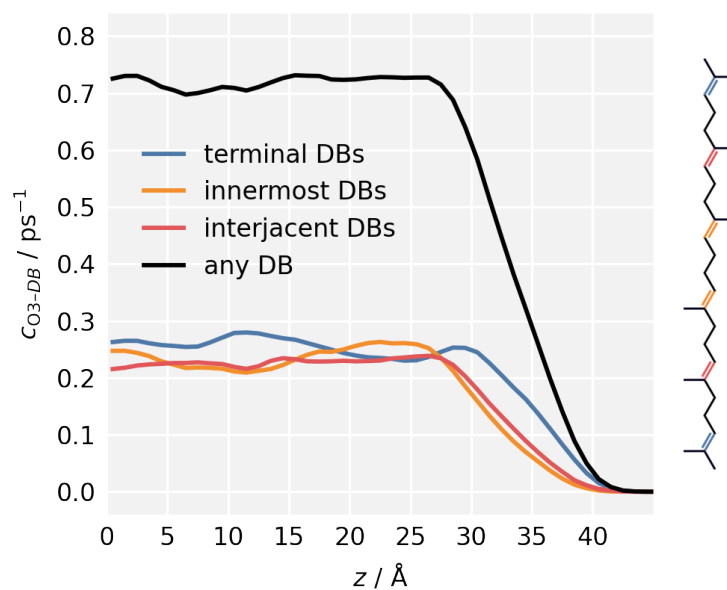


**Figure 3.11.** Position-dependent ozone–double-bond collision rates,  $c_{O3-DB}$ .

### 3.2.5 Conclusions.

With 50 vibrational normal modes in the C–H stretching region and close to 125000 possible conformations stemming solely from the dihedral flexibility of the main carbon chain, squalene is a spectroscopically complex molecule. We have begun to disentangle this complexity with MD simulations that revealed strong orientational/conformational preferences of interfacial squalene molecules. Our approach indicated that the vinylic =C–H oscillators point up and down in the interfacial region, largely resulting in an unanticipated cancellation of the SFG signal intensity at the expected oscillator frequency of  $\sim 3050\text{ cm}^{-1}$ . Vibrational peak assignments derived from common, long alkyl chain-containing molecules, which would attribute the  $2855\text{ cm}^{-1}$  and  $2915\text{ cm}^{-1}$  peaks to methylene stretches, were found to be at variance with the largely *anti*-configured  $\text{CH}_2$  groups dominating the interfacial squalene molecules in the MD simulations. Instead, the spectral features at these frequencies are likely to be largely due to the methyl groups that are oriented along the surface normal, resulting in different concentrations of the various types of its double bonds and thus different reactivities.

Another key finding of this study is that the concentrations of various types of squalene double bonds is predicted to differ in the interfacial region compared to the bulk. This prediction has direct implications for the reactivity of squalene with ozone and other indoor air oxidants. Collision rates between ozone and terminal double bonds were estimated to be higher in the interface when compared to those with interior bonds. This outcome warrants a more detailed investigation in kinetic models describing this important aspect of indoor air chemistry, as it would point towards a reaction mechanism in which the differing accessibility of each of the six C=C double bond to ozone would determine which oxygenated gas phase product would be formed. As relative humidity values indoors can vary considerably during the day, the role of adsorbed water, clearly observed in the SFG spectrum shown in **Figure 3.3 and 3.4**, should also be investigated,

especially given recent results indicating an intricate connection between viscosity and water/squalene interactions in reverse micelles.<sup>278</sup>

### **3.3 Preliminary Investigations on Ozonolysis of Squalene and Skin Oil**

With the flow setup and the capabilities of the laser system described in Section 2.5.2 in Chapter 2, we have started to investigate the ozonolysis process of squalene and skin oil. Some preliminary results are shown in this section and my fellow graduate student, Jana Butman, will continue the research and explore other characterization methods such as optical microscope and contact angle goniometry.

The SFG response of squalene, spin coated on a fused silica window, before and after 40 minutes of ozone flow was recorded (**Figure 3.12**). The spectral lineshape was largely retained but the signal intensity decreased significantly. Our current hypothesis is that, since the ozonolysis products of squalene are mostly volatile, the total amount of material left on the window decreased, resulting in lower signal. More experimental evidence is needed to characterize the chemical composition and molecular orientation of the material after ozonolysis.

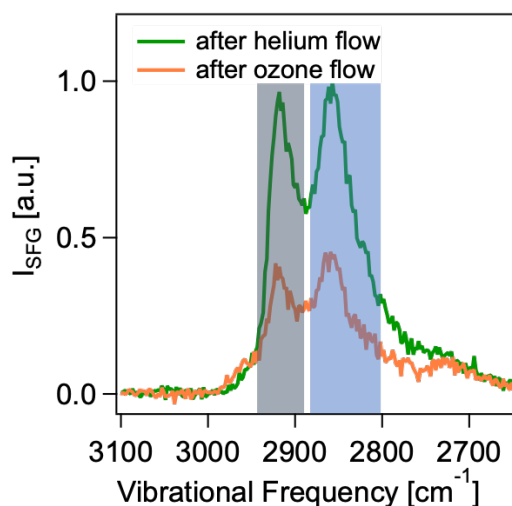


**Figure 3.12.** Representative ssp-polarized SFG spectra of squalene before (in green) and after (in orange) ozone flow. The helium flow was employed to adjust the RH. During the experiment, the RH was maintained at 40%. The ozone concentration was at 30 – 50 ppb. The shaded area indicates the wavenumber ranges of the integration of the two peak areas, which are used in kinetic analysis.

The kinetics of the ozonolysis was preliminarily investigated by tracking the signal decrease over time. The peak areas of the two peaks (shaded in blue and gray, respectively, in **Figure 3.12**) were integrated and plotted as a function of time (**Figure 3.13**). The peak areas of both peaks seemed to reach a stable level after about 5 minutes. However, the peak area of the lower-frequency peak resumed decreasing at about 30 minutes, exhibiting a two-step process. Furthermore, both peaks did not start decreasing until after 2 – 3 minutes. Since the total volume of the tubing and the sample flow cell is less than 30 cm<sup>3</sup> and the total flow rate is 2 standard liter per minute, ozone should arrive at the window within one second. Replicates are needed to confirm the reproducibility of the phenomenon and more investigation is needed to understand why the signal did not start decreasing immediately at time zero.

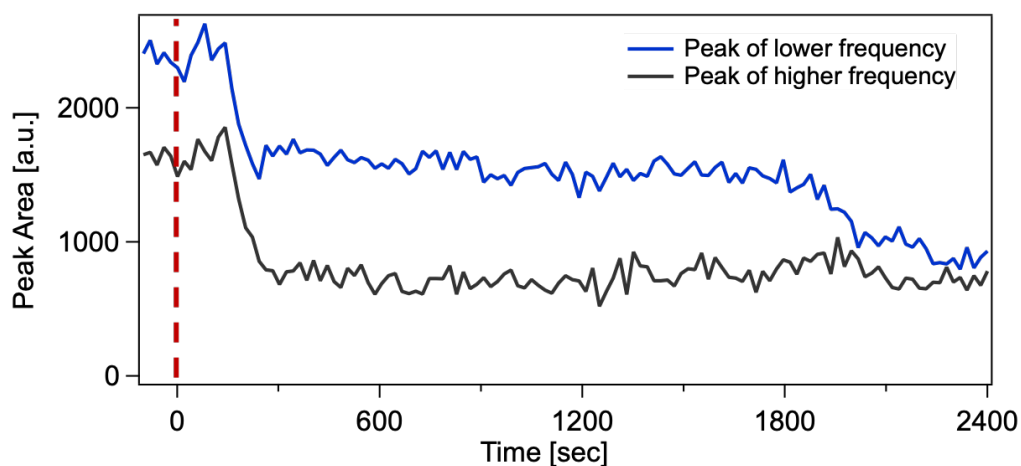


**Figure 3.13.** The peak areas of the two peaks in the ssp-polarized SFG spectra of squalene during ozonolysis over a time period of 40 min. The time zero is marked with a red dashed line.

Similar experiments were conducted for skin oil, collected as fingerprints on fused silica windows, under dry ( $RH < 5\%$ ) and wet ( $RH \sim 50\%$ ) conditions with ozone concentrations much higher than typical in indoor environments. Even though skin oil is a complex mixture of organic compounds, the SFG spectra are surprisingly consistent from day to day and the peaks appear well-defined and narrow. Upon ozonolysis, signal decrease was observed with the spectral features retained, similar to the results from squalene ozonolysis. Since the signal intensity almost remained the same after 10 minutes of helium flow under both dry and wet conditions, the signal decrease was not from the material being “blown away” by gas flows. Again, more experiments are needed to obtain more information about the process.

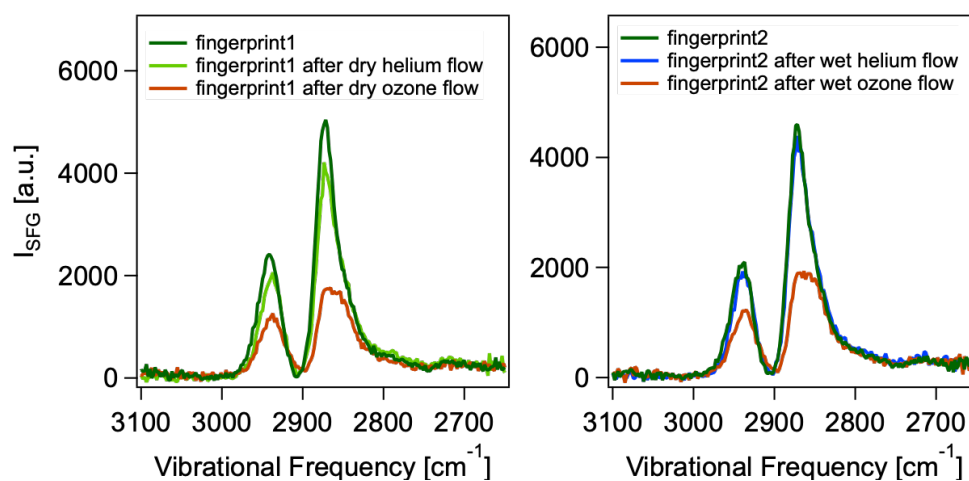


**Figure 3.14.** Representative ssp-polarized SFG spectra of two skin oil samples, collected on two different days, before and after 20 minutes of ozone flow. The helium flow was employed to adjust the RH. On the left, the RH was maintained below 5% and the ozone concentration was 1 – 1.2 ppm. On the right, the RH was maintained around 50% and the ozone concentration was about 0.5 ppm.

### 3.4 Home-Derived Indoor Molecular, Nano-, and Microlayers – Stay-at-HomeChem Campaign

Going beyond the idealized laboratory-controlled studies presented in the previous sections, one can passively collect matter suspended in the air from real indoor environments to perform analysis on. Depending on the sampling duration, which may range from under an hour to several days or weeks, surface spectroscopic techniques with the appropriate sensitivities may identify surface bound species under ambient conditions.

In 2020, the COVID-19 outbreak in the US led to stay-at-home orders in all but five U.S. states. Under the stay-at-home orders, Americans were spending the vast majority of their time at home, and, in many cases, with family members who would otherwise live elsewhere. What are the impacts of the more substantial human presence in indoor environments on indoor air? How do human activities under the stay-at-home orders influence the physical and chemical processes

of the built environment, compared to the “business as usual” condition? To address these questions, our group initiated the “Stay-at-HomeChem” campaign, which aimed at collecting indoor air samples during the stay-at-home orders, analyzing the samples, and comparing them to the “business as usual” time once the stay-at-home orders are lifted. In the campaign planning stage, I participated in discussions on protocols about sample handling, timelines, and activity logging, and coordinated home information gathering. Currently, we are coordinating post-campaign sample exchange, measurements, and information sharing. With the country open, plans are to carry out counterfactual campaign and run the same experiments for the same duration with participants at school/work.

### 3.4.1 Techniques to be Used for Sample Analysis

We first summarized a list of available techniques with information about their throughput, type of information to be obtained, substrate requirement, and whether sample can be reused after measurements (**Table 3.2**), since the information is important for deciding the number of samples to be collected and the types of substrates.

**Table 3.5.** Summary of available methods to be used for analyzing indoor surface samples.

<b>Method</b>	<b># of samples/hour*</b>	<b>Information</b>	<b>Substrate requirement</b>	<b>Can samples be reused after measurement?</b>
<b>DART-MS</b>	High	Chemical composition	N.A.	No
<b>APPI-ESI-MS</b>	TBA	Chemical composition	N.A.	No
<b>Optical microscopy</b>	High	Shape, size, morphology	Reflective/transparent	Yes
<b>UV-Vis</b>	High	Color, scattering as proxy for amount adsorbed	Reflective/transparent	Yes
<b>FTIR</b>	High	Chemical bonds	IR transparent	Yes



<b>ATR, PMIRAS</b>	Medium	Chemical bonds	N.A.	In part
<b>Raman</b>	Low	Chemical bonds, pH	N.A.	Yes
<b>Contact angle goniometry</b>	Medium	Hydrophobicity	Flat	In part
<b>XRF</b>	Medium to High	Elemental composition	N.A.	Yes
<b>AFM-IR</b>	Low	Chemical bonds, spatially resolved	Flat	Yes
<b>SFG</b>	Low	Chemical bonds	Reflective/transparent	Yes

\*high=>10, medium=~1, low=<<1 hr<sup>-1</sup>

### 3.4.2 Information about Participants' Home Environments

A Google survey was delivered to 24 participants to collect important information about their home environments. The list of questions on the survey includes:

- 1) What is your residence ID (RID) number?
- 2) What is the time zone of your home?
- 3) What is the closest description of your home type?
  - a. Single family detached house
  - b. Apartment/Condo with a separate kitchen
  - c. Apartment/Condo with an open/half open kitchen
  - d. Studio with a separate kitchen
  - e. Studio with an open/half open kitchen
  - f. Other
- 4) How many people live in your home?
- 5) How many pets are there in your home?
- 6) Do you have air conditioning (AC) in your home? (Check all that apply.)
  - a. Yes, I have central AC.
  - b – e. Yes, I have an AC in my bedroom/living room/dining room/home office.
  - f. No, I don't have AC in any room in my home.
  - g. Other
- 7) What best describes the location of your home?
  - a. Dense urban downtown
  - b. Suburban
  - c. College town
  - d. Countryside
  - e. Other
- 8) Rate how much traffic is around your home. (Range 1 – 5)
- 9) Rate how "green" the outdoor environment is around your home. (Range 1 – 5)

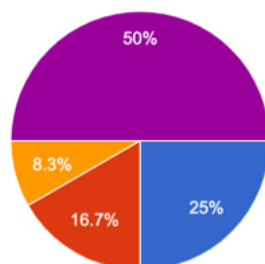
- 10) Where in your house will you set up sample collections? (Check all that apply.)
- a. Kitchen
  - b. Bedroom
  - c. Living room
  - d. Bathroom
  - e. Home Office
  - f. Other

Then, depending on the type of rooms the participant indicated, more specific information about the room (windows/screens/appliance/fan/radiator/others) was collected.

A variety of home environments were sampled in this campaign (see **Figure 3.15** for responses to selected questions). In terms of room choice, since we are interested in how increased home occupancy during the stay-at-home orders change indoor chemistry, the rooms to sample should at least be the one of those that are most occupied during the day under the current stay-at-home orders. As an example, kitchens and perhaps the associated dining/living room area are likely to be occupied a lot more and witness more human activities than before, so it will be interesting to sample that area. According to the responses from 24 participants, we collected samples in 22 kitchens, 9 bedrooms, 7 living rooms, 4 home offices, 1 bathroom, and 1 four-season room.

What is the time zone of your home?

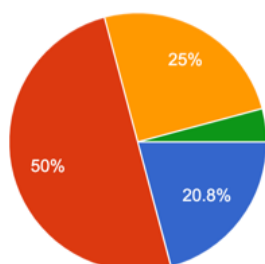
24 responses



- Eastern Daylight Time (EDT) (GMT-4)
- Central Daylight Time (CDT) (GMT-5)
- Mountain Daylight Time (MDT) (GMT-6)
- Mountain Standard Time (MST) (GMT-7) (certain regions in Arizona)
- Pacific Daylight Time (PDT) (GMT-7)
- Alaska Daylight Time (AKDT) (GMT-8)
- Hawaii-Aleutian Standard Time (HST) (GMT-10)

What best describes the location of your home?

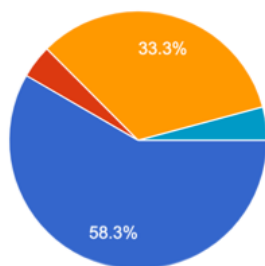
24 responses



- Dense urban downtown
- Suburban
- College town
- Countryside

What is the closest description of your home type?

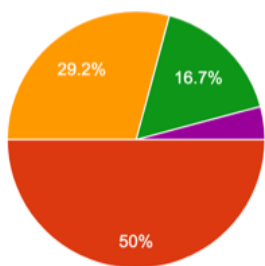
24 responses



- Single family detached house
- Apartment/Condo with separate kitchen
- Apartment/Condo with open/half open kitchen
- Studio with separate kitchen
- Studio with open/half open kitchen
- 2 bedroom apartment with open kitchen and living room

How many people live in your home?

24 responses



- 1
- 2
- 3
- 4
- 5
- 6 or more

**Figure 3.15.** Participants responses to some survey questions regarding their home environments.

### 3.4.3 Timeline of Experiments for Each Room

Each participant performed Experiment A and B and then chose between C and D.

#### **Experiment A: 3-Week sampling to collect large amounts of materials**

Each participant places three samples next to one another into the room(s) of their choice and keeps them there for the entire duration of the campaign, three weeks. The samples are labeled as A1, A2, and A3.

#### **Experiment B: “Accumulative” sampling to observe material building up over each week**

On day 1 of each of the three weeks, each participant stores one field blank (labeled as FB1, FB2, and FB3) and places seven samples next to one another into the room(s) of their choice. The samples are labeled as B1–7 in week 1, B8–14 in week 2, and B15–21 in week 3. One sample per day is stored on successive days as indicated below. As a result, for example, sample B1 collects for the first 24 hours of week 1, while sample B7 collects for all seven days of week 1.

Note: underscore marks the duration of the sampler in action. The sample is stored at the end of the underscore line.

**Week 1**

Sample

B1  
B2  
B3  
B4  
B5  
B6  
B7  
FB1

Day

1      2      3      4      5      6      7

**Week 2**

Sample

B8  
B9  
B10  
B11  
B12  
B13  
B14  
FB2

Day

8      9      10      11      12      13      14

**Week 3**

Sample

B15  
B16  
B17  
B18  
B19  
B20  
B21  
FB3

Day

15      16      17      18      19      20      21

**Experiment C: 24-Hour sampling to observe daily variations**

Samples on Day 1/8/15 are not needed as they are the same as samples B1/8/15.

**Week 1**

Sample

		<u>C1</u>						
			<u>C2</u>					
				<u>C3</u>				
					<u>C4</u>			
						<u>C5</u>		
							<u>C6</u>	
<b>Day</b>	<b>1</b>	<b>2</b>	<b>3</b>	<b>4</b>	<b>5</b>	<b>6</b>	<b>7</b>	

**Week 2**

Sample

		<u>C7</u>						
			<u>C8</u>					
				<u>C9</u>				
					<u>C10</u>			
						<u>C11</u>		
							<u>C12</u>	
<b>Day</b>	<b>8</b>	<b>9</b>	<b>10</b>	<b>11</b>	<b>12</b>	<b>13</b>	<b>14</b>	

**Week 3**

Sample

		<u>C13</u>						
			<u>C14</u>					
				<u>C15</u>				
					<u>C16</u>			
						<u>C17</u>		
							<u>C18</u>	
<b>Day</b>	<b>15</b>	<b>16</b>	<b>17</b>	<b>18</b>	<b>19</b>	<b>20</b>	<b>21</b>	

### Experiment D: 3-Hour sampling to observe variations within a given day

#### Day X

Sample	<u>D1</u>	<u>D2</u>	<u>D3</u>	<u>D4</u>	<u>D5</u>	<u>D6</u>	<u>D7</u>	<u>D8</u>
	<u>FB4</u>							<u>FB5</u>
Time	00:00	03:00	06:00	09:00	12:00	15:00	18:00	21:00

#### 3.4.4 Sample Collection and Storage

The entire procedure of sample collection and storage was discussed in detail and communicated to the participants through videos. Samples were collected on microscope glass slides, both sides of which were wiped with methanol on folded lens papers. The glass slides were clamped by metal clips on both ends and placed vertically at sample collection locations. A cover slip was cleaned and clamped on the edge of one side of each glass slide so that the area under the cover slip could serve as an internal reference without any contamination. The metal clips helped prevent the glass slide from tilting over and served as a handle for holding and moving the glass slides.

After the collection, each individual glass slide was stored in a glass jar or a falcon tube and labeled with codes that specified the participant ID, experiment number, room type, and date and time.

#### 3.4.5 Field Diary/Data Logging

The emphasis of this campaign is less on scripted activities of the participants, but more on appropriately detailed documentation of spontaneous and regular activities by each participant through activity logging in the form of a field intensive diary. Each participant was shared with a Google sheet to keep an electronic diary of daily data. The sheet indicated the participant to enter daily information about the date, sample placement, sample storage, cooking events, vacuuming events, cleaning events, average total household occupancy, human occupancy and duration in the room sampled, duration of window being open in the room sampled, duration of fan/exhaust on in the room sampled, and duration of AC on in the room sampled. Participants were also encouraged to record the weather data every day, including temperature, humidity, rainfall level, air quality index, and pollen level. These data can be potentially useful for understanding correlations between environmental factors and sample properties or any anomalies.



## **CHAPTER 4**

### **Vibrational Sum Frequency Scattering (SFS) Setup for Suspended Aerosols**

## 4.1 Introduction

As demonstrated in previous chapters, SFG spectroscopy is advantageous in studying interfacial processes in the atmospheric and indoor environments for its intrinsic surface selectivity, chemical-bond specificity, molecular orientation sensitivity, and applicability under ambient conditions. However, conventional SFG spectroscopy is only applicable for flat surfaces. In the work presented in Chapter 2, optically flat surfaces such as fused silica windows were used to model mineral dust as seeds for aerosols. In the work presented in Chapter 3, aerosols particles collected from the field were deposited on filters, pressed on flat optical windows, and then probed by SFG spectroscopy. In a recent publication from our group, we studied the behaviors of a suite of surface active  $\beta$ -caryophyllene oxidation products on aqueous aerosols by spreading them on a flat aqueous surface.<sup>100</sup> Besides atmospheric chemistry research, in indoor environments, the surface properties and evolution of aerosols, mostly from human sources, are of great research interest, especially in the current context of COVID-19.<sup>39, 166, 279-280</sup> It has not been well established whether the curvature of aerosol droplets or particles will affect the surface properties, compared to those of flat surfaces, because of the lack of surface selective techniques that can be directly employed for suspended aerosols. It would therefore significantly benefit the atmospheric and indoor surface chemistry communities to expand the capabilities of vibrational SFG spectroscopy to sum frequency scattering (SFS) of suspensions of submicron aerosols.

Second harmonic scattering (SHS) was developed earlier and has been more widely applied in different systems.<sup>281-291</sup> Rao and coworkers first reported an SHS setup on submicron aerosols in the gas phase and studied their surface properties.<sup>292-294</sup> As for SFS from suspensions of spherical particles, the theoretical basis has been described in detail<sup>288, 295</sup> and successful SFS experiments on suspensions of organic-coated particles or emulsions of oil droplets in liquids have

been demonstrated.<sup>295-298</sup> The first and, so far, the only SFS setup that can probe gas-phase aerosol particles was also reported by Rao and coworkers and was an electronic SFS system instead of a vibrational one.<sup>299</sup> This chapter will explain the practical considerations of building a vibrational SFS setup for gas-phase aerosols, show the experimental setup in the current stage, and present preliminary transmission SFG results obtained from the setup.

## 4.2 Experimental Considerations

*Particle Density.* As Rao and coworkers stated, the low number density of gas-phase aerosol particles presents as a major challenge for nonlinear scattering signal detection.<sup>292</sup> Our high power TOPAS SFG system allows for significant signal detection (120 counts/second) from a monolayer of  $\alpha$ -pinene ( $2 \times 10^9$  molecules in the focal spot) over a 300-msec acquisition. We adopted a near-collinear geometry for the IR and visible beam to optimize the focal volume ( $10^{-2} \text{ mm}^3$ ). Despite the low particle density in aerosol suspensions ( $10^7$  particles  $\text{cm}^{-3}$  at the highest), we expect to observe 20 SFG counts per second from an  $\alpha$ -pinene aerosol (100 nm diameter) in air over a 1-sec acquisition time.

*Detection Angle.* The scattering angle is known to be dependent on particle size. SHS studies have demonstrated that, in general, the scattering angles of larger particles of about 1  $\mu\text{m}$  in diameter are around 0 – 20 degrees and those of smaller particles below 100 nm in diameter are around 60 – 90 degrees.<sup>283, 285-287, 289</sup> However, Rao and coworkers adopted a forward geometry in their SHS<sup>292-293</sup> and electronic SFS setup<sup>299</sup> and detected scattering signal from gas-phase aerosols at around 0 degree. Roke *et al.* collected the highest signal from particles around 600 – 800 nm in diameter at a scattering angle of about 30 degrees<sup>295</sup> and later her group adopted a 60-degree

scattering angle for droplets with an average diameter of  $\sim 200$  nm.<sup>296-297</sup> In this work, since the aerosol droplets will have a nominal mode diameter of about 100 nm, the detection angles of 60 and 90 degrees will be picked first for aerosol scattering experiments. The 0- and 90-degree angles were also picked for transmission SFG detection from quartz and reflection SFG detection from gold, respectively, in the optical alignment stage. Increasing the size of the collecting lens can also increase the amount of light collected, but it requires the optics downstream, up to the focusing lens, to have the same size to prevent any loss of signal.

*Sample Container.* Rao and coworkers directed the aerosol droplets through a sealed chamber to the exhaust. The beam passed through the chamber perpendicularly, with the focusing lens and the recollimating lens placed inside the chamber.<sup>292-293</sup> In their initial setup, an additional pump was used to further evacuate the aerosols in the chamber.<sup>292</sup> However, since the optics are directly exposed to aerosols, this setup is vulnerable to potential damaging to the optics over time. In this work, we choose to contain the aerosols in a tube that is largely transparent to incident and output light. A cylindrical tube is used so that the detection angle can be varied. Although the tube itself can be easily cleaned or replaced, aerosols may partition to the wall during the experiment, which needs to be carefully examined.

### **4.3 Experimental Setup**

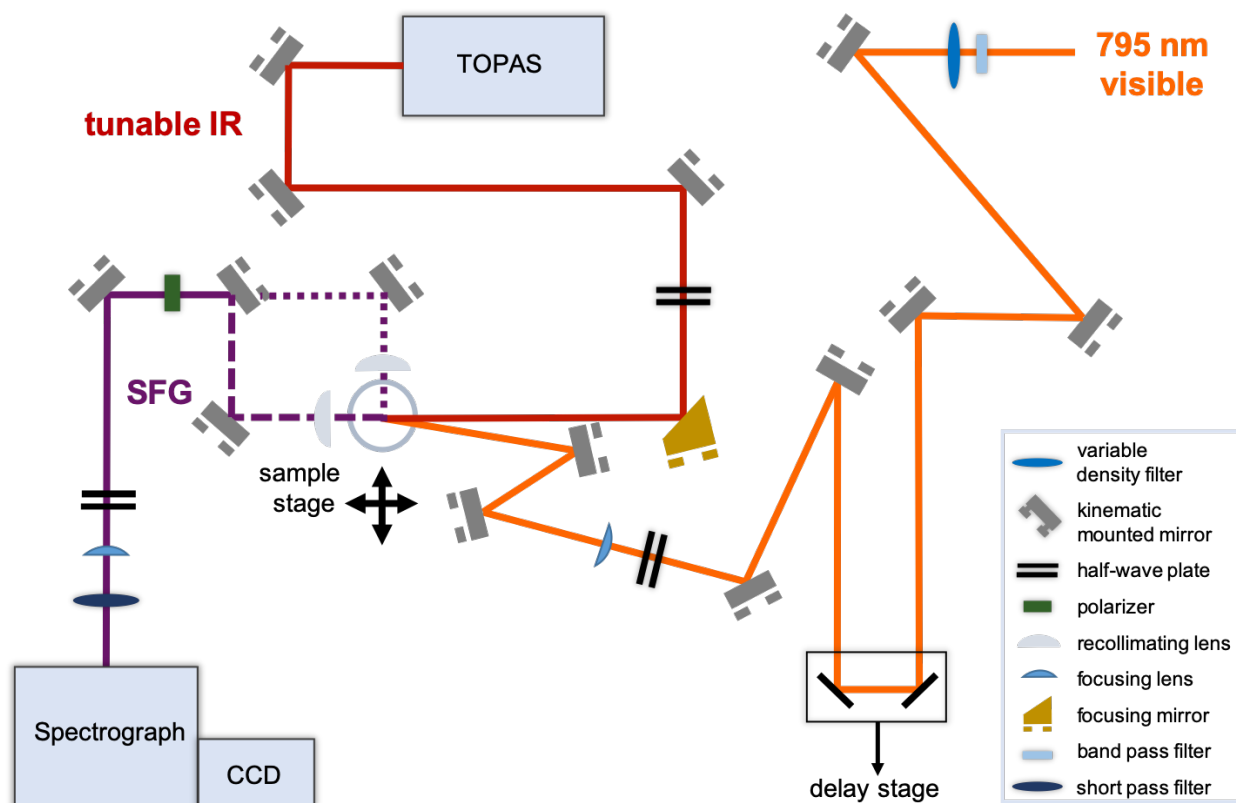


**Figure 4.1.** Schematic of the sum frequency scattering setup with the femtosecond, kHz Spectra-Physics Solstice /TOPAS laser system. Only the detection angles of 0 and 90 degrees are shown. Please refer to the text for details about the design and the part numbers.

The SFS setup shared the Spectra-Physics Solstice /TOPAS laser system and the detector system with our SFG setup described in previous work.<sup>112</sup> Three flip mirror mounts (Newport, 9891) are used to direct the beams to switch between the two setups. In brief, the Solstice system is a Ti:sapphire laser system that produces 795-nm pulses with 3 mJ pulse energy, 1 kHz repetition rate, and 120 femtosecond pulse duration. The beam passes through a 90/10 beam splitter (CVI, BS1-800-90-1012-45P), after which 90% of the beam pumps a tunable optical parametric amplifier (TOPAS, Light Conversion) to generate a tunable broadband IR beam. The IR beam then passes through a longpass IR filter and is focused onto the sample stage with a parabolic focusing mirror (Thorlabs, MPD169-M01). The remaining 10% of the beam passes through a narrow bandpass

filter (Andover Corporation, 795.0 nm wavelength, 1.0 nm bandwidth), a variable density filter (Thorlabs, NDC-50C-4), a delay stage, and a focusing lens (Thorlabs, LA1484-B) with 300.0 mm focal length. A focusing lens with long focal length for the visible beam is intentionally selected so that the beam gradually comes to a focus and thus would not be sensitive to small changes in alignment. The incident beam geometry in the paper of Roke and coworkers was adopted.<sup>295</sup> The visible beam and the IR beam are placed close to a collinear geometry (separated by a small angle  $\sim 10$  degrees) so as to maximize the focal volume in the aerosols.

The sample stage can translate in the x, y, and z directions. A custom-made fused quartz (GE Type 214 quartz) cylindrical tube (15 mm ID, 18 mm OD, and 64 mm long), with  $\frac{1}{4}$  inch OD segments attached to both ends as tube fittings, is clamped vertically on the stage for the aerosols to pass through. The IR transmittance of the Type 214 quartz is above 90% for the C–H and O–H stretching region (2700 – 3800 nm). The aerosols will be generated with a constant output atomizer (TSI 3076), fed with a stream of helium gas (Ultra-High Purity, 99.999%). For optical alignment, a reference can be clamped at the center position of the tube and a tube, made of the same material and of the same size but without the narrow tube fitting segments, can be slid on around the reference and adjusted with the translational stage to ensure that the beam passes through the tube at a normal angle.

The sum frequency scattering light will be collected with a recollimating lens (Thorlabs, LA1422-A) with relatively short focal length in order to maximize the light collection. Two detection angles, 90 and 180 degrees, are selected (indicated with different dashed lines in **Figure 4.1**). The beam passes through a polarizer (Thorlabs, GT10-A) for output polarization selection and a half-wave plate (Karl Lambrecht Corporation, MWPA2-12-400-700) so that the polarization is optimized for the signal collection at the spectrograph. The output beam then passes

through a focusing lens and a notch filter (Kaiser Optical Systems, Inc., holographic notch-plus filter, 61193622) before entering the spectrograph (Acton SP-2558 Imaging Spectrograph and Monochromator) coupled with a CCD camera (Roper Scientific,  $1340 \times 100$  pixels). Gold mirrors (Edmund Optics, 45606) are used for the input IR and visible beams and silver mirrors (Thorlabs, PF10-03-P01) are used for the output SFG beam.

#### 4.4 Preliminary Results and Future Plans

The optical system was aligned with a gold window in the reflection geometry with a detection angle of 90 degrees, and with a 1-mm thick quartz in the transmission geometry with a detection angle of 0 degree. The normalized spectra are shown in **Figure 4.2**. With gold in the reflection geometry, the peak SFG signal was about 45,000 counts. With the quartz in the transmission geometry, the highest counts were about 5000. Note that the axes of the quartz sample were unknown, so the relative signal intensities with different polarization combinations cannot be interpreted at this point.

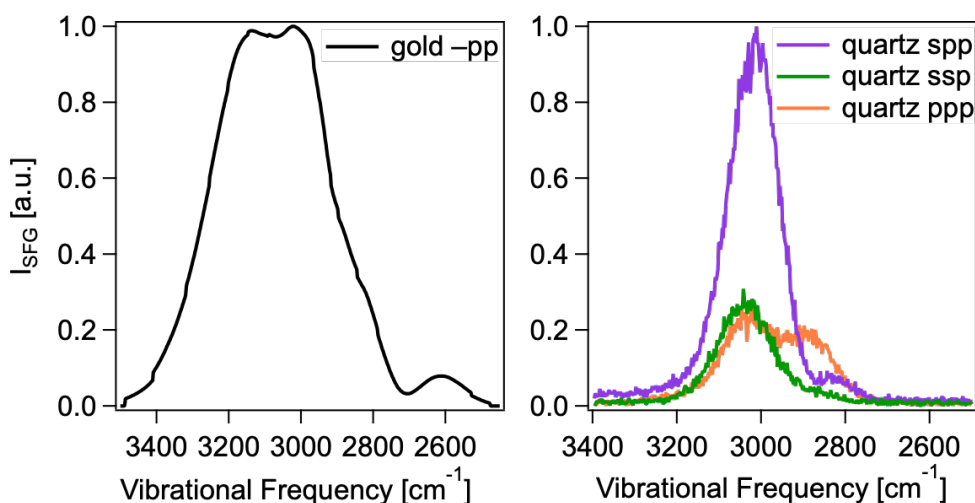


**Figure 4.2.** The reflection SFG spectrum of a gold window (normalized to the maximum signal) and the transmission SFG spectra of a 1-mm thick piece of quartz (normalized to the maximum signal in the *spp*-polarized spectrum). The SFG signal of the gold did not pass through a polarizer

but the incident visible and IR beams were both  $p$  polarized. The quartz spectra were taken with three polarization combinations.

The next step would be to find SFS signal from suspensions of aerosols.  $\alpha$ -Pinene and organic molecule coated polystyrene latex beads in water can be considered as potential candidates for aerosol samples. As a contingency plan, the optical setup with the best detection angle can be first optimized with a well-studied system, such as an emulsion of surfactant-stabilized oil droplets in water.



## References

1. Seinfeld, J. H.; Pandis, S. N., *Atmospheric Chemistry and Physics: From Air Pollution to Climate Change*; John Wiley & Sons, 2016.
2. Schauer, J. J.; Rogge, W. F.; Hildemann, L. M.; Mazurek, M. A.; Cass, G. R.; Simoneit, B. R. T., Source Apportionment of Airborne Particulate Matter Using Organic Compounds as Tracers. *Atmospheric Environment* **1996**, *30*, 3837-3855.
3. Kanakidou, M., et al., Organic Aerosol and Global Climate Modelling: A Review. *Atmos. Chem. Phys.* **2005**, *5*, 1053-1123.
4. Viana, M., et al., Source Apportionment of Particulate Matter in Europe: A Review of Methods and Results. *Journal of Aerosol Science* **2008**, *39*, 827-849.
5. Atkinson, R., Atmospheric Chemistry of Vocs and Nox. *Atmospheric Environment* **2000**, *34*, 2063-2101.
6. Hallquist, M., et al., The Formation, Properties and Impact of Secondary Organic Aerosol: Current and Emerging Issues. *Atmos. Chem. Phys.* **2009**, *9*, 5155-5236.
7. Charlson, R. J.; Schwartz, S. E.; Hales, J. M.; Cess, R. D.; Coakley, J. A.; Hansen, J. E.; Hofmann, D. J., Climate Forcing by Anthropogenic Aerosols. *Science* **1992**, *255*, 423-430.
8. Haywood, J.; Boucher, O., Estimates of the Direct and Indirect Radiative Forcing Due to Tropospheric Aerosols: A Review. *Reviews of Geophysics* **2000**, *38*, 513-543.
9. Novakov, T.; Penner, J. E., Large Contribution of Organic Aerosols to Cloud-Condensation-Nuclei Concentrations. *Nature* **1993**, *365*, 823.
10. Novakov, T.; Corrigan, C. E., Cloud Condensation Nucleus Activity of the Organic Component of Biomass Smoke Particles. *Geophysical Research Letters* **1996**, *23*, 2141-2144.
11. Lohmann, U.; Feichter, J., Global Indirect Aerosol Effects: A Review. *Atmospheric Chemistry and Physics* **2005**, *5*, 715-737.
12. Andreae, M. O.; Crutzen, P. J., Atmospheric Aerosols: Biogeochemical Sources and Role in Atmospheric Chemistry. *Science* **1997**, *276*, 1052-1058.
13. Kolb, C. E.; Worsnop, D. R., Chemistry and Composition of Atmospheric Aerosol Particles. *Annual Review of Physical Chemistry* **2012**, *63*, 471-491.

14. Shrivastava, M., et al., Recent Advances in Understanding Secondary Organic Aerosol: Implications for Global Climate Forcing. *Reviews of Geophysics* **2017**, *55*, 509-559.
15. Pachauri, R. K.; Allen, M. R.; Barros, V. R.; Broome, J.; Cramer, W.; Christ, R.; Church, J. A.; Clarke, L.; Dahe, Q.; Dasgupta, P., *Climate Change 2014: Synthesis Report. Contribution of Working Groups I, II and III to the Fifth Assessment Report of the Intergovernmental Panel on Climate Change*; IPCC, 2014.
16. Pöschl, U., et al., Rainforest Aerosols as Biogenic Nuclei of Clouds and Precipitation in the Amazon. *Science* **2010**, *329*, 1513-1516.
17. Martin, S. T., et al., Sources and Properties of Amazonian Aerosol Particles. *Reviews of Geophysics* **2010**, *48*.
18. Kroll, J. H.; Seinfeld, J. H., Chemistry of Secondary Organic Aerosol: Formation and Evolution of Low-Volatility Organics in the Atmosphere. *Atmospheric Environment* **2008**, *42*, 3593-3624.
19. Ebben, C. J., et al., Organic Constituents on the Surfaces of Aerosol Particles from Southern Finland, Amazonia, and California Studied by Vibrational Sum Frequency Generation. *The Journal of Physical Chemistry A* **2012**, *116*, 8271-8290.
20. Guenther, A.; Jiang, X.; Heald, C.; Sakulyanontvittaya, T.; Duhl, T.; Emmons, L.; Wang, X., The Model of Emissions of Gases and Aerosols from Nature Version 2.1 (Megan2. 1): An Extended and Updated Framework for Modeling Biogenic Emissions. **2012**.
21. O'Dowd, C. D.; Aalto, P.; Hmeri, K.; Kulmala, M.; Hoffmann, T., Atmospheric Particles from Organic Vapours. *Nature* **2002**, *416*, 497.
22. Claeys, M., et al., Terpenylic Acid and Related Compounds from the Oxidation of  $\alpha$ -Pinene: Implications for New Particle Formation and Growth above Forests. *Environmental Science & Technology* **2009**, *43*, 6976-6982.
23. Zhang, X.; McVay, R. C.; Huang, D. D.; Dalleska, N. F.; Aumont, B.; Flagan, R. C.; Seinfeld, J. H., Formation and Evolution of Molecular Products in  $\alpha$ -Pinene Secondary Organic Aerosol. *Proceedings of the National Academy of Sciences* **2015**, *112*, 14168-14173.
24. Pöschl, U.; Rudich, Y.; Ammann, M., Kinetic Model Framework for Aerosol and Cloud Surface Chemistry and Gas-Particle Interactions—Part 1: General Equations, Parameters, and Terminology. *Atmospheric Chemistry and Physics* **2007**, *7*, 5989-6023.

25. Voges, A. B.; Stokes, G. Y.; Gibbs-Davis, J. M.; Lettan, R. B.; Bertin, P. A.; Pike, R. C.; Nguyen, S. T.; Scheidt, K. A.; Geiger, F. M., Insights into Heterogeneous Atmospheric Oxidation Chemistry: Development of a Tailor-Made Synthetic Model for Studying Tropospheric Surface Chemistry. *The Journal of Physical Chemistry C* **2007**, *111*, 1567-1578.
26. Stokes, G. Y.; Chen, E. H.; Buchbinder, A. M.; Paxton, W. F.; Keeley, A.; Geiger, F. M., Atmospheric Heterogeneous Stereochemistry. *Journal of the American Chemical Society* **2009**, *131*, 13733-13737.
27. Jimenez, J. L., et al., Evolution of Organic Aerosols in the Atmosphere. *Science* **2009**, *326*, 1525-1529.
28. Klepeis, N. E.; Nelson, W. C.; Ott, W. R.; Robinson, J. P.; Tsang, A. M.; Switzer, P.; Behar, J. V.; Hern, S. C.; Engelmann, W. H., The National Human Activity Pattern Survey (Nhaps): A Resource for Assessing Exposure to Environmental Pollutants. *J. Expo. Anal. Environ. Epidemiol.* **2001**, *11*, 231-53.
29. Manuja, A.; Ritchie, J.; Buch, K.; Wu, Y.; Eichler, C. M. A.; Little, J. C.; Marr, L. C., Total Surface Area in Indoor Environments. *Environ. Sci. Process Impacts* **2019**, *21*, 1384-1392.
30. Bouhamra, W. S.; Elkilani, A. S., Investigation and Modeling of Surface Sorption/Desorption Behavior of Volatile Organic Compounds for Indoor Air Quality Analysis. *Environmental Technology* **1999**, *20*, 531-545.
31. Bouhamra, W.; Elkilani, A., Development of a Model for the Estimation of Indoor Volatile Organic Compounds Concentration Based on Experimental Sorption Parameters. *Environmental Science & Technology* **1999**, *33*, 2100-2105.
32. Elkilani, A.; Bouhamra, W.; Crittenden, B. D., An Indoor Air Quality Model That Includes the Sorption of Vocs on Fabrics. *Process Safety and Environmental Protection* **2001**, *79*, 233-243.
33. Mucha, M.; Frigato, T.; Levering, L. M.; Allen, H. C.; Tobias, D. J.; Dang, L. X.; Jungwirth, P., Unified Molecular Picture of the Surfaces of Aqueous Acid, Base, and Salt Solutions. *J. Phys. Chem. B.* **2005**, *109*, 7617-7623.
34. Shen, Y. R.; Ostroverkhov, V., Sum-Frequency Vibrational Spectroscopy on Water Interfaces: Polar Orientation of Water Molecules at Interfaces. *Chemical Reviews* **2006**, *106*, 1140-1154.

35. Ervens, B.; Sorooshian, A.; Lim, Y. B.; Turpin, B. J., Key Parameters Controlling Oh-Initiated Formation of Secondary Organic Aerosol in the Aqueous Phase (Aqsoa). *Journal of Geophysical Research: Atmospheres* **2014**, *119*, 3997-4016.
36. Marshall, F. H.; Berkemeier, T.; Shiraiwa, M.; Nandy, L.; Ohm, P. B.; Dutcher, C. S.; Reid, J. P., Influence of Particle Viscosity on Mass Transfer and Heterogeneous Ozonolysis Kinetics in Aqueous–Sucrose–Maleic Acid Aerosol. *Physical Chemistry Chemical Physics* **2018**, *20*, 15560-15573.
37. Marshall, F. H.; Miles, R. E. H.; Song, Y.-C.; Ohm, P. B.; Power, R. M.; Reid, J. P.; Dutcher, C. S., Diffusion and Reactivity in Ultraviscous Aerosol and the Correlation with Particle Viscosity. *Chemical Science* **2016**, *7*, 1298-1308.
38. Renbaum-Wolff, L.; Grayson, J. W.; Bateman, A. P.; Kuwata, M.; Sellier, M.; Murray, B. J.; Shilling, J. E.; Martin, S. T.; Bertram, A. K., Viscosity of  $\alpha$ -Pinene Secondary Organic Material and Implications for Particle Growth and Reactivity. *Proceedings of the National Academy of Sciences* **2013**, *110*, 8014–8019.
39. Ault, A. P., et al., Indoor Surface Chemistry: Developing a Molecular Picture of Reactions on Indoor Interfaces. *Chem* **2020**.
40. Rubasinghege, G.; Grassian, V., Role(S) of Adsorbed Water in the Surface Chemistry of Environmental Interfaces. *Chem. Comm.* **2013**, *49*, 3071-94.
41. Or, V. W.; Alves, M. R.; Wade, M.; Schwab, S.; Corsi, R. L.; Grassian, V. H., Crystal Clear? Microspectroscopic Imaging and Physicochemical Characterization of Indoor Depositions on Window Glass. *Environmental Science & Technology Letters* **2018**, *5*, 514-519.
42. Fang, Y.; Lakey, P.; Riahi, S.; McDonald, A.; Shrestha, M.; Tobias, D. J.; Grassian, V. H., A Molecular Picture of Surface Interactions of Organic Compounds on Prevalent Indoor Surfaces: Limonene Adsorption on SiO<sub>2</sub>. *Chem. Sci.* **2019**, *10*, 2906-14.
43. Fang, Y.; Riahi, S.; McDonald, A. T.; Shrestha, M.; Tobias, D. J.; Grassian, V. H., What Is the Driving Force Behind the Adsorption of Hydrophobic Molecules on Hydrophilic Surfaces? *The Journal of Physical Chemistry Letters* **2019**, *10*, 468-473.
44. Molhave, L., The Sick Buildings and Other Buildings with Indoor Climate Problems. *Environment International* **1989**, *15*, 65-74.
45. Weschler, C. J.; Shields, H. C., Potential Reactions among Indoor Pollutants. *Atmos. Environ.* **1997**, *31*, 3487-3495.

46. Bruce, N.; Perez-Padilla, R.; Albalak, R., Indoor Air Pollution in Developing Countries: A Major Environmental and Public Health Challenge. *Bulletin of the World Health Organization* **2000**, *78*, 1078-1092.
47. Spengler, J. D.; Chen, Q. Y., Indoor Air Quality Factors in Designing a Healthy Building. *Annual Review of Energy and the Environment* **2000**, *25*, 567-600.
48. Fisk, W. J., Health and Productivity Gains from Better Indoor Environments and Their Relationship with Building Energy Efficiency. *Annual Reviews of Energy and the Environment* **2000**, *25*, 537-566.
49. Patino, E. D. L.; Siegel, J. A., Indoor Environmental Quality in Social Housing: A Literature Review. *Building and Environment* **2018**, *131*, 231-241.
50. Wolkoff, P., Indoor Air Humidity, Air Quality, and Health – an Overview. *International Journal of Hygiene and Environmental Health* **2018**, *221*, 376-390.
51. Farmer, D. K., Analytical Challenges and Opportunities for Indoor Air Chemistry Field Studies. *Analytical Chemistry* **2019**, *91*, 3761-3767.
52. Abbatt, J. P. D.; Wang, C., The Atmospheric Chemistry of Indoor Environments. *Environ. Sci. Process Impacts* **2020**, *22*, 25-48.
53. Laskin, J.; Laskin, A.; Nizkorodov, S. A., Mass Spectrometry Analysis in Atmospheric Chemistry. *Analytical Chemistry* **2018**, *90*, 166-189.
54. Weschler, C. J., Ozone in Indoor Environments: Concentration and Chemistry. *Indoor Air* **2000**, *10*, 269-288.
55. Eichler, C. M. A.; Cao, J.; Isaacman-VanWertz, G.; Little, J. C., Modeling the Formation and Growth of Organic Films on Indoor Surfaces. *Indoor Air* **2019**, *29*, 17-29.
56. Lederer, M. R.; Staniec, A. R.; Coates Fuentes, Z. L.; Van Ry, D. A.; Hinrichs, R. Z., Heterogeneous Reactions of Limonene on Mineral Dust: Impacts of Adsorbed Water and Nitric Acid. *The Journal of Physical Chemistry A* **2016**, *120*, 9545-9556.
57. Ault, A. P.; Axson, J. L., Atmospheric Aerosol Chemistry: Spectroscopic and Microscopic Advances. *Analytical Chemistry* **2017**, *89*, 430-452.
58. Farmer, D. K., et al., Overview of Homechem: House Observations of Microbial and Environmental Chemistry. *Environ. Sci. Process Impacts* **2019**, *21*, 1280-1300.

59. Wisthaler, A.; Tamás, G.; Wyon, D. P.; Strøm-Tejsen, P.; Space, D.; Beauchamp, J.; Hansel, A.; Märk, T. D.; Weschler, C. J., Products of Ozone-Initiated Chemistry in a Simulated Aircraft Environment. *Environmental Science & Technology* **2005**, *39*, 4823-4832.
60. Weschler, C. J.; Wisthaler, A.; Cowlin, S.; Tamás, G.; Strøm-Tejsen, P.; Hodgson, A. T.; Destailats, H.; Herrington, J.; Zhang, J.; Nazaroff, W. W., Ozone-Initiated Chemistry in an Occupied Simulated Aircraft Cabin. *Environmental Science & Technology* **2007**, *41*, 6177-6184.
61. Wong, J. P. S.; Carslaw, N.; Zhao, R.; Zhou, S.; Abbatt, J. P. D., Observations and Impacts of Bleach Washing on Indoor Chlorine Chemistry. *Indoor Air* **2017**, *27*, 1082-1090.
62. Collins, D. B.; Hems, R. F.; Zhou, S. M.; Wang, C.; Grignon, E.; Alavy, M.; Siegel, J. A.; Abbatt, J. P. D., Evidence for Gas-Surface Equilibrium Control of Indoor Nitrous Acid. *Environmental Science & Technology* **2018**, *52*, 12419-12427.
63. Schmidt, C. M.; Buchbinder, A.; Weitz, E.; Geiger, F. M., Photochemistry of the Indoor Air Pollutant Acetone on Degussa P25 TiO<sub>2</sub> Studied by Chemical Ionization Mass Spectrometry. *J. Phys. Chem. A* **2007**, *111*, 13023-13031.
64. Schmidt, C. M.; Weitz, E.; Geiger, F. M., Interaction of the Indoor Air Pollutant Acetone with Degussa P25 TiO<sub>2</sub> Studied by Chemical Ionization Mass Spectrometry. *Langmuir* **2006**, *22*, 9642-9650.
65. Wisthaler, A.; Weschler, C. J., Reactions of Ozone with Human Skin Lipids: Sources of Carbonyls, Dicarboxyls, and Hydroxycarbonyls in Indoor Air. *Proceedings of the National Academy of Sciences* **2010**, *107*, 6568-6575.
66. Arata, C.; Heine, N.; Wang, N.; Misztal, P. K.; Wargocki, P.; Bekö, G.; Williams, J.; Nazaroff, W. W.; Wilson, K. R.; Goldstein, A. H., Heterogeneous Ozonolysis of Squalene: Gas-Phase Products Depend on Water Vapor Concentration. *Environmental Science & Technology* **2019**, *53*, 14441-14448.
67. Zhou, S. M.; Forbes, M. W.; Abbatt, J. P. D., Application of Direct Analysis in Real Time-Mass Spectrometry (Dart-MS) to the Study of Gas-Surface Heterogeneous Reactions: Focus on Ozone and PAHs. *Analytical Chemistry* **2015**, *87*, 4733-4740.
68. Zhou, S. M.; Forbes, M. W.; Abbatt, J. P. D., Kinetics and Products from Heterogeneous Oxidation of Squalene with Ozone. *Environmental Science & Technology* **2016**, *50*, 11688-11697.
69. Zhou, S. M.; Forbes, M. W.; Katrib, Y.; Abbatt, J. P. D., Rapid Oxidation of Skin Oil by Ozone. *Environmental Science & Technology Letters* **2016**, *3*, 170-174.

70. Schwartz-Narbonne, H.; Wang, C.; Zhou, S.; Abbatt, J. P. D.; Faust, J., Heterogeneous Chlorination of Squalene and Oleic Acid. *Environmental Science & Technology* **2019**, *53*, 1217-1224.
71. Zhou, S. M.; Yeung, L. W. Y.; Forbes, M. W.; Mabury, S.; Abbatt, J. P. D., Epoxide Formation from Heterogeneous Oxidation of Benzo a Pyrene with Gas-Phase Ozone and Indoor Air. *Environmental Science-Processes & Impacts* **2017**, *19*, 1292-1299.
72. Alwarda, R.; Zhou, S.; Abbatt, J. P. D., Heterogeneous Oxidation of Indoor Surfaces by Gas-Phase Hydroxyl Radicals. *Indoor Air* **2018**, *28*, 655-664.
73. Petrick, L.; Dubowski, Y., Heterogeneous Oxidation of Squalene Film by Ozone under Various Indoor Conditions. *Indoor Air* **2009**, *19*, 381-391.
74. Zhou, Z.; Zhou, S.; Abbatt, J. P. D., Kinetics and Condensed-Phase Products in Multiphase Ozonolysis of an Unsaturated Triglyceride. *Environmental Science & Technology* **2019**, *53*, 12467-12475.
75. O'Brien, R. E., et al., Ultrasonic Nebulization for the Elemental Analysis of Microgram-Level Samples with Offline Aerosol Mass Spectrometry. *Atmos. Meas. Tech.* **2019**, *12*, 1659-1671.
76. Ault, A. P., et al., Size-Dependent Changes in Sea Spray Aerosol Composition and Properties with Different Seawater Conditions. *Environmental Science & Technology* **2013**, *47*, 5603-5612.
77. Ault, A. P.; Guasco, T. L.; Ryder, O. S.; Baltrusaitis, J.; Cuadra-Rodriguez, L. A.; Collins, D. B.; Ruppel, M. J.; Bertram, T. H.; Prather, K. A.; Grassian, V. H., Inside Versus Outside: Ion Redistribution in Nitric Acid Reacted Sea Spray Aerosol Particles as Determined by Single Particle Analysis. *Journal of the American Chemical Society* **2013**, *135*, 14528-14531.
78. Hamdan, N. M.; Alawadhi, H.; Jisrawi, N.; Shameer, M., Size-Resolved Analysis of Fine and Ultrafine Fractions of Indoor Particulate Matter Using Energy Dispersive X-Ray Fluorescence and Electron Microscopy. *X-Ray Spectrometry* **2018**, *47*, 72-78.
79. Rindelaub, J. D.; Craig, R. L.; Nandy, L.; Bondy, A. L.; Dutcher, C. S.; Shepson, P. B.; Ault, A. P., Direct Measurement of Ph in Individual Particles Via Raman Microspectroscopy and Variation in Acidity with Relative Humidity. *The Journal of Physical Chemistry A* **2016**, *120*, 911-917.

80. Craig, R. L.; Nandy, L.; Axson, J. L.; Dutcher, C. S.; Ault, A. P., Spectroscopic Determination of Aerosol Ph from Acid–Base Equilibria in Inorganic, Organic, and Mixed Systems. *The Journal of Physical Chemistry A* **2017**, *121*, 5690-5699.
81. Fang, Y.; Lesnicki, D.; Wall, K. J.; Gageot, M.-P.; Sulpizi, M.; Vaida, V.; Grassian, V. H., Heterogeneous Interactions between Gas-Phase Pyruvic Acid and Hydroxylated Silica Surfaces: A Combined Experimental and Theoretical Study. *J. Phys. Chem. A* **2019**, *123*, 983-991.
82. Hung, H.-M.; Tang, C.-W., Effects of Temperature and Physical State on Heterogeneous Oxidation of Oleic Acid Droplets with Ozone. *The Journal of Physical Chemistry A* **2010**, *114*, 13104-13112.
83. Fu, D.; Leng, C.; Kelley, J.; Zeng, G.; Zhang, Y.; Liu, Y., Atr-Ir Study of Ozone Initiated Heterogeneous Oxidation of Squalene in an Indoor Environment. *Environmental Science & Technology* **2013**, *47*, 10611-10618.
84. Bondy, A. L.; Kirpes, R. M.; Merzel, R. L.; Pratt, K. A.; Banaszak Holl, M. M.; Ault, A. P., Atomic Force Microscopy-Infrared Spectroscopy of Individual Atmospheric Aerosol Particles: Subdiffraction Limit Vibrational Spectroscopy and Morphological Analysis. *Analytical Chemistry* **2017**, *89*, 8594-8598.
85. Or, V. W.; Estillore, A. D.; Tivanski, A. V.; Grassian, V. H., Lab on a Tip: Atomic Force Microscopy – Photothermal Infrared Spectroscopy of Atmospherically Relevant Organic/Inorganic Aerosol Particles in the Nanometer to Micrometer Size Range. *Analyst* **2018**, *143*, 2765-2774.
86. Voges, A. B.; Stokes, G. Y.; Gibbs-Davis, J. M.; Lettan, R. B.; Bertin, P. A.; Pike, R. C.; Nguyen, S. T.; Scheidt, K. A.; Geiger, F. M., Insights into Heterogeneous Atmospheric Oxidation Chemistry: Development of a Tailor-Made Synthetic Model for Studying Tropospheric Surface Chemistry. *J. Phys. Chem. C* **2007**, *111*, 1567-1578.
87. Stokes, G. Y.; Buchbinder, A. M.; Gibbs-Davis, J. M.; Scheidt, K. A.; Geiger, F. M., Heterogeneous Ozone Oxidation Reactions of 1-Pentene, Cyclopentene, Cyclohexene, and a Menthenol Derivative Studied by Sum Frequency Generation. *J. Phys. Chem. A* **2008**, *112*, 11688-11698.
88. Stokes, G. Y.; Chen, E. H.; Walter, S. R.; Geiger, F. M., Two Reactivity Modes in the Heterogeneous Cyclohexene Ozonolysis under Tropospheric Relevant Ozone-Rich and Ozone-Limited Conditions. *J. Phys. Chem. A* **2009**, *113*, 8985-8993.



89. Stokes, G. Y.; Buchbinder, A. M.; Gibbs-Davis, J. M.; Scheidt, K. A.; Geiger, F. M., Chemically Diverse Environmental Interfaces and Their Reactions with Ozone Studied by Sum Frequency Generation. *Vibrational Spectroscopy* **2009**, *50*, 86-98.
90. Stokes, G. Y.; Chen, E. H.; Buchbinder, A. M.; Paxton, W. F.; Keeley, A.; Geiger, F. M., Atmospheric Heterogeneous Stereochemistry. *J. Am. Chem. Soc.* **2009**, *131*, 13733-13737.
91. Ebben, C. J., et al., Contrasting Organic Aerosol Particles from Boreal and Tropical Forests During Humppa-Copec-2010 and Amaze-08 Using Coherent Vibrational Spectroscopy. *Atmos. Chem. Phys.* **2011**, *11*, 10317-10329.
92. Ault, A. P.; Zhao, D.; Ebben, C. J.; Tauber, M. J.; Geiger, F. M.; Prather, K. A.; Grassian, V. H., Raman Microspectroscopy and Vibrational Sum Frequency Generation Spectroscopy as Probes of the Bulk and Surface Compositions of Size-Resolved Sea Spray Aerosol Particles. *PCCP* **2013**, *15*, 6206-6214.
93. Ebben, C. J.; Ault, A. P.; Ruppel, M. J.; Ryder, O. S.; Bertram, T. H.; Grassian, V. H.; Prather, K. A.; Geiger, F. M., Size-Resolved Sea Spray Aerosol Particles Studied by Vibrational Sum Frequency Generation. *The Journal of Physical Chemistry A* **2013**, *117*, 6589-6601.
94. Shrestha, M.; Zhang, Y.; Ebben, C. J.; Martin, S. T.; Geiger, F. M., Vibrational Sum Frequency Generation Spectroscopy of Secondary Organic Material Produced by Condensational Growth from  $\alpha$ -Pinene Ozonolysis. *The Journal of Physical Chemistry A* **2013**, *117*, 8427-8436.
95. Ebben, C. J.; Strick, B. F.; Upshur, M. A.; Chase, H. M.; Achtyl, J. L.; Thomson, R. J.; Geiger, F. M., Towards the Identification of Molecular Constituents Associated with the Surfaces of Isoprene-Derived Secondary Organic Aerosol (Soa) Particles. *Atmospheric Chemistry and Physics* **2014**, *14*, 2303-2314.
96. Shrestha, M.; Zhang, Y.; Upshur, M. A.; Liu, P.; Blair, S. L.; Wang, H.-f.; Nizkorodov, S. A.; Thomson, R. J.; Martin, S. T.; Geiger, F. M., On Surface Order and Disorder of  $\alpha$ -Pinene-Derived Secondary Organic Material. *The Journal of Physical Chemistry A* **2015**, *119*, 4609-4617.
97. Chase, H. M.; Ho, J.; Upshur, M. A.; Thomson, R. J.; Batista, V. S.; Geiger, F. M., Unanticipated Stickiness of  $\alpha$ -Pinene. *The Journal of Physical Chemistry A* **2017**, *121*, 3239-3246.
98. Liu, Y.; Chase, H. M.; Geiger, F. M., Partially (Resp. Fully) Reversible Adsorption of Monoterpenes (Resp. Alkanes and Cycloalkanes) to Fused Silica. *J. Chem. Phys.* **2019**, *150*, 074701.

99. Bé, A. G., et al., Atmospheric B-Caryophyllene-Derived Ozonolysis Products at Interfaces. *ACS Earth and Space Chemistry* **2019**, *3*, 158-169.
100. Bé, A. G.; Liu, Y.; Tuladhar, A.; Bellcross, A. D.; Wang, Z.; Thomson, R. J.; Geiger, F. M., Surface-Active B-Caryophyllene Oxidation Products at the Air/Aqueous Interface. *ACS Earth and Space Chemistry* **2019**, *3*, 1740-1748.
101. Bé, A. G.; Upshur, M. A.; Liu, P.; Martin, S. T.; Geiger, F. M.; Thomson, R. J., Cloud Activation Potentials for Atmospheric A-Pinene and B-Caryophyllene Ozonolysis Products. *ACS Cent. Sci.* **2017**, *3*, 715-725.
102. Schwartz-Narbonne, H.; Donaldson, D. J., Water Uptake by Indoor Surface Films. *Scientific Reports* **2019**, *9*, 11089.
103. Liu, P.; Li, Y. J.; Wang, Y.; Gilles, M. K.; Zaveri, R. A.; Bertram, A. K.; Martin, S. T., Lability of Secondary Organic Particulate Matter. *Proceedings of the National Academy of Sciences* **2016**, *113*, 12643-12648.
104. Liu, P., et al., Resolving the Mechanisms of Hygroscopic Growth and Cloud Condensation Nuclei Activity for Organic Particulate Matter. *Nature communications* **2018**, *9*, 4076.
105. Malecha, K. T.; Cai, Z.; Nizkorodov, S. A., Photodegradation of Secondary Organic Aerosol Material Quantified with a Quartz Crystal Microbalance. *Environmental Science & Technology Letters* **2018**, *5*, 366-371.
106. Shen, Y. R., *The Principles of Nonlinear Optics*; John Wiley & Sons: New York, 1984.
107. Zhuang, X.; Miranda, P. B.; Kim, D.; Shen, Y. R., Mapping Molecular Orientation and Conformation at Interfaces by Surface Nonlinear Optics. *Physical Review B* **1999**, *59*, 12632-12640.
108. Wang, H.-F.; Gan, W.; Lu, R.; Rao, Y.; Wu, B.-H., Quantitative Spectral and Orientational Analysis in Surface Sum Frequency Generation Vibrational Spectroscopy (Sfg-Vs). *International Reviews in Physical Chemistry* **2005**, *24*, 191-256.
109. Stokes, G. Y.; Buchbinder, A. M.; Gibbs-Davis, J. M.; Scheidt, K. A.; Geiger, F. M., Chemically Diverse Environmental Interfaces and Their Reactions with Ozone Studied by Sum Frequency Generation. *Vibrational Spectroscopy* **2009**, *50*, 86-98.
110. Buchbinder, A. M.; Gibbs-Davis, J. M.; Stokes, G. Y.; Peterson, M. D.; Weitz, E.; Geiger, F. M., Method for Evaluating Vibrational Mode Assignments in Surface-Bound Cyclic

Hydrocarbons Using Sum-Frequency Generation. *The Journal of Physical Chemistry C* **2011**, *115*, 18284-18294.

111. Lu, R.; Gan, W.; Wu, B.-h.; Zhang, Z.; Guo, Y.; Wang, H.-f., C–H Stretching Vibrations of Methyl, Methylene and Methine Groups at the Vapor/Alcohol (N = 1–8) Interfaces. *The Journal of Physical Chemistry B* **2005**, *109*, 14118-14129.

112. Doğangün, M.; Ohno, P. E.; Liang, D.; McGeachy, A. C.; Bé, A. G.; Dalchand, N.; Li, T.; Cui, Q.; Geiger, F. M., Hydrogen-Bond Networks near Supported Lipid Bilayers from Vibrational Sum Frequency Generation Experiments and Atomistic Simulations. *The Journal of Physical Chemistry B* **2018**, *122*, 4870-4879.

113. Liggio, J.; Li, S. M.; Brook, J. R.; Mihele, C., Direct Polymerization of Isoprene and A-Pinene on Acidic Aerosols. *Geophysical Research Letters* **2007**, *34*.

114. Li, Y. J.; Cheong, G. Y. L.; Lau, A. P. S.; Chan, C. K., Acid-Catalyzed Condensed-Phase Reactions of Limonene and Terpineol and Their Impacts on Gas-to-Particle Partitioning in the Formation of Organic Aerosols. *Environmental Science & Technology* **2010**, *44*, 5483-5489.

115. Cheshchevoi, V. N.; Diner, V. A.; Polushkin, V. A., Cyclization and Oxidation of Isoprene Oligomers During Polymerization on Kaolinite. *Polymer Science U.S.S.R.* **1987**, *29*, 868-874.

116. Cheshchevoi, V. N.; Palamarev, D. N.; Diner, V. A.; Polushkin, V. A., Spectral Study of the Oligomerization Products of A-Pinene on Kaolinite. *Polymer Science U.S.S.R.* **1989**, *31*, 2274-2279.

117. Roberge, D. M.; Buhl, D.; Niederer, J. P. M.; Hölderich, W. F., Catalytic Aspects in the Transformation of Pinenes to P-Cymene. *Applied Catalysis A: General* **2001**, *215*, 111-124.

118. Ravasio, N.; Zaccheria, F.; Guidotti, M.; Psaro, R., Mono- and Bifunctional Heterogeneous Catalytic Transformation of Terpenes and Terpenoids. *Topics in Catalysis* **2004**, *27*, 157-168.

119. Strick, B. F.; Delferro, M.; Geiger, F. M.; Thomson, R. J., Investigations into Apopinene as a Biorenewable Monomer for Ring-Opening Metathesis Polymerization. *ACS Sustainable Chemistry & Engineering* **2015**, *3*, 1278-1281.

120. Frattini, L.; Isaacs, M. A.; Parlett, C. M. A.; Wilson, K.; Kyriakou, G.; Lee, A. F., Support Enhanced A-Pinene Isomerization over Hpw/Sba-15. *Applied Catalysis B: Environmental* **2017**, *200*, 10-18.

121. Ho, J.; Psciuk, B. T.; Chase, H. M.; Rudshiteyn, B.; Upshur, M. A.; Fu, L.; Thomson, R. J.; Wang, H.-F.; Geiger, F. M.; Batista, V. S., Sum Frequency Generation Spectroscopy and Molecular Dynamics Simulations Reveal a Rotationally Fluid Adsorption State of  $\alpha$ -Pinene on Silica. *The Journal of Physical Chemistry C* **2016**, *120*, 12578-12589.
122. Kesselmeier, J.; Staudt, M., Biogenic Volatile Organic Compounds (Voc): An Overview on Emission, Physiology and Ecology. *Journal of Atmospheric Chemistry* **1999**, *33*, 23-88.
123. Karl, T.; Guenther, A.; Yokelson, R. J.; Greenberg, J.; Potosnak, M.; Blake, D. R.; Artaxo, P., The Tropical Forest and Fire Emissions Experiment: Emission, Chemistry, and Transport of Biogenic Volatile Organic Compounds in the Lower Atmosphere over Amazonia. *Journal of Geophysical Research: Atmospheres* **2007**, *112*.
124. Atkinson, R., Kinetics and Mechanisms of the Gas-Phase Reactions of the Hydroxyl Radical with Organic Compounds under Atmospheric Conditions. *Chemical Reviews* **1986**, *86*, 69-201.
125. Atkinson, R., Gas-Phase Tropospheric Chemistry of Volatile Organic Compounds: 1. Alkanes and Alkenes. *Journal of Physical and Chemical Reference Data* **1997**, *26*, 215-290.
126. Calero, S.; Gómez-Álvarez, P., On the Performance of Fau and Mfi Zeolites for the Adsorptive Removal of a Series of Volatile Organic Compounds from Air Using Molecular Simulation. *Physical Chemistry Chemical Physics* **2015**, *17*, 26451-26455.
127. Yang, M.; Somorjai, G. A., Adsorption and Reactions of C<sub>6</sub> Hydrocarbons at High Pressures on Pt(111) Single-Crystal Surfaces Studied by Sum Frequency Generation Vibrational Spectroscopy: Mechanisms of Isomerization and Dehydrocyclization of N-Hexane. *Journal of the American Chemical Society* **2004**, *126*, 7698-7708.
128. Kholdeeva, O. A.; Skobelev, I. Y.; Ivanchikova, I. D.; Kovalenko, K. A.; Fedin, V. P.; Sorokin, A. B., Hydrocarbon Oxidation over Fe- and Cr-Containing Metal-Organic Frameworks Mil-100 and Mil-101—a Comparative Study. *Catalysis Today* **2014**, *238*, 54-61.
129. Ebben, C. J.; Strick, B.; Upshur, M.; Chase, H.; L. Achtyl, J.; J. Thomson, R.; Geiger, F., Towards the Identification of Molecular Constituents Associated with the Surfaces of Isoprene-Derived Secondary Organic Aerosol (Soa) Particles. *Atmos. Chem. Phys.* **2014**, *14*, 2303-2314.
130. Morita, A., *Theory of Sum Frequency Generation Spectroscopy*; Springer, 2018; Vol. 97.
131. Mukamel, S., *Principles of Nonlinear Optical Spectroscopy*; Oxford University Press: Oxford, 1995.

132. Boyd, R. W., *Nonlinear Optics*; Academic Press: New York, 1992.
133. Buchbinder, A. M.; Weitz, E.; Geiger, F. M., Pentane, Hexane, Cyclopentane, Cyclohexane, 1-Hexene, 1-Pentene, Cis-2-Pentene, Cyclohexene, and Cyclopentene at Vapor/A-Alumina and Liquid/A-Alumina Interfaces Studied by Broadband Sum Frequency Generation. *The Journal of Physical Chemistry C* **2010**, *114*, 554-566.
134. Brindza, M. R.; Ding, F.; Fourkas, J. T.; Walker, R. A., N-Alkane Adsorption to Polar Silica Surfaces. *The Journal of chemical physics* **2010**, *132*, 114701.
135. Buchbinder, A. M.; Weitz, E.; Geiger, F. M., When the Solute Becomes the Solvent: Orientation, Ordering, and Structure of Binary Mixtures of 1-Hexanol and Cyclohexane over the (0001) A-Al<sub>2</sub>O<sub>3</sub> Surface. *J. Am. Chem. Soc.* **2010**, *132*, 14661-14668.
136. Buchbinder, A. M.; Ray, N. A.; Lu, J.; Van Duyne, R. P.; Stair, P. C.; Weitz, E.; Geiger, F. M., Displacement of Hexanol by the Hexanoic Acid Overoxidation Product in Alcohol Oxidation on a Model Supported Palladium Nanoparticle Catalyst. *J. Am. Chem. Soc.* **2011**, *133*, 17816-17823.
137. Nanjundiah, K.; Dhinojwala, A., Confinement-Induced Ordering of Alkanes between an Elastomer and a Solid Surface. *Physical Review Letters* **2005**, *95*, 154301.
138. Esenturk, O.; Walker, R. A., Surface Vibrational Structure at Alkane Liquid/Vapor Interfaces. *The Journal of Chemical Physics* **2006**, *125*.
139. Guyot-Sionnest, P.; Hunt, J. H.; Shen, Y. R., Sum-Frequency Vibrational Spectroscopy of a Langmuir Film: Study of Molecular Orientation of a Two-Dimensional System. *Physical Review Letters* **1987**, *59*, 1597-1600.
140. MacPhail, R. A.; Strauss, H. L.; Snyder, R. G.; Elliger, C. A., Carbon-Hydrogen Stretching Modes and the Structure of N-Alkyl Chains. 2. Long, All-Trans Chains. *The Journal of Physical Chemistry* **1984**, *88*, 334-341.
141. Snyder, R. G., Group Moment Interpretation of the Infrared Intensities of Crystalline N-Paraffins. *The Journal of Chemical Physics* **1965**, *42*, 1744-1763.
142. Yaws, C. L.; Satyro, M. A., Chapter 1 - Vapor Pressure – Organic Compounds. In *The Yaws Handbook of Vapor Pressure*, Gulf Professional Publishing: 2015; pp 1-314.
143. Yaws, C. L., *Handbook of Vapor Pressure. Co., Houston* **1994**.

144. Stephenson, R. M.; Malanowski, S.; Ambrose, D., *A Handbook of the Thermodynamics of Organic Compounds*, 1978.
145. Desiraju, G. R., Iupac Definition of the Hydrogen Bond. Terminology and Nomenclature. In *the 24th Congress and General Assembly of the International Union of Crystallography*, Hyderabad, India, 2017.
146. Geiger, F. M.; Tridico, A. C.; Hicks, J. M., Second Harmonic Generation Studies of Ozone Depletion Reactions on Ice Surfaces under Stratospheric Conditions. *The Journal of Physical Chemistry B* **1999**, *103*, 8205-8215.
147. Wilmsmeyer, A. R.; Uzarski, J.; Barrie, P. J.; Morris, J. R., Interactions and Binding Energies of Dimethyl Methylphosphonate and Dimethyl Chlorophosphate with Amorphous Silica. *Langmuir* **2012**, *28*, 10962-10967.
148. Wilmsmeyer, A. R.; Gordon, W. O.; Davis, E. D.; Troya, D.; Mantooth, B. A.; Lalain, T. A.; Morris, J. R., Infrared Spectra and Binding Energies of Chemical Warfare Nerve Agent Simulants on the Surface of Amorphous Silica. *The Journal of Physical Chemistry C* **2013**, *117*, 15685-15697.
149. Abelard, J.; Wilmsmeyer, A. R.; Edwards, A. C.; Gordon, W. O.; Durke, E. M.; Karwacki, C. J.; Troya, D.; Morris, J. R., Adsorption of 2-Chloroethyl Ethyl Sulfide on Silica: Binding Mechanism and Energy of a Bifunctional Hydrogen-Bond Acceptor at the Gas-Surface Interface. *The Journal of Physical Chemistry C* **2015**, *119*, 365-372.
150. Abelard, J.; Wilmsmeyer, A. R.; Edwards, A. C.; Gordon, W. O.; Durke, E. M.; Karwacki, C. J.; Troya, D.; Morris, J. R., Adsorption of Substituted Benzene Derivatives on Silica: Effects of Electron Withdrawing and Donating Groups. *The Journal of Physical Chemistry C* **2016**, *120*, 13024-13031.
151. Raval, R.; Parker, S. F.; Chesters, M. A., C-H ... M Interactions and Orientational Changes of Cyclohexane on Cu(111): A Rairs, Eels and Leed Study. *Surface Science* **1993**, *289*, 227-236.
152. Stiopkin, I. V.; Jayathilake, H. D.; Bordenyuk, A. N.; Benderskii, A. V., Heterodyne-Detected Vibrational Sum Frequency Generation Spectroscopy. *Journal of the American Chemical Society* **2008**, *130*, 2271-2275.
153. Fu, L.; Chen, S.-L.; Wang, H.-F., Validation of Spectra and Phase in Sub-1 Cm<sup>-1</sup> Resolution Sum-Frequency Generation Vibrational Spectroscopy through Internal Heterodyne Phase-Resolved Measurement. *The Journal of Physical Chemistry B* **2016**, *120*, 1579-1589.

154. Vanselow, H.; Petersen, P. B., Extending the Capabilities of Heterodyne-Detected Sum-Frequency Generation Spectroscopy: Probing Any Interface in Any Polarization Combination. *The Journal of Physical Chemistry C* **2016**, *120*, 8175-8184.
155. Fiegand, L. R.; McCorn Saint Fleur, M.; Morris, J. R., Reactions of C:C-Terminated Self-Assembled Monolayers with Gas-Phase Ozone. *Langmuir* **2005**, *21*, 2660-2661.
156. D'Andrea, T. M. D.; Zhang, X.; Jochnowitz, E. B.; Lindeman, T. G.; Simpson, C. J. S. M.; David, D. E.; Curtiss, T. J.; Morris, J. R.; Ellison, G. B., Oxidation of Organic Films by Beams of Hydroxyl Radicals. *J. Phys. Chem. B* **2008**, *112*, 535-544.
157. Dubowski, Y.; Vieceli, J.; Tobias, D. J.; Gomez, A.; Lin, A.; Nizkorodov, S. A.; McIntire, T. M.; Finlayson-Pitts, B. J., Interaction of Gas-Phase Ozone at 296 K with Unsaturated Self-Assembled Monolayers: A New Look at an Old System. *Journal of Physical Chemistry A* **2004**, *108*, 10473-10485.
158. Stokes, G. Y.; Buchbinder, A. M.; Gibbs-Davis, J. M.; Scheidt, K. A.; Geiger, F. M., Heterogeneous Ozone Oxidation Reactions of 1-Pentene, Cyclopentene, Cyclohexene, and a Menthenol Derivative Studied by Sum Frequency Generation. *The Journal of Physical Chemistry A* **2008**, *112*, 11688-11698.
159. Stokes, G. Y.; Chen, E. H.; Walter, S. R.; Geiger, F. M., Two Reactivity Modes in the Heterogeneous Cyclohexene Ozonolysis under Tropospherically Relevant Ozone-Rich and Ozone-Limited Conditions. *The Journal of Physical Chemistry A* **2009**, *113*, 8985-8993.
160. Buchbinder, A. M.; Gibbs-Davis, J. M.; Stokes, G. Y.; Peterson, M. D.; Weitz, E.; Geiger, F. M., Method for Evaluating Vibrational Mode Assignments in Surface-Bound Cyclic Hydrocarbons Using Sum-Frequency Generation. *J. Phys. Chem. C* **2011**, *115*, 18284-18294.
161. Upshur, M. A.; Chase, H. M.; Strick, B. F.; Ebben, C. J.; Fu, L.; Wang, H.; Thomson, R. J.; Geiger, F. M., Vibrational Mode Assignment of A-Pinene by Isotope Editing: One Down, Seventy-One to Go. *The Journal of Physical Chemistry A* **2016**, *120*, 2684-2690.
162. Upshur, M. A., et al., Synthesis and Surface Spectroscopy of A-Pinene Isotopologues and Their Corresponding Secondary Organic Material. *Chemical Science* **2019**, *10*, 8390-8398.
163. Morrison, G., Recent Advances in Indoor Chemistry. *Current Sustainable/Renewable Energy Reports* **2015**, *2*, 33-40.
164. Weschler, C. J., Roles of the Human Occupant in Indoor Chemistry. *Indoor Air* **2016**, *26*, 6-24.

165. Weschler, C. J.; Carslaw, N., Indoor Chemistry. *Environmental Science & Technology* **2018**, *52*, 2419-2428.
166. Morrison, G., Interfacial Chemistry in Indoor Environments. *Environmental Science & Technology* **2008**, *42*, 3495-3499.
167. Shiraiwa, M., et al., Modelling Consortium for Chemistry of Indoor Environments (Moccie): Integrating Chemical Processes from Molecular to Room Scales. *Environmental Science: Processes & Impacts* **2019**, *21*, 1240-1254.
168. Weschler, C. J.; Nazaroff, W. W., Growth of Organic Films on Indoor Surfaces. *Indoor Air* **2017**, *27*, 1101-1112.
169. Wu, Y.; Eichler, C. M. A.; Leng, W.; Cox, S. S.; Marr, L. C.; Little, J. C., Adsorption of Phthalates on Impervious Indoor Surfaces. *Environmental Science & Technology* **2017**, *51*, 2907-2913.
170. Bi, C.; Liang, Y.; Xu, Y., Fate and Transport of Phthalates in Indoor Environments and the Influence of Temperature: A Case Study in a Test House. *Environmental Science & Technology* **2015**, *49*, 9674-9681.
171. Liu, Q.-T.; Chen, R.; McCarry, B. E.; Diamond, M. L.; Bahavar, B., Characterization of Polar Organic Compounds in the Organic Film on Indoor and Outdoor Glass Windows. *Environmental Science & Technology* **2003**, *37*, 2340-2349.
172. Morrison, G.; Shakila, N. V.; Parker, K., Accumulation of Gas-Phase Methamphetamine on Clothing, Toy Fabrics, and Skin Oil. *Indoor Air* **2015**, *25*, 405-414.
173. Goodman, A. L.; Bernard, E. T.; Grassian, V. H., Spectroscopic Study of Nitric Acid and Water Adsorption on Oxide Particles: Enhanced Nitric Acid Uptake Kinetics in the Presence of Adsorbed Water. *The Journal of Physical Chemistry A* **2001**, *105*, 6443-6457.
174. Fang, Y.; Tang, M.; Grassian, V. H., Competition between Displacement and Dissociation of a Strong Acid Compared to a Weak Acid Adsorbed on Silica Particle Surfaces: The Role of Adsorbed Water. *The Journal of Physical Chemistry A* **2016**, *120*, 4016-4024.
175. Tang, M.; Larish, W. A.; Fang, Y.; Gankanda, A.; Grassian, V. H., Heterogeneous Reactions of Acetic Acid with Oxide Surfaces: Effects of Mineralogy and Relative Humidity. *The Journal of Physical Chemistry A* **2016**, *120*, 5609-5616.
176. Buchbinder, A.; Weitz, E.; Geiger, F. M., Pentane, Hexane, Cyclopentane, Cyclohexane, 1-Hexene, 1-Pentene, Cis-2-Pentene, Cyclohexene, and Cyclopentene at Vapor/A-Alumina and



Liquid/A-Alumina Interfaces Studied by Broadband Sum Frequency Generation. *J. Phys. Chem. C ASAP Article* **2009**.

177. Lee, C.-S.; Haghghat, F.; Ghaly, W. S., A Study on Voc Source and Sink Behavior in Porous Building Materials – Analytical Model Development and Assessment. *Indoor Air* **2005**, *15*, 183-196.

178. Baltrusaitis, J.; Schuttlefield, J.; Jensen, J. H.; Grassian, V. H., Ftir Spectroscopy Combined with Quantum Chemical Calculations to Investigate Adsorbed Nitrate on Aluminium Oxide Surfaces in the Presence and Absence of Co-Adsorbed Water. *Phys Chem Chem Phys* **2007**, *9*, 4970-4980.

179. Pöschl, U.; Letzel, T.; Schauer, C.; Niessner, R., Interaction of Ozone and Water Vapor with Spark Discharge Soot Aerosol Particles Coated with Benzo[a]Pyrene: O<sub>3</sub> and H<sub>2</sub>O Adsorption, Benzo[a]Pyrene Degradation, and Atmospheric Implications. *The Journal of Physical Chemistry A* **2001**, *105*, 4029-4041.

180. Wang, J.; Paszti, Z.; Even, M. A.; Chen, Z., Measuring Polymer Surface Ordering Differences in Air and Water by Sum Frequency Generation Vibrational Spectroscopy. *Journal of the American Chemical Society* **2002**, *124*, 7016-7023.

181. Wei, F.; Xiong, W.; Li, W.; Lu, W.; Allen, H. C.; Zheng, W., Assembly and Relaxation Behaviours of Phosphatidylethanolamine Monolayers Investigated by Polarization and Frequency Resolved Sfg-Vs. *Physical Chemistry Chemical Physics* **2015**, *17*, 25114-25122.

182. Lü, R.; Gan, W.; Wang, H., Novel Method for Accurate Determination of the Orientational Angle of Interfacial Chemical Groups. *Chinese Science Bulletin* **2003**, *48*, 2183-2187.

183. Gan, W.; Wu, B.-h.; Chen, H.; Guo, Y.; Wang, H.-f., Accuracy and Sensitivity of Determining Molecular Orientation at Interfaces Using Sum Frequency Generation Vibrational Spectroscopy. *Chemical Physics Letters* **2005**, *406*, 467-473.

184. Wang \*, H.-F.; Gan † ‡, W.; Lu † ‡ §, R.; Rao † ‡ ¶, Y.; Wu †, B.-H., Quantitative Spectral and Orientational Analysis in Surface Sum Frequency Generation Vibrational Spectroscopy (Sfg-Vs). *International Reviews in Physical Chemistry* **2005**, *24*, 191-256.

185. Wang, H.-F.; Velarde, L.; Gan, W.; Fu, L., Quantitative Sum-Frequency Generation Vibrational Spectroscopy of Molecular Surfaces and Interfaces: Lineshape, Polarization, and Orientation. *Annual Review of Physical Chemistry* **2015**, *66*, 189-216.

186. Chase, H. M.; Chen, S.; Fu, L.; Upshur, M. A.; Rudshiteyn, B.; Thomson, R. J.; Wang, H.-F.; Batista, V. S.; Geiger, F. M., Orientations of Nonlocal Vibrational Modes from Combined Experimental and Theoretical Sum Frequency Spectroscopy. *Chemical Physics Letters* **2017**, *683*, 199-204.
187. Chase, H. M.; Psciuk, B. T.; Strick, B. L.; Thomson, R. J.; Batista, V. S.; Geiger, F. M., Beyond Local Group Modes in Vibrational Sum Frequency Generation. *The Journal of Physical Chemistry A* **2015**, *119*, 3407-3414.
188. Chase, H. M.; Rudshiteyn, B.; Psciuk, B. T.; Upshur, M. A.; Strick, B. F.; Thomson, R. J.; Batista, V. S.; Geiger, F. M., Assessment of Dft for Computing Sum Frequency Generation Spectra of an Epoxydiol and a Deuterated Isotopologue at Fused Silica/Vapor Interfaces. *The Journal of Physical Chemistry B* **2016**, *120*, 1919-1927.
189. Lakey, P. S. J.; Morrison, G. C.; Won, Y.; Parry, K. M.; von Domaros, M.; Tobias, D. J.; Rim, D.; Shiraiwa, M., The Impact of Clothing on Ozone and Squalene Ozonolysis Products in Indoor Environments. *Communications Chemistry* **2019**, *2*, 56.
190. Wells, J.; Morrison, G.; Coleman, B.; Spicer, C.; Dean, S., Kinetics and Reaction Products of Ozone and Surface-Bound Squalene. *Journal of Astm International* **2008**, *5*.
191. Moise, T.; Rudich, Y., Reactive Uptake of Ozone by Aerosol-Associated Unsaturated Fatty Acids: Kinetics, Mechanism, and Products. *The Journal of Physical Chemistry A* **2002**, *106*, 6469-6476.
192. Heine, N.; Houle, F. A.; Wilson, K. R., Connecting the Elementary Reaction Pathways of Criegee Intermediates to the Chemical Erosion of Squalene Interfaces During Ozonolysis. *Environmental Science & Technology* **2017**, *51*, 13740-13748.
193. Dubowski, Y.; Vieceli, J.; Tobias, D. J.; Gomez, A.; Lin, A.; Nizkorodov, S. A.; McIntire, T. M.; Finlayson-Pitts, B. J., Interaction of Gas-Phase Ozone at 296 K with Unsaturated Self-Assembled Monolayers: A New Look at an Old System. *The Journal of Physical Chemistry A* **2004**, *108*, 10473-10485.
194. Usher, C. R.; Michel, A. E.; Stec, D.; Grassian, V. H., Laboratory Studies of Ozone Uptake on Processed Mineral Dust. *Atmos. Environ.* **2003**, *37*, 5337-5347.
195. Voges, A. B.; Al-Abadeh, H. A.; Musorrafiti, M. J.; Bertin, P. A.; Nguyen, S. T.; Geiger, F. M., Carboxylic Acid- and Ester-Functionalized Siloxane Scaffolds on Glass Studied by Broadband Sum Frequency Generation. *J. Phys. Chem. B* **2004**, *108*.

196. Voges, A. B.; Al-Abadleh, H. A.; Geiger, F. M., "Development of Nonlinear Optical Spectroscopies for Studying Heterogeneous Environmental Catalytic Processes" in *Environmental Catalysis*; CRC Press: Boca Raton, 2005.
197. Weschler, C. J.; Hodgson, A. T.; Wooley, J. D., Indoor Chemistry - Ozone, Volatile Organic-Compounds, and Carpets. *Environmental Science & Technology* **1992**, *26*, 2371-2377.
198. Shaughnessy, R. J.; McDaniels, T. J.; Weschler, C. J., Indoor Chemistry: Ozone and Volatile Organic Compounds Found in Tobacco Smoke. *Environmental Science & Technology* **2001**, *35*, 2758-2764.
199. Duncan, S. M.; Sexton, K. G.; Turpin, B. J., Oxygenated Vocs, Aqueous Chemistry, and Potential Impacts on Residential Indoor Air Composition. *Indoor Air* **2018**, *28*, 198-212.
200. Duncan, S. M.; Tomaz, S.; Morrison, G.; Webb, M.; Atkin, J.; Surratt, J. D.; Turpin, B. J., Dynamics of Residential Water-Soluble Organic Gases: Insights into Sources and Sinks. *Environmental Science & Technology* **2019**, *53*, 1812-1821.
201. Kidd, C.; Perraud, V.; Wingen, L. M.; Finlayson-Pitts, B. J., Integrating Phase and Composition of Secondary Organic Aerosol from the Ozonolysis of  $\alpha$ -Pinene. *Proceedings of the National Academy of Sciences* **2014**, *111*, 7552-7557.
202. Zhang, Y.; Sanchez, M.; Douet, C.; Wang, Y.; Bateman, A.; Gong, Z.; Kuwata, M.; Renbaum-Wolff, L.; Sato, B.; Liu, P., Changing Shapes and Implied Viscosities of Suspended Submicron Particles. *Atmospheric Chemistry and Physics* **2015**, *15*, 7819-7829.
203. Renbaum-Wolff, L.; Song, M.; Marcolli, C.; Zhang, Y.; Liu, P. F.; Grayson, J. W.; Geiger, F. M.; Martin, S. T.; Bertram, A. K., Observations and Implications of Liquid-Liquid Phase Separation at High Relative Humidities in Secondary Organic Material Produced by  $\alpha$ -Pinene Ozonolysis without Inorganic Salts. *Atmos. Chem. Phys.* **2016**, *16*, 7969-79.
204. Song, M.; Liu, P.; Martin, S. T.; Bertram, A. K., Liquid-Liquid Phase Separation in Particles Containing Secondary Organic Material Free of Inorganic Salts. *Atmos. Chem. Phys.* **2017**, *17*, 11261-11271.
205. Stewart, D. J.; Cai, C.; Nayler, J.; Preston, T. C.; Reid, J. P.; Krieger, U. K.; Marcolli, C.; Zhang, Y. H., Liquid-Liquid Phase Separation in Mixed Organic/Inorganic Single Aqueous Aerosol Droplets. *The Journal of Physical Chemistry A* **2015**, *119*, 4177-4190.
206. Björneholm, O., et al., Water at Interfaces. *Chem. Rev.* **2016**, *116*, 7698-7726.

207. Knipping, E. M.; Lakin, M. J.; Foster, K. L.; Jungwirth, P.; Tobias, D. J.; Gerber, R. B.; Dabdub, D.; Finlayson-Pitts, B. J., Experiments and Simulations of Ion-Enhanced Interfacial Chemistry on Aqueous NaCl Aerosols. *Science* **2000**, *288*, 301-306.
208. Jungwirth, P.; Tobias, D. J., Molecular Structure of Salt Solutions: A New View of the Interface with Implications for Heterogeneous Atmospheric Chemistry. *The Journal of Physical Chemistry B* **2001**, *105*, 10468-10472.
209. Jungwirth, P.; Tobias, D. J., Specific Ion Effects at the Air/Water Interface. *Chemical Reviews* **2006**, *106*, 1259-1281.
210. Götte, L.; Parry, K. M.; Hua, W.; Verreault, D.; Allen, H. C.; Tobias, D. J., Solvent-Shared Ion Pairs at the Air–Solution Interface of Magnesium Chloride and Sulfate Solutions Revealed by Sum Frequency Spectroscopy and Molecular Dynamics Simulations. *The Journal of Physical Chemistry A* **2017**, *121*, 6450-6459.
211. Dogangun, M.; Ohno, P. E.; Liang, D.; McGeachy, A. C.; Be, A. G.; Dalchand, N.; Li, T.; Cui, Q.; Geiger, F. M., Hydrogen-Bond Networks near Supported Lipid Bilayers from Vibrational Sum Frequency Generation Experiments and Atomistic Simulations. *J. Phys. Chem. B* **2018**, *122*, 4870-4879.
212. Wei, X.; Shen, Y. R., Vibrational Spectroscopy of Ice Interfaces. *Appl. Phys. B: Lasers Opt.* **2002**, *74*, 617-620.
213. Fumagalli, L., et al., Anomalously Low Dielectric Constant of Confined Water. *Science* **2018**, *360*, 1339-42.
214. Wang, C.; Collins, D. B.; Abbatt, J. P. D., Indoor Illumination of Terpenes and Bleach Emissions Leads to Particle Formation and Growth. *Environmental Science & Technology* **2019**, *53*, 11792-11800.
215. Upshur, M. A.; Chase, H. M.; Strick, B. F.; Ebben, C. J.; Fu, L.; Wang, H.-F.; Thomson, R. J.; Geiger, F. M., Vibrational Mode Assignment of A-Pinene by Isotope Editing: One Down, Seventy-One to Go. *J. Phys. Chem. A* **2016**, *120*, 2684-2690.
216. Nozière, B., et al., The Molecular Identification of Organic Compounds in the Atmosphere: State of the Art and Challenges. *Chem. Rev.* **2015**, *115*, 3919-3983.
217. Rivera-Rios, J. C., et al., Conversion of Hydroperoxides to Carbonyls in Field and Laboratory Instrumentation: Observational Bias in Diagnosing Pristine Versus Anthropogenically Controlled Atmospheric Chemistry. *Geophysical Research Letters* **2014**, *41*, 8645-8651.

218. Lin, Y.-H., et al., Isoprene Epoxydiols as Precursors to Secondary Organic Aerosol Formation: Acid-Catalyzed Reactive Uptake Studies with Authentic Compounds. *Environmental Science & Technology* **2012**, *46*, 250-258.
219. Zhang, Z.; Lin, Y. H.; Zhang, H.; Surratt, J. D.; Ball, L. M.; Gold, A., Technical Note: Synthesis of Isoprene Atmospheric Oxidation Products: Isomeric Epoxydiols and the Rearrangement Products Cis- and Trans-3-Methyl-3,4-Dihydroxytetrahydrofuran. *Atmospheric Chemistry and Physics* **2012**, *12*, 8529-8535.
220. Upshur, M. A.; Strick, B. F.; McNeill, V. F.; Thomson, R. J.; Geiger, F. M., Climate-Relevant Physical Properties of Molecular Constituents for Isoprene-Derived Secondary Organic Aerosol Material. *Atmos. Chem. Phys.* **2014**, *14*, 10731-10740.
221. Cortés, D. A.; Elrod, M. J., Kinetics of the Aqueous Phase Reactions of Atmospherically Relevant Monoterpene Epoxides. *The Journal of Physical Chemistry A* **2017**, *121*, 9297-9305.
222. Ma, S. X.; Rindelaub, J. D.; McAvey, K. M.; Gagare, P. D.; Nault, B. A.; Ramachandran, P. V.; Shepson, P. B., *α*-Pinene Nitrates: Synthesis, Yields and Atmospheric Chemistry. *Atmos. Chem. Phys.* **2011**, *11*, 6337-6347.
223. Donahue, N. M.; Tischuk, J. E.; Marquis, B. J.; Hartz, K. E. H., Secondary Organic Aerosol from Limona Ketone: Insights into Terpene Ozonolysis Via Synthesis of Key Intermediates. *Physical Chemistry Chemical Physics* **2007**, *9*, 2991-2998.
224. Steimer, S. S.; Delvaux, A.; Campbell, S. J.; Gallimore, P. J.; Pitton, D.; Hoffmann, T.; Kalberer, M., Synthesis and Characterization of Peroxypinic Acids as Proxies for Highly Oxygenated Molecules (Homs) in Secondary Organic Aerosol. *Atmos. Chem. Phys. Discuss.* **2018**, *2018*, 1-15.
225. Hansen, A. M. K.; Hong, J.; Raatikainen, T.; Kristensen, K.; Ylisirniö, A.; Virtanen, A.; Petäjä, T.; Glasius, M.; Prisle, N. L., Hygroscopic Properties and Cloud Condensation Nuclei Activation of Limonene-Derived Organosulfates and Their Mixtures with Ammonium Sulfate. *Atmos. Chem. Phys.* **2015**, *15*, 14071-14089.
226. Fache, F.; Piva, O.; Mirabel, P., First Synthesis of Hydroxy-Pinonaldehyde and Hydroxy-Pinonic Acid, Monoterpene Degradation Products Present in Atmosphere. *Tetrahedron Letters* **2002**, *43*, 2511-2513.
227. Jaoui, M.; Leungsakul, S.; Kamens, R. M., Gas and Particle Products Distribution from the Reaction of Beta-Caryophyllene with Ozone. *J Atmos Chem* **2003**, *45*, 261-287.

228. Jaoui, M.; Lewandowski, M.; Kleindienst, T. E.; Offenberg, J. H.; Edney, E. O., Beta-Caryophyllinic Acid: An Atmospheric Tracer for Beta-Caryophyllene Secondary Organic Aerosol. *Geophys Res Lett* **2007**, *34*.
229. Parshintsev, J.; Nurmi, J.; Kilpelainen, I.; Hartonen, K.; Kulmala, M.; Riekkola, M. L., Preparation of Beta-Caryophyllene Oxidation Products and Their Determination in Ambient Aerosol Samples. *Analytical and Bioanalytical Chemistry* **2008**, *390*, 913-919.
230. van Eijck, A.; Opatz, T.; Taraborrelli, D.; Sander, R.; Hoffmann, T., New Tracer Compounds for Secondary Organic Aerosol Formation from Beta-Caryophyllene Oxidation. *Atmospheric Environment* **2013**, *80*, 122-130.
231. Helmig, D.; Ortega, J.; Duhl, T.; Tanner, D.; Guenther, A.; Harley, P.; Wiedinmyer, C.; Milford, J.; Sakulyanontvittaya, T., Sesquiterpene Emissions from Pine Trees - Identifications, Emission Rates and Flux Estimates for the Contiguous United States. *Environmental Science & Technology* **2007**, *41*, 1545-1553.
232. Kleindienst, T. E.; Jaoui, M.; Lewandowski, M.; Offenberg, J. H.; Lewis, C. W.; Bhawe, P. V.; Edney, E. O., Estimates of the Contributions of Biogenic and Anthropogenic Hydrocarbons to Secondary Organic Aerosol at a Southeastern Us Location. *Atmos. Environ.* **2007**, *41*, 8288-8300.
233. Lewandowski, M.; Jaoui, M.; Offenberg, J. H.; Kleindienst, T. E.; Edney, E. O.; Sheesley, R. J.; Schauer, J. J., Primary and Secondary Contributions to Ambient Pm in the Midwestern United States. *Environmental Science & Technology* **2008**, *42*, 3303-3309.
234. Ye, Q.; Upshur, M. A.; Robinson, E. S.; Geiger, F. M.; Sullivan, R. C.; Thomson, R. J.; Donahue, N. M., Following Particle-Particle Mixing in Atmospheric Secondary Organic Aerosols by Using Isotopically Labeled Terpenes. *Chem* **2018**, *4*, 318-333.
235. Kenseth, C. M.; Huang, Y.; Zhao, R.; Dalleska, N. F.; Hethcox, J. C.; Stoltz, B. M.; Seinfeld, J. H., Synergistic O<sub>3</sub> + Oh Oxidation Pathway to Extremely Low-Volatility Dimers Revealed in B-Pinene Secondary Organic Aerosol. *Proceedings of the National Academy of Sciences* **2018**, *115*, 8301.
236. Zhang, X., et al., Highly Oxygenated Multifunctional Compounds in A-Pinene Secondary Organic Aerosol. *Env. Sci. Technol.* **2017**, *51*, 5932-5940.
237. Dormont, L.; Bessière, J.-M.; Cohuet, A., Human Skin Volatiles: A Review. *Journal of Chemical Ecology* **2013**, *39*, 569-578.

238. Fenske, J. D.; Paulson, S. E., Human Breath Emissions of Vocs. *Journal of the Air & Waste Management Association* **1999**, *49*, 594-598.
239. Kruza, M.; Carslaw, N., How Do Breath and Skin Emissions Impact Indoor Air Chemistry? *Indoor Air* **2019**, *29*, 369-379.
240. Nicolaidis, N., Skin Lipids: Their Biochemical Uniqueness. *Science* **1974**, *186*, 19-26.
241. Wisthaler, A.; Weschler, C. J., Reactions of Ozone with Human Skin Lipids: Sources of Carbonyls, Dicarboxyls, and Hydroxycarbonyls in Indoor Air. *Proceedings of the National Academy of Sciences* **2010**, *107*, 6568.
242. Pandrangi, L. S.; Morrison, G. C., Ozone Interactions with Human Hair: Ozone Uptake Rates and Product Formation. *Atmospheric Environment* **2008**, *42*, 5079-5089.
243. Zhou, S.; Forbes, M. W.; Abbatt, J. P. D., Kinetics and Products from Heterogeneous Oxidation of Squalene with Ozone. *Environmental Science & Technology* **2016**, *50*, 11688-11697.
244. von Domaros, M.; Lakey, P. S. J.; Shiraiwa, M.; Tobias, D. J., Multiscale Modeling of Human Skin Oil-Induced Indoor Air Chemistry: Combining Kinetic Models and Molecular Dynamics. *The Journal of Physical Chemistry B* **2020**, *124*, 3836-3843.
245. Fiegand, L. R.; McCorn Saint Fleur, M.; Morris, J. R., Reactions of Cc-Terminated Self-Assembled Monolayers with Gas-Phase Ozone. *Langmuir* **2005**, *21*, 2660-2661.
246. Hall, S. A.; Jena, K. C.; Covert, P. A.; Roy, S.; Trudeau, T. G.; Hore, D. K., Molecular-Level Surface Structure from Nonlinear Vibrational Spectroscopy Combined with Simulations. *The Journal of Physical Chemistry B* **2014**, *118*, 5617-5636.
247. Hosseinpour, S.; Roeters, S. J.; Bonn, M.; Peukert, W.; Woutersen, S.; Weidner, T., Structure and Dynamics of Interfacial Peptides and Proteins from Vibrational Sum-Frequency Generation Spectroscopy. *Chemical Reviews* **2020**, *120*, 3420-3465.
248. Mermut, O.; Phillips, D. C.; York, R. L.; McCrea, K. R.; Ward, R. S.; Somorjai, G. A., In Situ Adsorption Studies of a 14-Amino Acid Leucine-Lysine Peptide onto Hydrophobic Polystyrene and Hydrophilic Silica Surfaces Using Quartz Crystal Microbalance, Atomic Force Microscopy, and Sum Frequency Generation Vibrational Spectroscopy. *Journal of the American Chemical Society* **2006**, *128*, 3598-3607.
249. Kim, J.; Somorjai, G. A., Molecular Packing of Lysozyme, Fibrinogen, and Bovine Serum Albumin on Hydrophilic and Hydrophobic Surfaces Studied by Infrared-Visible Sum

Frequency Generation and Fluorescence Microscopy. *Journal of the American Chemical Society* **2003**, *125*, 3150-3158.

250. Liljeblad, J. F. D.; Bulone, V.; Rutland, M. W.; Johnson, C. M., Supported Phospholipid Monolayers. The Molecular Structure Investigated by Vibrational Sum Frequency Spectroscopy. *The Journal of Physical Chemistry C* **2011**, *115*, 10617-10629.

251. Cédric, V.; Yves, C.; Andre, P., Sum Frequency Generation Spectroscopy in Biosensors Technology. In *Biosensors - Emerging Materials and Applications*, Pier Andrea Serra, IntechOpen: 2011.

252. Chen, X.; Wang, J.; Sniadecki, J. J.; Even, M. A.; Chen, Z., Probing A-Helical and B-Sheet Structures of Peptides at Solid/Liquid Interfaces with Sfg. *Langmuir* **2005**, *21*, 2662-2664.

253. Nguyen, K. T.; King, J. T.; Chen, Z., Orientation Determination of Interfacial B-Sheet Structures in Situ. *The Journal of Physical Chemistry B* **2010**, *114*, 8291-8300.

254. Carr, J. K.; Wang, L.; Roy, S.; Skinner, J. L., Theoretical Sum Frequency Generation Spectroscopy of Peptides. *The Journal of Physical Chemistry B* **2015**, *119*, 8969-8983.

255. Yan, E. C. Y.; Fu, L.; Wang, Z.; Liu, W., Biological Macromolecules at Interfaces Probed by Chiral Vibrational Sum Frequency Generation Spectroscopy. *Chemical Reviews* **2014**, *114*, 8471-8498.

256. von Domaros, M.; Liu, Y.; Butman, J. L.; Perlt, E.; Geiger, F. M.; Tobias, D. J., Molecular Orientation at the Squalene/Air Interface from Sum Frequency Generation Spectroscopy and Atomistic Modeling. *The Journal of Physical Chemistry B* **2021**, *125*, 3932-3941.

257. Vácha, R.; Slavíček, P.; Mucha, M.; Finlayson-Pitts, B. J.; Jungwirth, P., Adsorption of Atmospherically Relevant Gases at the Air/Water Interface: Free Energy Profiles of Aqueous Solvation of N<sub>2</sub>, O<sub>2</sub>, O<sub>3</sub>, OH, H<sub>2</sub>O, HO<sub>2</sub>, and H<sub>2</sub>O<sub>2</sub>. *The Journal of Physical Chemistry A* **2004**, *108*, 11573-11579.

258. Vieceli, J.; Ma, O. L.; Tobias, D. J., Uptake and Collision Dynamics of Gas Phase Ozone at Unsaturated Organic Interfaces. *The Journal of Physical Chemistry A* **2004**, *108*, 5806-5814.

259. Vieceli, J.; Roeselová, M.; Potter, N.; Dang, L. X.; Garrett, B. C.; Tobias, D. J., Molecular Dynamics Simulations of Atmospheric Oxidants at the Air–Water Interface: Solvation and Accommodation of OH and O<sub>3</sub>. *The Journal of Physical Chemistry B* **2005**, *109*, 15876-15892.



260. Luecke, H.; Schobert, B.; Richter, H.-T.; Cartailier, J.-P.; Lanyi, J. K., Structure of Bacteriorhodopsin at 1.55 Å Resolution 11 edited by D. C. Rees. *Journal of Molecular Biology* **1999**, *291*, 899-911.
261. Staroverov, V. N.; Scuseria, G. E.; Tao, J.; Perdew, J. P., Comparative Assessment of a New Nonempirical Density Functional: Molecules and Hydrogen-Bonded Complexes. *The Journal of Chemical Physics* **2003**, *119*, 12129-12137.
262. Weigend, F.; Ahlrichs, R., Balanced Basis Sets of Split Valence, Triple Zeta Valence and Quadruple Zeta Valence Quality for H to Rn: Design and Assessment of Accuracy. *Physical Chemistry Chemical Physics* **2005**, *7*, 3297-3305.
263. Caldeweyher, E.; Ehlert, S.; Hansen, A.; Neugebauer, H.; Spicher, S.; Bannwarth, C.; Grimme, S., A Generally Applicable Atomic-Charge Dependent London Dispersion Correction. *The Journal of Chemical Physics* **2019**, *150*, 154122.
264. Perdew, J. P.; Burke, K.; Ernzerhof, M., Generalized Gradient Approximation Made Simple. *Physical Review Letters* **1996**, *77*, 3865-3868.
265. Turbomole V7.5 2020, a Development of University of Karlsruhe and Forschungszentrum Karlsruhe GmbH, 1989-2007, Turbomole GmbH, since 2007; Available from <https://www.turbomole.org>.
266. Lawrence, C. P.; Skinner, J. L., Ultrafast Infrared Spectroscopy Probes Hydrogen-Bonding Dynamics in Liquid Water. *Chemical Physics Letters* **2003**, *369*, 472-477.
267. Sefler, G. A.; Du, Q.; Miranda, P. B.; Shen, Y. R., Surface Crystallization of Liquid N-Alkanes and Alcohol Monolayers Studied by Surface Vibrational Spectroscopy. *Chemical Physics Letters* **1995**, *235*, 347-354.
268. Kliewer, C. J.; Bieri, M.; Somorjai, G. A., Hydrogenation of the A,B-Unsaturated Aldehydes Acrolein, Crotonaldehyde, and Prenal over Pt Single Crystals: A Kinetic and Sum-Frequency Generation Vibrational Spectroscopy Study. *Journal of the American Chemical Society* **2009**, *131*, 9958-9966.
269. Michalak, W. D.; Krier, J. M.; Komvopoulos, K.; Somorjai, G. A., Structure Sensitivity in Pt Nanoparticle Catalysts for Hydrogenation of 1,3-Butadiene: In Situ Study of Reaction Intermediates Using Sfg Vibrational Spectroscopy. *The Journal of Physical Chemistry C* **2013**, *117*, 1809-1817.

270. Kennedy, G.; Melaet, G.; Han, H.-L.; Ralston, W. T.; Somorjai, G. A., In Situ Spectroscopic Investigation into the Active Sites for Crotonaldehyde Hydrogenation at the Pt Nanoparticle–Co<sub>3</sub>O<sub>4</sub> Interface. *ACS Catalysis* **2016**, *6*, 7140-7147.
271. Walter, S. R.; Youn, J.; Emery, J. D.; Kewalramani, S.; Hennek, J. W.; Bedzyk, M. J.; Facchetti, A.; Marks, T. J.; Geiger, F. M., In-Situ Probe of Gate Dielectric-Semiconductor Interfacial Order in Organic Transistors: Origin and Control of Large Performance Sensitivities. *Journal of the American Chemical Society* **2012**, *134*, 11726-11733.
272. Chun, H. J.; Weiss, T. L.; Devarenne, T. P.; Laane, J., Vibrational Spectra and Dft Calculations of Squalene. *Journal of Molecular Structure* **2013**, *1032*, 203-206.
273. Hall, D. W.; Marshall, S. N.; Gordon, K. C.; Killeen, D. P., Rapid Quantitative Determination of Squalene in Shark Liver Oils by Raman and Ir Spectroscopy. *Lipids* **2016**, *51*, 139-147.
274. Esenturk, O.; Walker, R. A., Surface Vibrational Structure at Alkane Liquid/Vapor Interfaces. *The Journal of Chemical Physics* **2006**, *125*, 174701.
275. Watry, M. R.; Tarbuck, T. L.; Richmond, G. L., Vibrational Sum-Frequency Studies of a Series of Phospholipid Monolayers and the Associated Water Structure at the Vapor/Water Interface. *The Journal of Physical Chemistry B* **2003**, *107*, 512-518.
276. Buchy, E.; Vukosavljevic, B.; Windbergs, M.; Sobot, D.; Dejean, C.; Mura, S.; Couvreur, P.; Desmaële, D., Synthesis of a Deuterated Probe for the Confocal Raman Microscopy Imaging of Squalenoyl Nanomedicines. *Beilstein Journal of Organic Chemistry* **2016**, *12*, 1127-1135.
277. Fu, L.; Zhang, Y.; Wei, Z.-H.; Wang, H.-F., Intrinsic Chirality and Prochirality at Air/R-(+)- and S(-)-Limonene Interfaces: Spectral Signatures with Interference Chiral Sum-Frequency Generation Vibrational Spectroscopy. *Chirality* **2014**, *26*, 509-520.
278. Baryames, C. P.; Baiz, C. R., Slow Oil, Slow Water: Long-Range Dynamic Coupling across a Liquid–Liquid Interface. *Journal of the American Chemical Society* **2020**, *142*, 8063-8067.
279. Kohanski, M. A.; Lo, L. J.; Waring, M. S., Review of Indoor Aerosol Generation, Transport, and Control in the Context of Covid-19. *Int Forum Allergy Rhinol* **2020**, *10*, 1173-1179.
280. van Doremalen, N., et al., Aerosol and Surface Stability of Sars-Cov-2 as Compared with Sars-Cov-1. *New England Journal of Medicine* **2020**, *382*, 1564-1567.

281. Wang, H.; Yan, E. C. Y.; Borguet, E.; Eienthal, K. B., Second Harmonic Generation from the Surface of Centrosymmetric Particles in Bulk Solution. *Chemical Physics Letters* **1996**, *259*, 15-20.
282. Dadap, J. I.; Shan, J.; Eienthal, K. B.; Heinz, T. F., Second-Harmonic Rayleigh Scattering from a Sphere of Centrosymmetric Material. *Physical Review Letters* **1999**, *83*, 4045-4048.
283. Yang, N.; Angerer, W. E.; Yodh, A. G., Angle-Resolved Second-Harmonic Light Scattering from Colloidal Particles. *Physical Review Letters* **2001**, *87*, 103902.
284. Dadap, J. I.; Shan, J.; Heinz, T. F., Theory of Optical Second-Harmonic Generation from a Sphere of Centrosymmetric Material: Small-Particle Limit. *J. Opt. Soc. Am. B* **2004**, *21*, 1328-1347.
285. Pavlyukh, Y.; Hübner, W., Nonlinear Mie Scattering from Spherical Particles. *Physical Review B* **2004**, *70*, 245434.
286. Jen, S.-H.; Dai, H.-L., Probing Molecules Adsorbed at the Surface of Nanometer Colloidal Particles by Optical Second-Harmonic Generation. *The Journal of Physical Chemistry B* **2006**, *110*, 23000-23003.
287. Jen, S.-H.; Gonella, G.; Dai, H.-L., The Effect of Particle Size in Second Harmonic Generation from the Surface of Spherical Colloidal Particles. I: Experimental Observations. *The Journal of Physical Chemistry A* **2009**, *113*, 4758-4762.
288. de Beer, A. G. F.; Roke, S., Nonlinear Mie Theory for Second-Harmonic and Sum-Frequency Scattering. *Physical Review B* **2009**, *79*, 155420.
289. Gonella, G.; Dai, H.-L., Determination of Adsorption Geometry on Spherical Particles from Nonlinear Mie Theory Analysis of Surface Second Harmonic Generation. *Physical Review B* **2011**, *84*, 121402.
290. Gonella, G.; Dai, H.-L., Second Harmonic Light Scattering from the Surface of Colloidal Objects: Theory and Applications. *Langmuir* **2014**, *30*, 2588-2599.
291. Duboisset, J.; Brevet, P.-F., Second-Harmonic Scattering-Defined Topological Classes for Nano-Objects. *The Journal of Physical Chemistry C* **2019**, *123*, 25303-25308.
292. Wu, Y.; Li, W.; Xu, B.; Li, X.; Wang, H.; McNeill, V. F.; Rao, Y.; Dai, H.-L., Observation of Organic Molecules at the Aerosol Surface. *The Journal of Physical Chemistry Letters* **2016**, *7*, 2294-2297.

293. Qian, Y.; Deng, G.-h.; Rao, Y., In Situ Chemical Analysis of the Gas–Aerosol Particle Interface. *Analytical Chemistry* **2018**, *90*, 10967-10973.
294. Qian, Y.; Deng, G.-h.; Lapp, J.; Rao, Y., Interfaces of Gas–Aerosol Particles: Relative Humidity and Salt Concentration Effects. *The Journal of Physical Chemistry A* **2019**, *123*, 6304-6312.
295. Roke, S.; Roeterdink, W. G.; Wijnhoven, J. E. G. J.; Petukhov, A. V.; Kleyn, A. W.; Bonn, M., Vibrational Sum Frequency Scattering from a Submicron Suspension. *Physical Review Letters* **2003**, *91*, 258302.
296. de Aguiar, H. B.; de Beer, A. G. F.; Strader, M. L.; Roke, S., The Interfacial Tension of Nanoscopic Oil Droplets in Water Is Hardly Affected by Sds Surfactant. *Journal of the American Chemical Society* **2010**, *132*, 2122-2123.
297. de Aguiar, H. B.; Samson, J.-S.; Roke, S., Probing Nanoscopic Droplet Interfaces in Aqueous Solution with Vibrational Sum-Frequency Scattering: A Study of the Effects of Path Length, Droplet Density and Pulse Energy. *Chemical Physics Letters* **2011**, *512*, 76-80.
298. Vácha, R.; Rick, S. W.; Jungwirth, P.; de Beer, A. G. F.; de Aguiar, H. B.; Samson, J.-S.; Roke, S., The Orientation and Charge of Water at the Hydrophobic Oil Droplet–Water Interface. *Journal of the American Chemical Society* **2011**, *133*, 10204-10210.
299. Qian, Y.; Deng, G.-h.; Rao, Y., In Situ Spectroscopic Probing of Polarity and Molecular Configuration at Aerosol Particle Surfaces. *The Journal of Physical Chemistry Letters* **2020**, *11*, 6763-6771.

**APPENDIX****SFG Spectroscopy of Field Aerosol Samples from the GoAmazon2014/5 Campaign**

## A1.1 Background

SFG Spectroscopy has proven to be a nondestructive, sensitive technique to probe the surface composition and properties of field collected aerosol samples under ambient conditions, complementing other online or offline bulk and surface analytics. Our group participated in a few interdisciplinary studies that combined aerosol science, meteorology, chemistry, and spectroscopy to investigate complex aerosol samples from field campaigns. We conducted SFG spectral analyses of field samples from AMAZE-08 in tropical forests in the central Amazon basin, BEARPEX-2009 in anthropologically influenced pine forests in California, and HUMPPA-COPEC-2010 in boreal forests in Southern Finland.<sup>1-2</sup>

This work expands upon the previous work by studying the field aerosol samples collected in the dry season of the Amazon rainforest during the GoAmazon2014/5 campaign.<sup>3</sup> Detailed descriptions of the sample collection sites and methods can be found in Dr. Mary Alice Upshur's thesis. Briefly, over 100 samples were collected onto Teflon filters (diameter of 37 mm, pore size of 1  $\mu\text{m}$ ) with two apparatus, a portable PM<sub>2.5</sub> particles sampler for particulate matter under 2.5  $\mu\text{m}$  in diameter and a Micro-orifice uniform-deposit impactors (MOUDI) for various sizes of particles. The samples were collected at three locations, the T2, T3, and ZF2 sites. The city of Manaus is highly urbanized and the T2 site in Tiwa is 8 km downwind from Manaus. The T3 site is about 70 km from Manaus, at the border of a pristine forest and a heavily polluted urban area. This unique location makes T3 site great for studying the interplay between naturally generated aerosols and anthropogenic influence, thus being the most heavily instrumented site. The ZF2 site is 50 km north of Manaus and served as a reference site for pristine aerosol samples. From the particle density data collected by a condensation particle counter (CPC) on an aircraft above the sampling area, the urban plume from Manaus spread to the T2 and T3 site.

## A1.2 Results and Discussion

The *ssp*-polarized SFG spectra in the C–H stretching region of all the filter samples collected with the particle sampler were taken, with Dr. Ariana Gray Bé and Aleia Bellcross, and summarized in **Figure A1.1**. At least two spectra were taken from different spots on each sample as replicates.

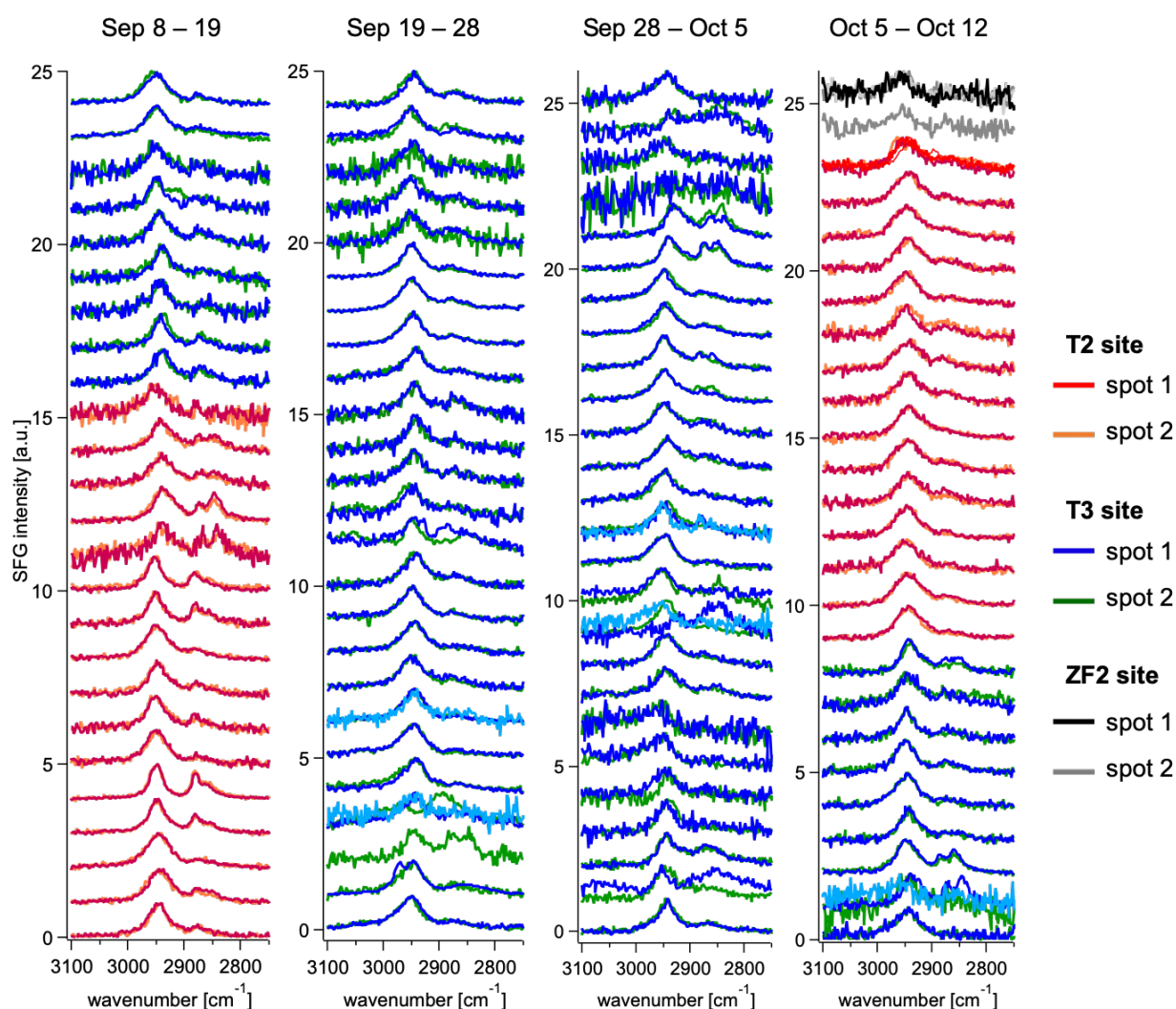


**Figure A1.1.** A compilation of *ssp*-polarized SFG spectra, in the C–H stretching region, of the filter samples collected in 2014 during the GoAmazon2014/5 Campaign.

### A1.2.1 Signal-to-Noise Ratio is not Correlated with the Collection Duration

First, the signal-to-noise ratios of the SFG spectra are analyzed as a function of the sample collection durations. A simple definition of signal-to-noise ratio was adopted in this work, which was simply the peak intensity divided by the standard deviation of the background noise. Because all the spectra were normalized to the maximum peak intensity, the signal-to-noise ratio can be relatively presented as the inverse of the standard deviation of the noise, for which the region of  $3050 - 3100 \text{ cm}^{-1}$  of each spectrum was taken as the baseline with no SFG signal present. The signal-to-noise ratios are plotted against the collection interval of each sample (**Figure A1.2**).

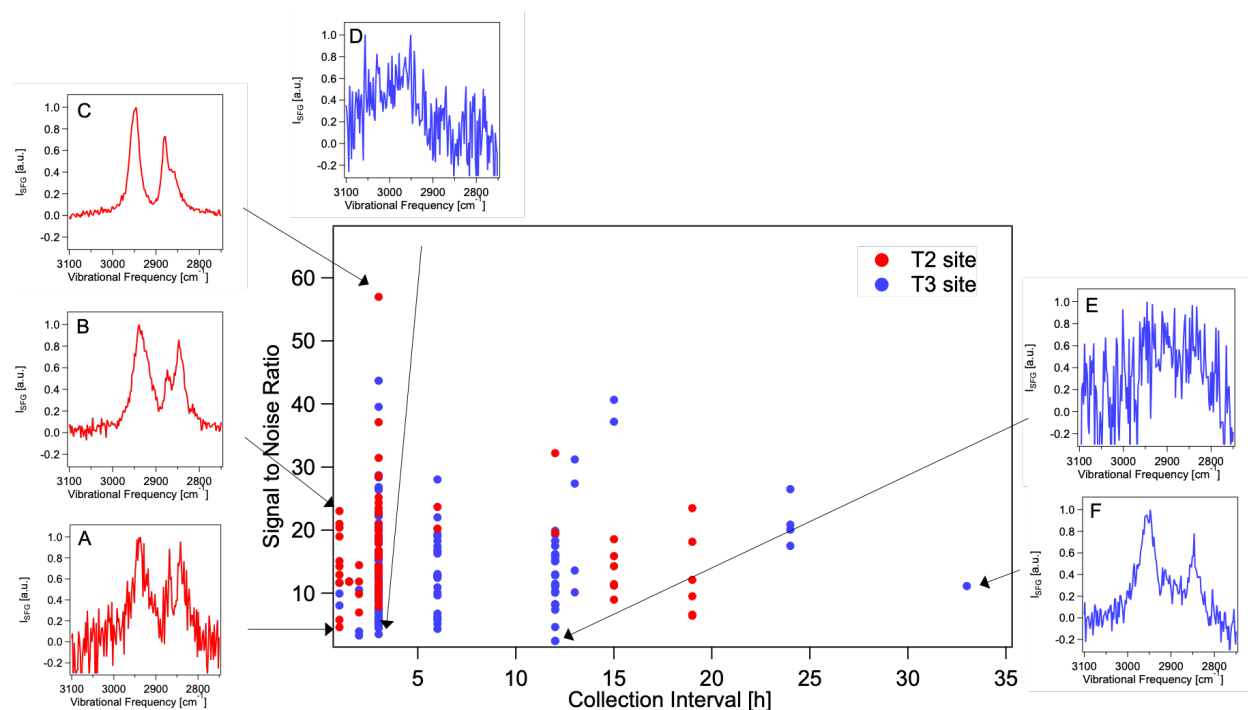


**Figure A1.2.** Signal-to-noise ratios of the samples plotted against the lengths of the collection interval, with representative spectra shown as examples. Red and blue dots indicate that the spectra were taken at the T2 and T3 site, respectively.

Contradictory to the preliminary results that seemed to indicate that signal intensity would increase with longer collection time, the current analysis suggests that signal-to-noise ratio is not correlated to the collection duration. In **Figure A1.2**, spectrum **A** and **B** have the lowest and highest



signal-to-noise ratio, respectively, from samples that were collected for one hour. Three-hour samples have the largest range of signal-to-noise ratios, with the spectrum **C** and **D** being the highest and lowest. Spectrum **E** has the lowest signal-to-noise ratio despite being taken from a 12-hour sample. The sample that was collected over the longest interval, 33 hours, does not have a distinctively high signal-to-noise ratio (spectrum **F**). This result is not surprising, since the particle density varies from time to time and thus the amount of material on the filters is not directly proportional to the length of collection duration. In addition, since SFG response is sensitive to the surface ordering of the samples, the signal intensity is not linearly related to the amount of material. Regardless, the high signal-to-noise ratio one *can* get from one-hour samples shows the low detection limit of SFG spectroscopy.

### **A1.2.2 Samples Give Two Main Types of SFG Responses**

As shown in **Figure A1.1**, none of the aerosol samples seems to contain aromatic compounds on the surface, which would give rise to a peak above  $3000\text{ cm}^{-1}$ . The samples do not exhibit large variance in spectral features. There are mainly two types of SFG responses, one containing a dominant peak at around  $2950\text{ cm}^{-1}$  and a minor peak at around  $2870\text{ cm}^{-1}$ , and one with an additional small peak around  $2850\text{ cm}^{-1}$ . We found that, the spectra that contain three peaks closely resemble the spectrum of a synthetic standard of organosulfate derived from isoprene epoxy diol (IEPOX) (**Figure A1.3**). Given that organic aerosols from tropical rainforests are known to be dominated by oxidation products from isoprene emissions, it is likely that some aerosol samples contain the IEPOX-derived organosulfates on the surface and the peak around  $2850\text{ cm}^{-1}$  can serve as an indicator.

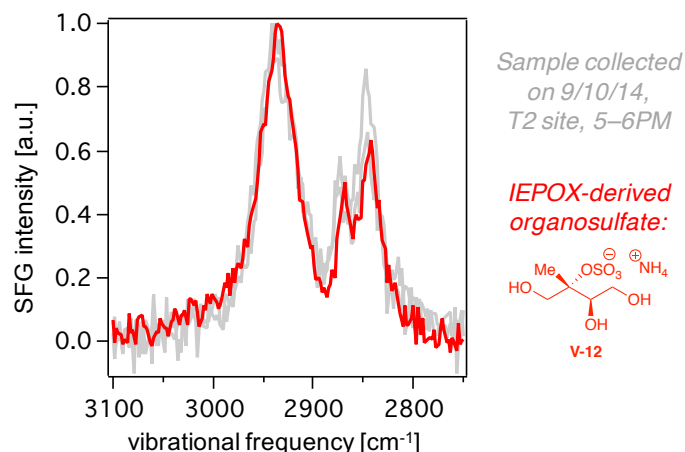


**Figure A1.3.** The overlaying of *ssp*-polarized SFG spectra of field samples collected at the T2 site and a synthesized IEPOX-derived organosulfate.

In order to quantitatively represent the intensity of the peak at around  $2850\text{ cm}^{-1}$ , the spectra were fit with three Lorentzian peaks and the peak intensity was extracted. The fitting procedure was described in Section 4.2.2B in Chapter 4, except that the nonresonant term was omitted here and only three peaks in the C–H stretching region were fitted. The common assignments of the three peaks are listed in **Table A1.1**. The asymmetric stretches are fixed to be in phase with each other but can be in phase or out of phase with symmetric stretches and Fermi resonances. The case when all three peaks are in phase was marked as (+++) and the case when the peak from symmetric stretches and Fermi resonance was out of phase was marked as (–++). The case that gave the better fit was selected.

**Table A1.1.** Common assignments of the three peaks fitted.

Wavenumber [ $\text{cm}^{-1}$ ]	Assignment
~ 2950	Methyl Asymmetric Stretch + Fermi Resonance

~ 2870

Methyl Symmetric Stretch

~ 2850

Methylene Symmetric Stretch

The fitting results for three example spectra were shown in **Figure A1.4**. In the first example, there are only two distinctive peaks in the spectra. In the second and third example, the peak around  $2850 - 2860 \text{ cm}^{-1}$  appears with different intensities.

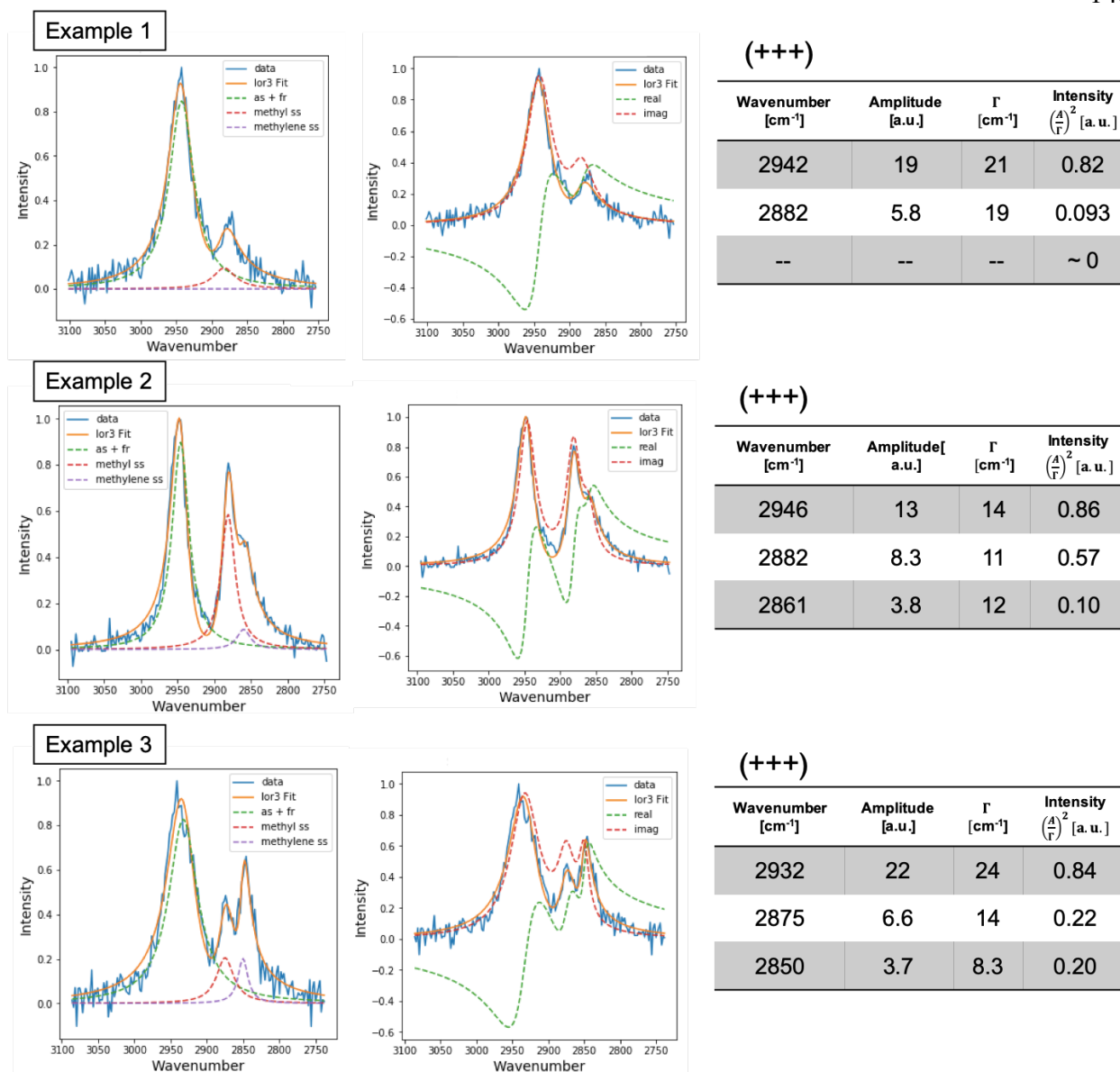


**Figure A1.4.** Fitting results of the *ssp*-polarized SFG spectra of three field aerosol samples, as examples of the two main types of SFG responses.

The intensity of the peak around 2850 cm<sup>-1</sup> from the samples was plotted over time in **Figure A1.5**. The team spent about three days at the T2 site, traveled to the T3 site, and went back to the T2 site after about a month. The samples were therefore from the two sites at different times, indicated with different colors.

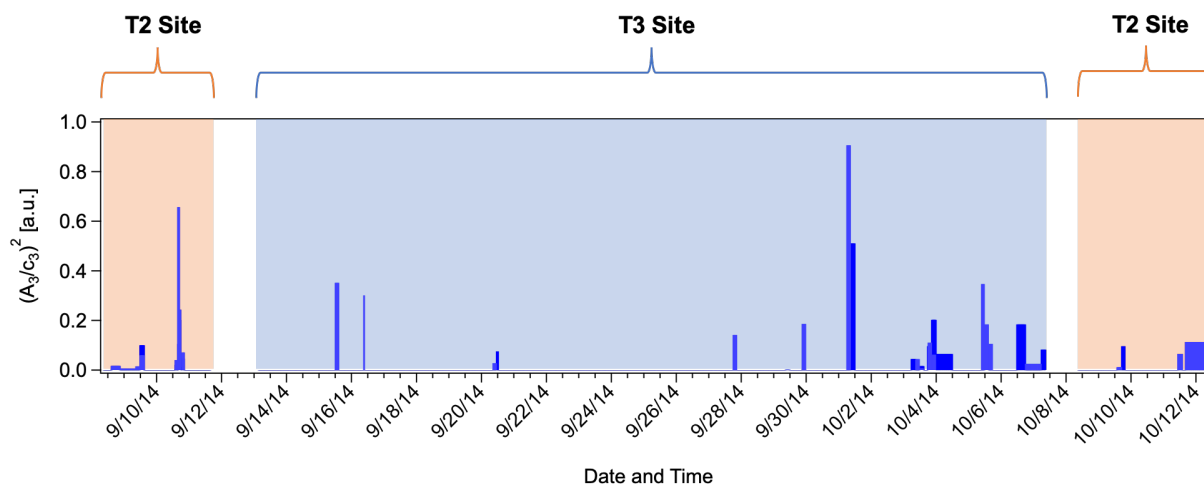


**Figure A1.5.** The intensity of the SFG peak around  $2850\text{ cm}^{-1}$  from samples collected at different times. The orange and blue backgrounds indicate that the samples were collected from the T2 and T3 sites, respectively.

The trace gas concentrations of  $\text{SO}_2(\text{g})$  and ozone and the concentrations of sulfates and organic compounds measured by a time-of-flight aerosol mass spectrometer (AMS) at the T3 site were plotted and overlaid with the peak intensity in **Figure A1.6**. The data were retrieved from the Atmospheric Radiation Measurement (ARM) Climate Research Facility database for the GoAmazon2014/5 experiment (<https://www.arm.gov/research/campaigns/amf2014goamazon>). Unfortunately, we could not find any correlation between the SFG response and these meteorological data.

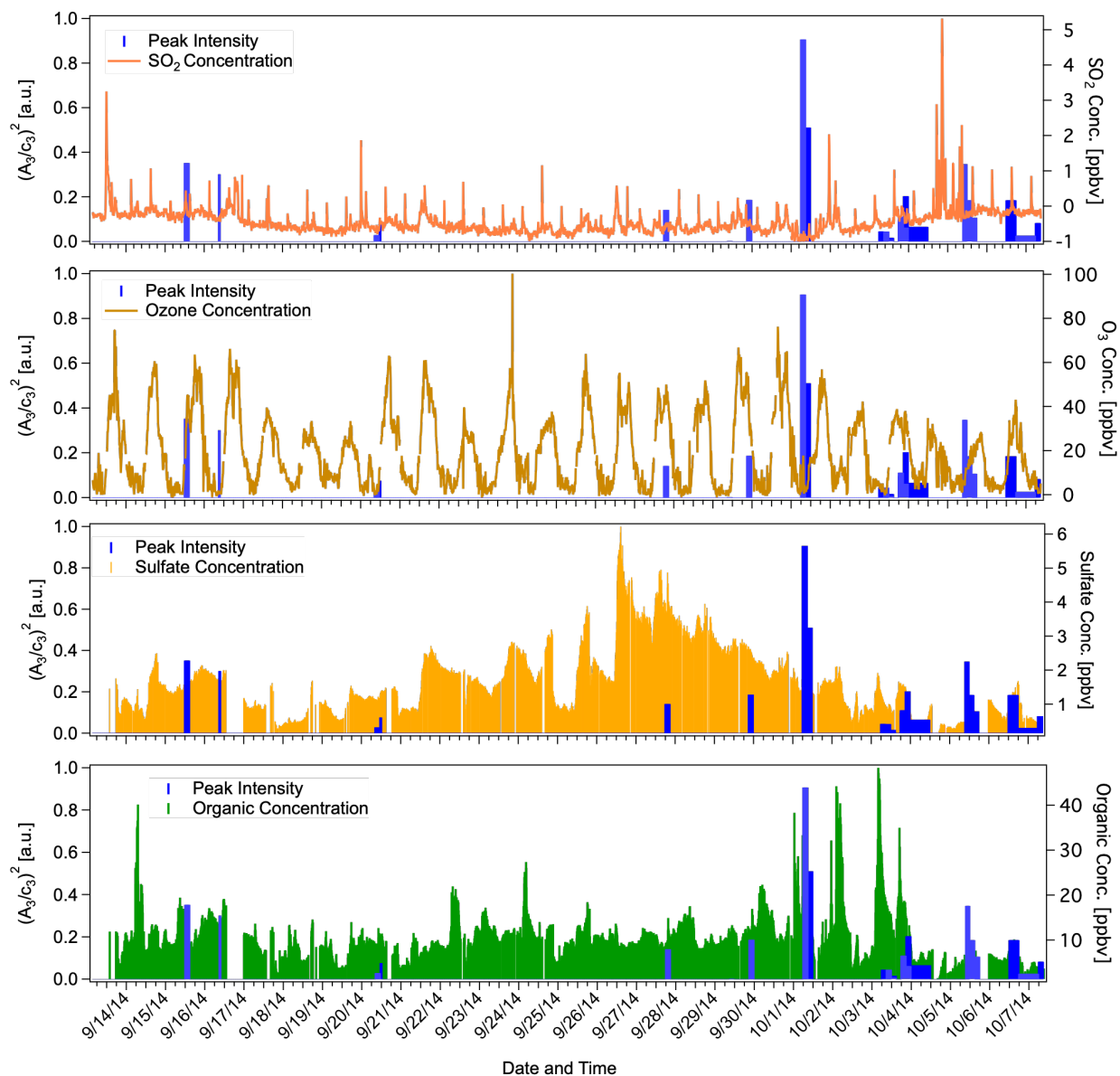


**Figure A1.6.** The overlaying of the intensity of the SFG peak around  $2850\text{ cm}^{-1}$ , with the concentrations of  $\text{SO}_2(\text{g})$ , ozone, sulfates, and organic components at the T3 site during the sample collection. The concentrations of  $\text{SO}_2(\text{g})$  and ozone were measured every second and were averaged every 10 minutes for the plots here.

One future direction on interpreting the two main SFG response of the aerosol samples collected from the GoAmazon2014/5 campaign can be to identify episodic events, such as local biomass burning events,<sup>3-4</sup> and see if they can be correlated to different spectral features.

### Appendix References

1. Ebben, C. J., et al., Contrasting Organic Aerosol Particles from Boreal and Tropical Forests During Humppa-Copec-2010 and Amaze-08 Using Coherent Vibrational Spectroscopy. *Atmos. Chem. Phys.* **2011**, *11*, 10317-10329.
2. Ebben, C. J., et al., Organic Constituents on the Surfaces of Aerosol Particles from Southern Finland, Amazonia, and California Studied by Vibrational Sum Frequency Generation. *The Journal of Physical Chemistry A* **2012**, *116*, 8271-8290.
3. Martin, S. T., et al., Introduction: Observations and Modeling of the Green Ocean Amazon (Goamazon2014/5). *Atmos. Chem. Phys.* **2016**, *16*, 4785-4797.
4. de Sá, S. S., et al., Contributions of Biomass-Burning, Urban, and Biogenic Emissions to the Concentrations and Light-Absorbing Properties of Particulate Matter in Central Amazonia During the Dry Season. *Atmos. Chem. Phys.* **2019**, *19*, 7973-8001.

**YANGDONGLING LIU**

(773) 896-4665 | yangdonglingliu2021@u.northwestern.edu

**EDUCATION**

---

**Northwestern University**

Ph.D. in Chemistry

**Evanston, IL | Sep. 2016 – Sep. 2021**

GPA: 3.95/4.00

- Management for Scientists and Engineers Certificate | Kellogg School of Management
- Graduate Certificate in Integrated Data Science | The Graduate School
- Graduate Engagement Opportunities Internship | Center for Civic Engagement

**University of California, Berkeley**

University Level Exchange for Undergraduates

**Berkeley, CA | Jan. 2015 – Aug. 2015**

GPA: 4.00/4.00

**The University of Hong Kong**

B.S. in Chemistry | First Class Honor

**Hong Kong | Sep. 2012 – Jun. 2016**

GPA: 3.94/4.30

**RESEARCH EXPERIENCE**

---

**Graduate Student Researcher**

Advisor: Prof. Franz M. Geiger

**Northwestern University | Sep. 2016 – Sep. 2021**

- Worked on second-order spectroscopic analysis of the surface chemistry of organic molecules in the atmospheric and indoor environment
- Participate in 10+ projects, published 8 papers, and delivered 3 conference presentations
- Spearhead extensive collaborations with 4 research institutions; Coordinate an indoor chemistry campaign involving 20+ participants from 8 universities
- Manage the maintenance, troubleshooting, and optimization of 3 optical instruments shared in lab; assembled a novel sum frequency scattering (SFS) laser system for studying the surfaces of suspending aerosol particles
- Built a gas flow system that mimics the real atmospheric environment with well-controlled conditions including relative humidity and ozone concentration

**Undergraduate Student Researcher**

Advisor: Prof. Vivian Wing-Wah Yam

**The University of Hong Kong | Sep. 2015 – Jun. 2016**

- Designed, synthesized, and characterized the monomer for a binuclear platinum complex with ligand structures that can enhance metal–metal interactions

**Full-time Summer Intern**

Advisor: Dr. Stefan G. Minasian

**Lawrence Berkeley National Laboratory | Jun. 2015 – Aug. 2015**

- Synthesized COF-5 by modifying a reported method and successfully deposited synthesized lanthanide complexes onto COF-5 in a uniform manner for making monodisperse nanoparticles

**Summer Undergraduate Researcher**

Advisor: Prof. Vivian Wing-Wah Yam

**The University of Hong Kong | Jun. 2014 – Aug. 2014**

- Synthesized and characterized a series of luminescent alkynylplatinum(II) phosphine complexes of different extents of  $\pi$ -conjugation
- Conducted photophysical studies of the synthesized complexes, including UV-Vis spectroscopy, emission spectroscopy, lifetime measurements, and transient absorption spectroscopy



## TECHNICAL SKILLS

---

### Spectroscopy & Microscopy

- Sum frequency generation spectroscopy, second harmonic generation spectroscopy, second harmonic imaging, atomic force microscopy, other common spectroscopic techniques such as UV-Vis, FTIR, etc.

### Other Instrumentation

- Gas flow system, quartz crystal microbalance, Langmuir-Blodgett trough, thermal evaporator

### Programming Languages (Packages) & Software

- Python (NumPy, SciPy, scikit-learn, Pandas, Matplotlib, Bokeh, Plotly), JavaScript, Git, LabVIEW, Igor Pro, Microsoft Office

### Data Science

- Statistical analysis, hypothesis testing, regression and classification with machine learning

## PUBLICATIONS

---

Ma, E.; Ohno, P. E.; Kim, J.; **Liu, Y.**; Lozier, E. H.; Miller, T. F.; Wang, H.-F.; Geiger, F. M., A New Imaginary Term in the Second-Order Nonlinear Susceptibility from Charged Interfaces. *J. Phys. Chem. Lett.* **2021**, *12*, 5649-5659.

von Domaros, M.; **Liu, Y.**; Butman, J. L.; Perlt, E.; Geiger, F. M.; Tobias, D. J., Molecular Orientation at the Squalene/Air Interface from Sum Frequency Generation Spectroscopy and Atomistic Modeling. *J. Phys. Chem. B* **2021**, *125*, 3932-3941.

**Liu, Y.**; Bé, A. G.; Or, V. W.; Alves, M. R.; Grassian, V. H.; Geiger, F. M., Challenges and Opportunities in Molecular-Level Indoor Surface Chemistry and Physics. *Cell Reports Physical Science* **2020**, *1*, 100256.

Moreau, L. M. ; Herve, A.; Straub, M. D.; Dominic, R. R.; Abergel, R. J.; Alayoglu, S.; Arnold, J.; Braun, A.; Deblonde, G. J. P.; **Liu, Y.**; Lohrey, T. D.; Olive, D. T.; Qiao, Y.; Rees, J. A.; Shuh, D. K.; Teat, S. J.; Booth, C. H.; Minasian, S. G. Structural Properties of Ultra-Small Thorium and Uranium Dioxide Nanoparticles Embedded in a Covalent Organic Framework. *Chem Sci.*, **2020**, *11*, 4648-4668.

Chang, H. B.; Ohno, P. E.; **Liu, Y.**; Lozier, E. H.; Dalchand N.; Geiger, F. M. Direct Measurement of Charge Reversal on Lipid Bilayers Using Heterodyne-Detected Second Harmonic Generation Spectroscopy. *J. Phys. Chem. B* **2020**, *124*, (4), 641-649

Bé, A. G.; **Liu, Y. (co-1st author)**; Tuladhar, A.; Bellcross, A. D.; Wang, Z.; Thomson, R. J.; Geiger, F. M. Surface-Active  $\beta$ -Caryophyllene Oxidation Products at the Air/Aqueous Interface. *ACS Earth Space Chem.* **2019**, *3*, (9), 1740-1748

Ohno, P. E.; Chang, H. B.; Spencer, A. P; **Liu, Y.**; Boamah, M. D.; Wang, H.-F.; Geiger F. M. Beyond the Gouy-Chapman Model with Heterodyne-Detected Second Harmonic Generation. *J. Phys. Chem. Lett.* **2019**, *10* (10), 2328-2334

**Liu Y.**; Chase H. M.; Geiger F. M. Partially (resp. fully) reversible adsorption of monoterpenes (resp. alkanes and cycloalkanes) to fused silica. *J. Chem. Phys.* **2019**, *150*, 074701 (Featured)

Bé, A. G.; Chase, H. M.; Liu, Y.; Upshur, M. A.; Zhang Y.; Tuladhar, A.; Chase, Z. A.; Bellcross, A. D.; Wang, H-F.; Wang, Z; Batista, V. S.; Martin, S. T.; Thomson, R. J.; Geiger, F. M. Atmospheric  $\beta$ -Caryophyllene-Derived Ozonolysis Products at Interfaces. *ACS Earth Space Chem.* **2019**, 3, (2), 158-169

## PRESENTATIONS

---

**Seven Minutes of Scholarship | CIERA, NU** **Evanston, IL | Dec. 2019**

*TED-Style Talk to General Audience*

“From Aerosols to Clouds: How Surface Chemistry Helps Unravel the Mysteries”

**Sino-European School on Atmospheric Chemistry** **Shanghai, China | Nov. 2019**

*Poster Presentation*

“Second-Order Spectroscopy of Terpenes at Aerosol Surfaces”

**American Chemical Society National Meeting** **San Diego, CA | Aug. 2019**

*Oral Presentation*

“Surface Activity and Interfacial Structure of  $\beta$ -Caryophyllene-Derived Ozonolysis Products”

**Pacific Conference on Spectroscopy and Dynamics** **San Diego, CA | Jan. 2019**

*Poster Presentation*

“Second-Order Spectroscopy of Monoterpenes Adsorbed to Model Atmospheric Surfaces”

**Chautauqua on Non-linear Optics** **West Lafayette, IN | Jun. 2017**

*Lightening Talk Presentation*

“Probing the Gas/Particle Interface of Secondary Organic Aerosols by SFG Spectroscopy”

## TEACHING & LEADERSHIP EXPERIENCE

---

**Senior Graduate Student Mentor** **Northwestern University | Sep. 2018 – Present**

- Train and advise junior graduate students on optical instruments, data analysis, and scientific writing

**Volunteer Project Judge** **Evanston, IL | May 2019**

- Communicated with six graders and assessed their proposed solutions to climate change problems as part of the first Citywide STEAM Project Showcase in Evanston

**Teaching Assistant,  
Department of Chemistry** **Northwestern University | Sep. 2016 – Jun. 2018**

- Awarded the Teaching Assistant Award for Organic Chemistry
- Supervised undergraduate students on instrumental analysis and organic chemistry experiments in lab for 6 academic quarters (>100 students in total)
- Guided pre-lab lectures that summarized experimental procedures, techniques and cautions
- Designed experimental protocols and refined instruction materials for the instrumental analysis lab
- Tutored students on course materials in one-on-one settings

**Co-Founder and Instructor,  
FUTURE Plan** **Chongqing, China | Jun. 2014**

- Designed a syllabus, organized course materials, and led in-class group discussions for an intensive oral English proficiency training workshop for non-native speakers (10 students)

**Teaching Assistant,****Department of Chemistry****The University of Hong Kong | Jun. 2013 – Aug. 2013**

- Developed course materials for an undergraduate quantum chemistry course with the professor and designed lecture slides

**Mainland Women Basketball Team****The University of Hong Kong | 2013 – 2016****(Captain for 2015 – 2016)**

- Served as a mediator to motivate the team and build healthy relationships between the players, the coach, and the manager

**AWARDS & FELLOWSHIPS**

---

TGS Conference Travel Award

**Northwestern University | 2019**

Teaching Assistant Award for Organic Chemistry

**PLU, Northwestern University | 2016 – 2017**

Norman Chui Scholarship

**The University of Hong Kong | 2016**

Undergraduate Research Fellowship

**The University of Hong Kong | 2015 – 2016**

Overseas Research Fellowship

**The University of Hong Kong | 2015**

Rosita King Ho Scholarship

**The University of Hong Kong | 2015**

Summer Research Fellowship

**The University of Hong Kong | 2014**

Dean's Honor

**The University of Hong Kong | 2012 – 2015**

Zhiyuan Fellowship

**Soong Ching Ling Foundation | 2012 – 2016**